Department of Physics
University of Fribourg (Switzerland)

Magnetic Proximity Effect in Oxide-Based Superconductor/Ferromagnet Superlattices

Thesis

by

Miguel Angel Uribe Laverde

from Bogotá, Colombia

Accepted by the Faculty of Science of the University of Fribourg (Switzerland) upon the recommendation of

Prof. Dr. Jean-Claude Dousse	University of Fribourg, Switzerland	President of the Jury
Prof. Dr. Christian Bernhard	University of Fribourg, Switzerland	Thesis Supervisor
Prof. Dr. Philipp Aebi	University of Fribourg, Switzerland	Examiner
Dr. Jochen Stahn	Paul Scherrer Institute, Switzerland	Examiner

Fribourg, July 21, 2014

Thesis supervisor: Dean:

....

Prof. Dr. Christian Bernhard   Prof. Dr. Fritz Müller

Abstract

The main goal of this thesis is to study the phenomenology of the magnetic proximity effect in $YBa_2Cu_3O_7/La_{2/3}Ca_{1/3}MnO_3$ (YBCO/LCMO) and $YBCO/LaMnO_{3+y}$(LMO) superlattices grown on $La_{0.3}Sr_{0.7}Al_{0.65}Ta_{0.35}O_3$ (LSAT) substrates with almost symmetric layer thicknesses. For both samples the cuprate and manganite layers preserve their respective superconducting and ferromagnetic properties. The superconducting transition onset temperature amounts to $T_C \approx 88\,K$ and $77\,K$ for the YBCO/LCMO and the YBCO/LMO superlattices, respectively. The reduced T_C in the latter suggests a small oxygen deficiency in the YBCO layers. The Curie temperature of the LCMO and LMO layers amounts to $T^{Curie} \approx 200\,K$ and $135\,K$, respectively. The structural properties of both samples are comparable; the superlattices are strained and adopt in-plane lattice parameters similar to the ones of the substrate. While the LCMO layers exhibit a metal-to-insulator transition at T^{Curie}, the LMO layers remain insulating in the ferromagnetic phase. This different behavior in the ferromagnetic state allows the study of the influence of the electronic properties of the ferromagnetic layers on the magnetic proximity effect.

The magnetic depth profile of the superlattices has been studied by means of polarized neutron reflectometry (PNR). The high quality of the superlattices and the stability of the LSAT substrate at low temperatures permit the measurement of the reflectivity curve up to q_z values of $0.14\,\text{Å}^{-1}$. The access to this extended q_z range allows the identification of the differences between the observations and the simulations based on different magnetic configurations at the interface. The analysis of the neutron reflectivity curves measured at room temperature reveals that the interface roughness for both the YBCO/LMCO and YBCO/LMO superlattices is similar and small. In both cases the even order superlattice Bragg peaks (SLBPs) are strongly suppressed as expected for the similar thickness of the cuprate and manganite layers. The PNR curves measured in the ferromagnetic state of the YBCO/LCMO superlattice exhibit prominent even order SLBP which suggests a mismatch between the magnetic and structural depth profiles. The observed features of the reflectivity curves are properly reproduced only when a so-called depleted layer, in which the ferromagnetic moment is strongly suppressed, is introduced on the LCMO side of the interface. These depleted layers extend over several LCMO monolayers from the interfaces and their thickness is larger than the interface roughness. This suggests that they are of intrinsic rather than structural origin. Furthermore, the temperature evolution of the reflectivity curves suggests that the thickness of the depleted layers exhibits a rather sudden change in the vicinity of the YBCO superconducting transition temperature T_C. Whether this is evidence of superconductivity-induced changes in the magnetic-depth profile needs to be further explored. In contrast, the PNR curves measured on the YBCO/LMO sample in the ferromagnetic state do not show a significant increase in the intensity of the even order SLBPs. The magnetic contributions to the neutron potential are thus nearly symmetric. The quantitative analysis of the PNR curves shows that the depleted layers in this case are bound to the first LMO monolayer at the interface. Since the structural and interface properties of the YBCO/LCMO and YBCO/LMO samples are comparable, the large difference in the strength of the depleted layers appears to be related to the electronic properties of the manganite layers. The intrinsic origin of the depleted layers is thus confirmed.

The electric and magnetic properties of the Cu ions on the YBCO side of the interface have been studied with x-ray absorption spectroscopy measurements with linear and circular

polarization. The orbital reconstruction and ferromagnetic order of the Cu ions at the interface is confirmed for both samples. The orbital reconstruction is such that the occupation of the in-plane and out-of-plane orbitals is similar, in contrast to the large orbital polarization of bulk YBCO. The induced magnetization in Cu is antiparallel to the applied field and to the magnetic moment in the manganite layers. The x-ray resonant magnetic reflectometry measurements of sample YBCO/LCMO confirm that the moments in Cu are on the YBCO side of the interface and are not consequence of chemical interdiffusion. In addition, the similar temperature dependence and switching behavior evidence that the Cu moments are coupled to the magnetization on the manganite layers. The quantitative analysis shows that the orbital reconstruction and the magnetism occur exclusively in a fraction of Cu ions located at the interface for which a modified electronic environment is evidenced. A direct link between these two effects is thus established for the first time. The obtained magnetic moment per modified Cu ion amounts to $0.18(4)\,\mu_B$ and $0.16(6)\,\mu_B$ for the YBCO/LCMO and YBCO/LMO superlattices respectively. The size of the orbital reconstruction is also similar in the two samples. These effects are thus not strongly affected by the electronic properties of the ferromagnetic layers. Nevertheless, the fraction of electronically modified Cu ions at the interface appears to be larger in the YBCO/LMO sample. The origin of this difference is still to be determined.

The simultaneous suppression of the magnetization on the manganite side of the interface and induction of a ferromagnetic moment on the YBCO side is thus confirmed for the first time. This observation suggests that in spite of the strong reduction of the net magnetization on the manganite side of the interface the magnetic correlations persist right to the interface. The depleted layers therefore cannot be regarded as non-magnetic. They must exhibit a canted antiferromagnetic or oscillatory order for which the net in-plane magnetization is largely suppressed.

Résumé

L'objectif principal de cette thèse est d'étudier la phénoménologie de l'effet de proximité magnétique dans des superréseaux de $YBa_2Cu_3O_7/La_{2/3}Ca_{1/3}MnO_3$ (YBCO/LCMO) et YBCO/$LaMnO_{3+y}$ (LMO) déposés sur des substrats $La_{0.3}Sr_{0.7}Al_{0.65}Ta_{0.35}O_3$ (LSAT) avec des épaisseurs de couche presque symétriques. Pour les deux échantillons les couches de cuprate et de manganite préservent leurs propriétés supraconductrices et ferromagnétiques respectives. Le début de la transition supraconductrice se situe à $T_C \approx 88\,K$ et $77\,K$ pour les superréseaux YBCO/LCMO et YBCO/LMO, respectivement. La réduction de T_C dans ce dernier suggère une légère déficience d'oxygène dans les couches de YBCO. La température de Curie des couches de LCMO et de LMO se situe à $T^{Curie} \approx 200\,K$ et $135\,K$, respectivement. Les propriétés structurales des deux échantillons sont comparables, les superréseaux sont contraints et adoptent des paramètres de maille dans le plan similaires à ceux-là du substrat. Les couches de LCMO présentent une transition métal-isolant à T^{Curie}, tandis que les couches de LMO restent isolantes dans la phase ferromagnétique. Ce comportement différent à l'état ferromagnétique permet l'étude de l'influence des propriétés électroniques des couches ferromagnétiques sur l'effet de proximité magnétique.

Le profil de profondeur magnétique des superréseaux a été étudié au moyen de la réflectométrie de neutrons polarisés (PNR). La haute qualité des superréseaux et la stabilité du substrat LSAT à basses températures permettent la mesure de la courbe de réflectivité pour valeurs de q_z qui montent jusqu'à $0.14\,Å^{-1}$. L'accès à cette gamme étendue de q_z permet l'identification des différences entre les observations et les simulations basées sur différentes configurations magnétiques à l'interface. L'analyse des courbes de réflectivité de neutrons mesurées à température ambiante révèle que la rugosité des interfaces pour les superréseaux YBCO/LCMO et YBCO/LMO est similaire et fiable. Dans les deux cas, les pics de Bragg de super-réseau (SLBPs) d'ordre pair sont fortement supprimés comme prévu pour l'épaisseur similaire des couches de cuprate et de manganite. Les courbes de PNR mesurées dans l'état ferromagnétique du superréseau YBCO/LCMO montrent des intenses SLBPs d'ordre pair, ce qui suggère un désaccord entre les profils de profondeur magnétique et structural. Les caractéristiques observées dans les courbes de réflectivité sont correctement reproduites seulement lorsqu'une couche dite de déplétion, dans laquelle le moment ferromagnétique est fortement supprimé, est introduite du côté de LCMO de l'interface. Ces couches de déplétion s'étendent sur plusieurs monocouches de LCMO à partir des interfaces et leur épaisseur est supérieure à la rugosité des interfaces. Cela suggère qu'elles ont une origine intrinsèque plutôt que structurelle. Par ailleurs, l'évolution des courbes de réflectivité avec la température suggère que l'épaisseur des couches de déplétion présente un changement brusque au voisinage de la température de transition supraconductrice de l'YBCO, T_C. Il faut encore explorer si ce phénomène est la preuve des changements induits par la supraconductivité dans le profil magnétique. Par contre, les courbes de PNR mesurées sur l'échantillon YBCO/LMO dans l'état ferromagnétique ne montrent pas une augmentation significative de l'intensité des SLBPs d'ordre pair. Les contributions magnétiques au potentiel des neutrons sont donc presque symétriques. L'analyse quantitative des courbes de PNR montre que les couches de déplétion dans ce cas sont limitées à la première monocouche de LMO à l'interface. Comme les propriétés structurelles et l'interface des échantillons YBCO/LCMO et YBCO/LMO sont comparables, la grande différence dans la taille des couches de déplétion semble être liée aux propriétés électroniques des couches de manganite. L'origine intrinsèque des couches de

déplétion est donc confirmée.

Les propriétés électriques et magnétiques des ions de Cu du côté d'YBCO de l'interface ont été étudiées avec des mesures de spectroscopie d'absorption des rayons X avec polarisation linéaire et circulaire. La reconstruction orbitale et l'ordre ferromagnétique des ions de Cu à l'interface sont confirmés pour les deux échantillons. La reconstruction orbitale est telle que l'occupation des orbitales dans le plan et hors du plan est similaire, à différence de la grande polarisation orbitale d'YBCO. La magnétisation induite en Cu est antiparallèle au champ appliqué et au moment magnétique dans les couches de manganite. La réflectométrie magnétique résonnante de rayons X de l'échantillon YBCO/LCMO confirme que les moments de Cu sont du côté d'YBCO de l'interface et ne sont pas conséquence de l'inter-diffusion chimique. En outre, le couplage entre les moments de Cu et la magnétisation des couches de manganite est prouvé par la similarité dans leur dépendance avec la température et leur changement avec le champ magnétique appliqué. L'analyse quantitative montre que la reconstruction orbitale et le magnétisme se produisent exclusivement dans une fraction des ions de Cu qui se trouvent à l'interface pour laquelle une modification de l'environnement électronique est mise en évidence. Un lien direct entre ces deux effets est ainsi établi pour la première fois. Le moment magnétique par ion de Cu modifié s'élève à $0.18(4)\,\mu_B$ et $0.16(6)\,\mu_B$ pour les superréseaux YBCO/LCMO et YBCO/LMO respectivement. La taille de la reconstruction orbitale est également similaire dans les deux échantillons. Ces effets ne sont donc pas fortement affectés par les propriétés électroniques des couches ferromagnétiques. Néanmoins, la fraction des ions de Cu modifiés électroniquement à l'interface semble être plus importante dans l'échantillon YBCO/LMO. Il reste à déterminer l'origine de cette différence.

La suppression simultanée de la magnétisation du côté de manganite de l'interface et l'induction d'un moment ferromagnétique du côté d'YBCO est donc confirmée pour la première fois. Cette observation suggère qu'en dépit de la forte réduction de la magnétisation nette du côté de manganite de l'interface des corrélations magnétiques persistent jusqu'à l'interface. Les couches de déplétion ne peuvent donc pas être considérées comme non-magnétiques. Elles doivent présenter un ordre antiferromagnétique imparfait ou oscillatoire pour lequel la magnétisation nette dans le plan est supprimée en grande partie.

Contents

Chapter 1

Introduction

While ferromagnetism is associated with the parallel alignment of the electronic spins in a system, the Cooper-pairs forming the condensate of conventional superconductors consist of electrons with opposite spins. These opposing ordering schemes of the electronic spins make of superconductivity and ferromagnetism two antagonistic phenomena and give rise to the question about their interaction when located in close proximity. The interplay of the competing superconducting and ferromagnetic order parameters is thus a fascinating topic that has been extensively studied theoretically and experimentally [1–3]. In recent years significant progress has been made with thin-film heterostructures from conventional superconductors and elemental or alloy ferromagnets where effects such as domain wall superconductivity [4], critical temperature oscillations with the thickness of the ferromagnetic layer in superconductor/ferromagnet/superconductor junctions [5] and a long-range proximity effect of a spin-triplet superconducting state through composite ferromagnetic layers with a non-collinear magnetic order [6], were predicted theoretically and confirmed experimentally [7–11]. These developments have inspired concepts for new kinds of spintronic devices and applications in information technology [12, 13].

The discovery of the cuprate high-temperature superconductors by Bednorz and Müller in 1986 marked a breaking point in the history of superconductivity [14]. With critical temperatures as high as $130\,\text{K}$ [15], the scientific community was challenged not only to explain the mechanism of superconductivity in these new family of superconductors but also to clear the way to new devices and applications. On the other hand, the observation of the colossal magnetoresistance effect in manganites in the nineties [16] renovated the interest on the versatile magnetic properties of these systems [17, 18]. Given the similar crystal structure of the cuprate superconductors and the manganites and their potential for high-temperature applications, the study of the interaction between the superconducting and ferromagnetic order parameters was soon extended to these systems [19–24]. Recent improvements in film deposition techniques, enable the layer by layer controlled epitaxial growth of multilayers and superlattices with very sharp interfaces [22, 25]. Experiments on this kind of oxide superconductor/ferromagnet heterostructures revealed effects such as a change in the superconducting critical temperature, T_C, related to the presence and thickness of the ferromagnetic layers, and vice-versa [22, 24]; a superconductivity-related giant magneto-resistance in ferromagnet/superconductor/ferromagnet trilayers [26]; the enhancement of T_C by an external magnetic field [27, 28] and even a superconductivity-induced modulation of the magnetic moment in the ferromagnetic layers [29]. These observations provided encouraging evidence for a sizable interaction between the superconducting and ferromagnetic order parameters in these cuprate/manganite multilayer systems. They also showed that not only the superconducting but also the magnetic properties of these oxide heterostructures are extremely versatile and need to be thoroughly investigated.

It is in the framework of this research that the so-called magnetic proximity effect was first reported in a symmetric $YBa_2Cu_3O_7/La_{2/3}Ca_{1/3}MnO_3$ (YBCO/LCMO) superlattice [30]. Polarized neutron reflectometry measurements evidenced that the structural symmetry of the

neutron potential was broken by the magnetic contribution in the vicinity of the YBCO/LCMO interfaces below T^{Curie}. Nevertheless, it was not clear whether the symmetry-breaking is the consequence of a strong reduction of the magnetization on the LCMO side of the interface or due to the induction of a net magnetization on the YBCO side. Subsequent experimental and theoretical reports have appeared in support of both scenarios. The existence of a magnetically dead-layer on the LCMO side of the interface has been evidenced by PNR, x-ray magnetic reflectometry measurements and electron energy loss spectroscopy [31, 32]. In addition, it has been predicted by density-functional calculations [33]. On the other hand, the induction of a magnetization on the Cu side of the interface has also been reported experimentally [24, 34, 35] and predicted theoretically [36]. The combined evidence thus suggest that both the suppression of the ferromagnetic order on the LCMO side of the interface and the induction of magnetization on the YBCO side may play a role in the magnetic proximity effect. Which one of these effects is more important in the observed symmetry-breaking of the neutron potential has remained unclear.

Furthermore, the magnetic order is not the only unusual property of the Cu ions on the YBCO side of the interfaces. X-ray linear dichroism measurements have shown that the strong orbital occupation anisotropy of the Cu-$3d$ orbitals of bulk YBCO is strongly reduced at the interface where a similar occupation is found for the in-plane and out-of-plane orbitals [37]. Although a direct link between this so-called orbital reconstruction and the observed magnetism in Cu was initially proposed, the observation of ordered Cu moments without an associated change in the orbital occupation opened the possibility that these are independent phenomena [24].

Whether the suppression of the ferromagnetic order on the LCMO side of the interface, and the magnetic order and orbital reconstruction of the Cu ions on the YBCO side of the interface occur simultaneously and whether these are related effects are, however, still open questions. A detailed study that allows the quantitative characterization of the magnetic properties on both sides of the interfaces in YBCO/LCMO superlattices has so far been missing.

The main goal of this thesis was to perform the first comprehensive study of the magnetic proximity effect in a YBCO/LCMO and a YBCO/LaMnO$_{3+y}$ (LMO) superlattices grown on La$_{0.3}$Sr$_{0.7}$Al$_{0.65}$Ta$_{0.35}$O$_3$(LSAT) substrates. As a first objective, the depth profile of the magnetization has been quantitatively studied to determine whether the observed changes in the symmetry of the neutron potential at the interface correspond to a suppression on the manganite side or rather to an induction of magnetism on the cuprate side. The temperature evolution of the magnetic depth profile and its dependence on the applied magnetic field have been studied as well. Secondly, the magnetic and electronic properties of the Cu and Mn ions on either side of the interfaces have been thoroughly studied. The quantitative analysis allows the determination not only of the magnetization of the Cu ions at the interface, the orbital occupation and the fraction of magnetic ions at the interface have also been quantified. Finally, the comparison of the results obtained for conducting LCMO and insulating LMO shows the dependence of the magnetic proximity effect on the electronic properties of the ferromagnetic layers.

This thesis is organized as follows. In Chapter 2 the scientific background is presented. Special emphasis is made on the polarized neutron reflectometry and x-ray absorption spectroscopy techniques. In Chapter 3 the sample characterization and all the phenomenology of the magnetic proximity effect in a symmetric YBCO/LCMO superlattice are discussed. Chapter 4 presents a corresponding analysis for the a symmetric YBCO/LMO superlattice for which the ferromagnetic layers are insulating. The concluding remarks and outlook are presented in Chapter 5.

Chapter 2

Scientific background

This chapter reviews the scientific concepts and relevant previous results that are of interest for this thesis. In section 2.1 the properties of the ferromagnetic manganites and the cuprate high temperature superconductors that have been studied in this thesis are briefly discussed. A review on the magnetic proximity effect in oxide-based superconductor/ferromagnet is also presented. Given their prime relevance in the research project that is condensed in this thesis, sections 2.2 and 2.3 are dedicated to the discussion of the theoretical and practical aspects of the polarized neutron reflectometry and the x-ray absorption spectroscopy techniques, respectively.

2.1. Manganites, superconducting cuprates and magnetic proximity effect

The electrical and magnetic properties of the ferromagnetic manganites and the cuprate superconductors are discussed in this section, special emphasis is given to the $La_{2/3}Ca_{1/3}MnO_3$ (LCMO), $LaMnO_{3+y}$ (LMO) and $YBa_2Cu_3O_7$ (YBCO) compounds. The phenomenology of the magnetic proximity effect in YBCO/LCMO heterostructures is introduced at the end of the section.

2.1.1. The $La_{1-x}Ca_xMnO_3$ and $LaMnO_{3+y}$ manganites

The manganites are manganese oxide compounds with a general formula $RE_{1-x}AE_xMnO_3$, where RE stands for a trivalent rare-earth element and AE is a divalent alkaline earth ion [17]. Due to the large distortions of the simple cubic symmetry, their crystal structure is usually described in terms of rather complicated orthorhombic or rhombohedral unit cells. Nevertheless, as exemplified in Figure 2.1(a) for the case of LCMO, their crystal arrangement corresponds essentially to a distorted pseudo-cubic perovskite structure with the (RE,AE) ion in the center, the Mn ions in the corners and the O ions in the edges of the cube. The six-fold coordinated Mn ions are thus in the center of an octahedron with O ions in the corners. In the parent compound, with $x = 0$, with a valence of $+3$ the Mn ions have 4 electrons in the $3d$ band. With increasing x, a corresponding fraction of Mn ions with valence $+4$ (with three electrons in the $3d$ band) is introduced. The substitution of the trivalent RE by the divalent AE ions can thus be regarded as a hole doping process.

The electronic structure of Mn is strongly modified by the octahedral coordination with oxygen, this symmetric arrangement makes the $3d$ orbitals that are extended along the diagonals of the cubic structure to be energetically favorable giving rise to the so-called crystal field splitting shown in Figure 2.1(b). The $3d$ band is thus split into the t_{2g} and e_g bands which are three and two-fold degenerate, respectively. The t_{2g} band is always half-filled and due to the large Hund's coupling the electrons are distributed in each of the available levels with their spins parallel. For Mn^{+3} ions, an additional electron sits in the e_g band with its spin aligned with those in the t_{2g} levels. In this configuration, the energy of the electron in the e_g band
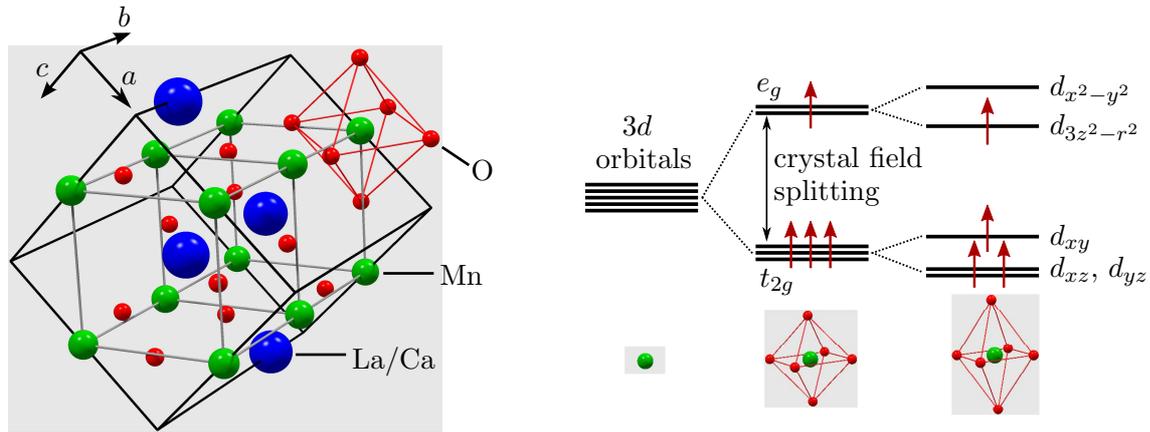
Figure 2.1: Left panel: orthorhombic unit cell of $La_{2/3}Ca_{1/3}MnO_3$. The gray lines highlight the pseudo-cubic perovskite structure which will be taken as reference throughout this thesis. The red lines depict the octahedral coordination of Mn with the neighboring O ions. Right panel: Jahn-Teller distortion. In an isolated Mn ions the $3d$ energy levels are degenerate. In a cubic environment the degeneracy is lifted and the e_g and t_{2g} degenerated bands are separated. If there is an electron in the e_g band the system may lower its energy by distorting the O octahedron to make one of the e_g orbitals energetically favorable, this is the so-called Jahn-Teller effect. The figure has been taken from Ref. [17].

can be reduced by distorting the O octahedra to lift the degeneracy and make one of the e_g orbitals energetically favorable. This is the so-called Jahn-Teller distortion and an example is also shown in Figure 2.1(b).

The manganite structures exhibit in general distortions or rotations of the O octahedra which largely affect their electric and magnetic properties. Owing to the strong electron-electron and electron-phonon interactions in these systems, the manganites exhibit a wide variety of correlated phenomena, like magnetic ordering (which can be ferromagnetic or antiferromagnetic of different types), charge ordering, orbital ordering and the so-called colossal magnetoresistance effect which caught the attention of the scientific community in the nineties after a thirty years hiatus [16, 38].

In this thesis the $La_{2/3}Ca_{1/3}MnO_3$ (LCMO) and $LaMnO_{3+y}$ (LMO) manganites are studied. Both systems are holed-doped versions of the parent compound $LaMnO_3$. In the parent compound only Mn^{+3} ions are present, the collective Jahn-Teller distortions are therefore important and stabilize an orbital-ordered, A-type antiferromagnetic phase [39]. The spins are lying in the pseudocubic ac-plane, their order is ferromagnetic along the ac-plane and antiferromagnetic along the b-direction. Due to the large Jahn-Teller effect and the large on-site repulsion which forbids the electron hoping between Mn sites the compound is insulating.

Upon hole doping, vacancies in the low energy levels of the e_g band are created and the electron hoping probability is enhanced. This gives rise to a competition between the Jahn-Teller distortion which tends to localize the electrons and the so-called double-exchange mechanism between neighboring Mn^{+3} and Mn^{+4} ions which yields a metallic state. The strength of the latter depends strongly on the band-width which is determined by the Mn-O-Mn bond angle and is largest for the case of a straight bond. The competition between the different structural and magnetic orders is further complicated if the electron-lattice and the intrasite and intersite Coulomb interactions are included. Correspondingly, the ground state of the LCMO and LMO manganites depends strongly on the doping level giving rise to the rich phase diagrams shown in Figure 2.2 for LCMO (panel a) and LMO (panel b) which were taken from Refs. [18, 40].

For LCMO a ferromagnetic and conducting state is stabilized only in the doping range where the double-exchange interaction is the most prominent. Above the Curie temperature, T^{Curie}, the system exhibits insulator-like transport properties. In a simplified picture, this can be explained by the small electron hoping probability for randomly ordered spins. When the
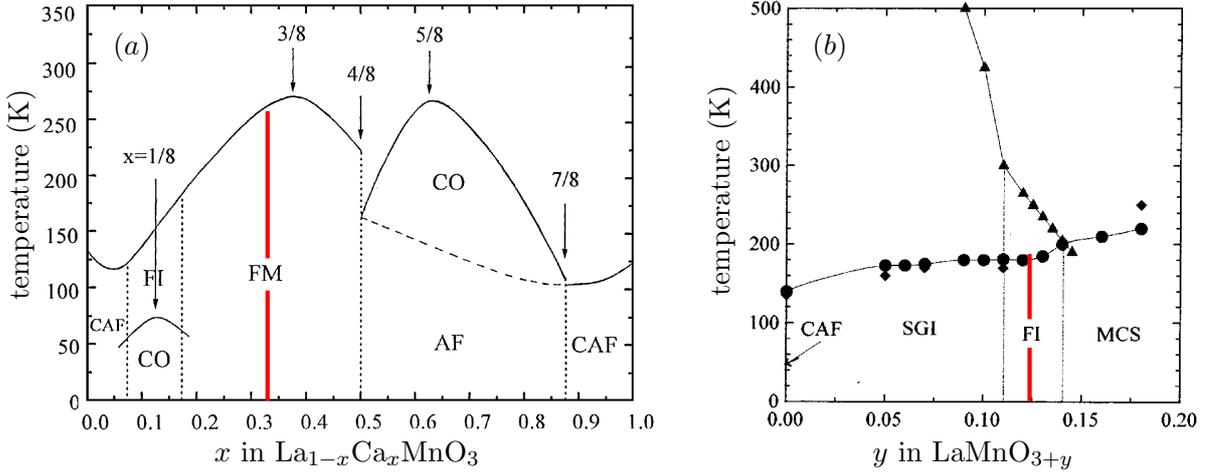
Figure 2.2: (a) Phase diagram of $La_{1-x}Ca_xMnO_3$ taken from Ref. [18]. Depending on the doping level the system can exhibit an antiferromagnetic (AF), a canted antiferromagnetic (CAF), a ferromagnetic insulating (FI) or a ferromagnetic metallic (FM) magnetic orders. In addition, the system shows charge and orbital ordering (CO). The numbers show the commensurate doping levels which mark the positions of changes in the phase diagram. (b) Phase diagram of the oxygen doped $LaMnO_{3+y}$ taken from Ref. [40]. As the La, Mn deficiency is increased, the system develops CAF, spin glass insulating (SGI), FI and metamagnetic canted spin ordering. In both cases the red lines indicate the expected doping level of the LCMO and LMO layers that are studied in this thesis.

system becomes ferromagnetic the mobility of the electrons increases and an insulator-to-metal transition is observed. For temperatures near T^{Curie} the magnetic order, and thus the electron mobility, can be largely enhanced by an applied field and the colossal magnetoresistance effect is observed [17]. The $La_{2/3}Ca_{1/3}MnO_3$ system studied in this thesis corresponds to a doping level in the middle of the ferromagnetic regime as shown in Figure 2.2(a).

As it is not possible to introduce interstitial oxygen in the $LaMnO_3$ structure, a more appropriate way to look at LMO is in terms of a La- and/or Mn-deficient compound [40]. As seen in Figure 2.2(b), with this doping scheme a ferromagnetic phase can be stabilized within a narrow range of the phase diagram. In contrast to LCMO, this ferromagnetic phase is insulating. Although the double-exchange mechanism is still promoting the ferromagnetic ordering in this system, the carriers are most likely localized by the formation of orbital polarons which are strongly coupled to the lattice [41, 42]. Although the exact composition of the LMO layers in the sample studied in this thesis was not determined, as will be discussed in section 4.2, the values of T^{Curie} and the net magnetization suggest that they are within the ferromagnetic-insulating regime as indicated by the red line in the figure.

2.1.2. The $YBa_2Cu_3O_{7-\delta}$ high-T_C superconductor

In September 1986, Bednorz and Müller reported evidence of superconductivity above 30 K in a La-Ba-Cu-O compound [14]. This discovery was a breakthrough, not only because the critical temperature was the highest ever reported at that time, but also because superconductivity had been rarely observed in oxides but mostly in pure metals and their alloys. Bednorz and Müller were thus awarded the Nobel Prize in Physics already in the following year. Soon after the initial report, the phase $La_{2-x}Ba_xCuO_4$ was identified as the one where superconductivity occurred [43, 44] and it was shown in addition that under pressure the superconducting critical temperature, T_C, can be increased to 52 K [45, 46]. In an attempt to induce chemical pressure, Wu *et al.* replaced La by the isovalent Y and found superconductivity in a Y-Ba-Cu-O compound with a T_C of 93 K [47]. The superconducting phase was later identified as $YBa_2Cu_3O_{7-\delta}$ (YBCO) [48]. It became the first superconducting compound with a T_C above the nitrogen boiling temperature thus widening the range of potential applications. Within few years, the record in T_C was raised to 133 K at ambient pressure in a
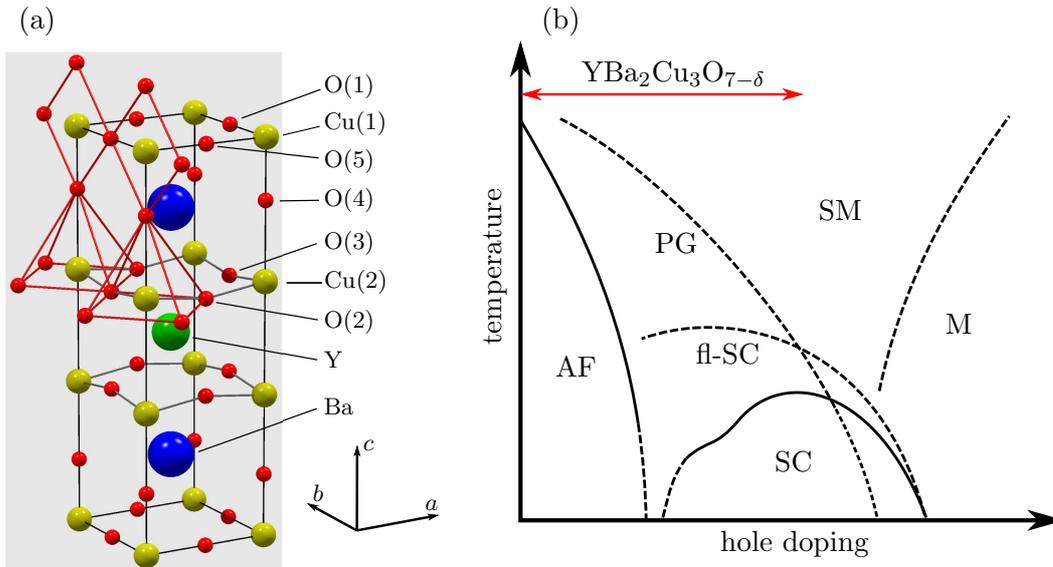
Figure 2.3: (*a*) YBCO crystal structure. The different positions of the ions in the unit cell are specified. The highlighted bonds specify the 4-fold and 5-fold oxygen coordination of the Cu(1) and Cu(2) sites, respectively. (*b*) Schematic phase diagram of the cuprate HTSC. The red arrow marks the region of the phase diagram that is accessible via oxygen variations in YBCO. Only the solid lines are confirmed phase transitions. AF: antiferromagnetic phase, PG: Pseudogap regime, fl-SC: superconducting fluctuations regime, SC: bulk superconducting phase, SM: strange metal regime, M: metallic regime.

Hg-Ba-Ca-Cu-O system [15]. Given the high T_C of these systems it soon became clear that the electron-phonon interaction responsible for superconductivity in metals and alloys was not the only ingredient in the pairing mechanism of cuprates. In spite of the massive theoretical and experimental effort to solve this problem, almost thirty years later, the exact mechanism behind the superconductivity in the Cu-based high T_C superconductors (HTSC) is still elusive.

The properties of YBCO, and all other cuprate HTSC, are closely related to its very characteristic crystal structure. The YBCO unit cell, shown in Figure 2.3(*a*), can be regarded as a stack of three oxygen-deficient perovskites. The Y and Ba ions are ordered in the crystal and, in the representation of the figure, the Y ion is at the center of the unit cell. The Cu ions occupy the corners of the pseudo-cubic perovskite units. In the fully oxygenated case, $\delta = 0$, the unit cell is orthorhombic with lattice parameters $a = 3.8206\,\text{Å}$, $b = 3.8851\,\text{Å}$ and $c = 11.6757\,\text{Å}$ [49] and the occupation of the O(5) position in the figure is zero. Two missing oxygen sites can thus be identified, one in the Y plane and one corresponding to the O(5) position. As a consequence, two different coordinations are observed for the Cu ions as shown in Figure 2.3(*a*). The Cu(2) ions in the planes adjacent to the Y plane have a five-fold pyramidal coordination with the O(2), O(3) ions in the CuO$_2$ planes and the apical O(4) position. On the other hand the Cu ions in the corners of the unit cell have a four-fold ribbon coordination with the O(1) ions along the b axis and the apical O(4) ions. The unit-cell can thus be regarded as containing two CuO$_2$ planes separated by the so-called Cu-O chains which extend along the b crystallographic direction. Indeed, it is now generally accepted that superconductivity takes place in the CuO$_2$ planes and that the Cu-O chains serve as a charge reservoir to control the carrier density in the planes. The fully oxygenated state is superconducting with a critical temperature of $T_C \approx 90\,\text{K}$.

By removing oxygen, electrons migrate from the chains to the planes via the apical O(4). The hole density and thus the carrier concentration in the CuO$_2$ planes is therefore reduced. Correspondingly, after reaching a maximum of 93 K at $\delta \approx 0.07$, T_C shows a decrease with increasing δ [50]. Structurally, with increasing δ the oxygen is removed almost exclusively from the O(1) site, a migration of O ions from the O(1) to the O(5) site also takes place. The oxygen deficiency also affects the lattice parameters and an increase in a is observed

while b and c are reduced [51]. At $\delta \approx 0.4$ the superconducting critical temperature shows a plateau and if the oxygen deficiency is further increased a sharp decay in T_C is observed until superconductivity is entirely lost around $\delta = 0.6$. At this point the occupancy of the O(1) and O(5) sites is the same and they become equivalent positions in the unit cell which in turn becomes tetragonal. By further reducing the oxygen content the occupation of the O(1) and O(5) sites decreases, the holes in the CuO$_2$ planes order antiferromagnetically and become localized as a consequence of the strong on-site Coulomb repulsion. The system thus becomes insulating. In the undoped case, $\delta = 1$, the system is an antiferromagnetic Mott-insulator with a Néel temperature of about 415 K [52].

Regarding the electronic structure of Cu in YBCO, it should be added that irrespective of the oxygen content the valence of the Cu(2) ions is close to $+2$, a $3d^9$ configuration is thus exhibited. The additional holes introduced in the CuO$_2$ planes upon oxygen doping have mainly oxygen character [53]. Since the bond length of the Cu(2) ions with the O(3) and O(2) sites is much smaller than with the O(4), the $3d_{3z^2-y^2}$ orbital in Cu is energetically more favorable than the strongly hybridized $3d_{x^2-y^2}$ one. The Cu holes in the planes therefore have a predominant $3d_{x^2-y^2}$ character [54].

The phase diagram of YBCO is shown in Figure 2.3(b). It corresponds to a portion of the universal phase diagram for cuprate HTSC. The superconducting phase in all these systems appears when the antiferromagnetic and insulating parent compounds are sufficiently hole-doped to suppress the long-range magnetic order and to enhance the mobility of the carriers. Nevertheless, if the doping is increased beyond an optimal value the system becomes more metallic and the critical temperature starts to decrease until the superconducting phase disappears. The proximity between the superconducting and the antiferromagnetic phases was soon recognized as an indication that the mechanism of superconductivity in cuprate HTSC is linked to magnetic correlations in the CuO$_2$ planes and not only to electron-phonon interactions as in conventional superconductors [55]. As seen in Figure 2.3(b), the superconducting phase is not the only anomaly in the phase diagram of cuprate HTSC. The so-called pseudogap (PG) regime is always observed in the normal state on the underdoped side of the superconducting dome. This state is characterized by the partial suppression of the low energy charge and spin excitations [56]. Whether the PG phase is a precursor of the superconductivity state or corresponds to a correlated state independent or even competing with the superconductivity is still an open question. Nevertheless, recent reports support the latter scenario as they confirm that near optimal doping the PG crossover line crosses the regime of superconducting fluctuations and the superconducting transition line as depicted in the Figure 2.3(b) [57, 58]. For optimally doped compounds a strange metal behavior, characterized by a linear variation of the resistivity with the temperature, is observed in the normal state. The confinement of this regime to the optimally doped region is often considered as an evidence of quantum criticality in these systems [59, 60].

2.1.3. Previous work on the magnetic proximity effect in YBCO/LCMO heterostructures

The so-called magnetic proximity effect in YBCO/LCMO heterostructures was first reported by J. Stahn *et al.* back in 2005 [30]. Based on polarized neutron reflectometry (PNR) measurements performed on a [YBCO(16 nm)/LCMO(16 nm)]$_{\times 6}$ superlattice grown on a SrTiO$_3$ (STO) substrate, they established that for this system there is a mismatch between the magnetic and structural depth profiles. To explain their observations they proposed two possible scenarios: the existence of a so-called magnetic "dead-layer" on the LCMO side of the interface where the magnetization is strongly suppressed, or the so-called "inverse proximity effect" according to which a net magnetization is induced on the YBCO side of the interface. To match their observations, the induced magnetization in the YBCO layers ought to be antiparallel to the applied field and the magnetization in the LCMO layers. Due to the limited q_z-range of their PNR measurements, a clear distinction between these two possibilities was not possible, the question regarding the magnetic properties of the interfaces in

YBCO/LCMO heterostructures was thus first raised.

Soon after, A. Hoffmann *et al.* reported energy electron loss spectroscopy (EELS) and PNR measurements performed on a YBCO(14 nm)/LCMO(16 nm) superlattice [31]. Their measurements showed that the occupation of the $3d$ levels in Mn increased from approximately 3.5 electrons per Mn ion in the center of the LCMO layers to almost 4.0 electrons per Mn ion at the interface. As discussed in section 2.1.1, for such a large occupation of $3d$ electrons the ferromagnetic correlations are expected to weaken and a crossover toward antiferromagnetic interactions is expected. These results were thus interpreted as an evidence for the "dead-layer" scenario.

Nevertheless, experimental evidence in support of the inverse proximity was also reported. In 2006, J. Chakhalian *et al.* published the x-ray magnetic circular dichroism (XMCD) measurements of a YBCO(10 nm)/LCMO(10 nm) superlattice that confirmed that there is a net Cu ferromagnetic moment on the YBCO side of the interface [34]. In addition, this moment is antiparallel to the magnetization in LCMO and to the applied magnetic field, as previously suggested by Stahn *et al.* in Ref. [30]. The temperature evolution of the Cu and Mn moments was found to be similar evidencing that the Cu moment arises as a consequence of an interaction with the ferromagnetic LCMO layers. The authors of this report argued that such an antiparallel alignment would not be possible without a change in the electronic configuration of either the Cu or Mn layers at the interface. This so-called orbital reconstruction was indeed reported soon after by J. Chakhalian *et al.* [37]. Based on x-ray linear dichroism (XLD) measurements performed on [YBCO(10 nm)/LCMO(10 nm)]$_{\times 10}$ superlattices grown on STO substrates, they showed that this orbital reconstruction occurs on the YBCO side of the interface. Their measurements evidenced that for the Cu ions next to the interface the predominant $3d_{x^2-y^2}$ nature of the holes is modified and that similar occupations are found for both the in-plane and out-of-plane orbitals.

The induction of a ferromagnetic ordering and the electronic reconstruction of the Cu ions at the interface were explained in terms of the so-called covalent bonding model. The redistribution of the hole in Cu to a molecular orbital shared with the Mn ion on the other side of the interface would explain the observed orbital reconstruction and the magnetization of Cu [37]. Such an electron doping of cuprates in contact with manganites had been previously predicted [61], nevertheless, it conflicts with the observations of A. Hoffmann *et al.* which suggest an electron doping on the LCMO side of the interface [31].

Theoretical works in support of both the magnetic dead layer and the inverse proximity have also been published. The first-principles density-functional calculations reported by W. Luo *et al.* predicted that the magnetic correlations in the LCMO layer get weakened near the interface with a cuprate and that they may even become antiferromagnetic [33]. According to their results the changes in the ferromagnetic correlations extend through two or three monolayers from the interface in support of the dead layer scenario. Nevertheless, the calculations also predict a slight reduction of the Mn-e_g band occupation which is in good agreement with the covalent bonding. On the other hand, Salafranca *et al.* showed that the antiparallel magnetization in Cu is an essential ingredient to explain the observed enhancement of T_C with an applied magnetic field in LCMO/YBCO/LCMO trilayers [27, 36].

The contradictory experimental evidence in support of these two different magnetic arrangements at the interface of the YBCO/LCMO superlattices can be reconciled in a picture where both effects occur simultaneously. Nevertheless, a dedicated study of the magnetic properties of the YBCO and LCMO sides of the interface that allows the quantification of the two effects has so far been missing.

The XMCD and XLD measurements on the YBCO/LCMO superlattices have raised an additional question that is yet to be answered. It concerns the link between the induced ferromagnetic moment and the orbital reconstruction of Cu. The studies of both the magnetic and orbital properties of Cu at the interface in YBCO/LCMO superlattices are scarce. Most recent reports emphasize on the induced magnetization [35, 62] while no comments are made about the electronic structure of Cu. Notably, in a paper published in 2010, R. Werner *et al.* [24] reported the XMCD and XLD measurements on a YBCO(20 nm)/LCMO(5 nm) bilayer

which confirms the induction of an antiparallel moment on the YBCO side of the interface but show no evidence of the orbital reconstruction that was reported in Ref. [37]. The authors thus suggest that the magnetization of Cu and the changes in the orbital occupation are two independent phenomena.

An additional remark concerns the influence of the STO substrates on the electric and magnetic properties of the YBCO/LCMO superlattices. This kind of substrate has been used in all the previous investigations that have been discussed above. As reported in Ref. [63], the multiple structural phase transitions experienced by STO below $105\,\mathrm{K}$ can give rise to a buckling of the surface with micrometer-sized structural domains that are tilted up to $0.5°$ and that are transmitted to the film on top of the substrate. This enhanced surface roughness strongly suppresses the neutron specular reflectivity and was one of the reasons behind the limited q_z range of the measurements of Ref. [30]. Furthermore, the domain structure of the STO modifies the magnetic domain structure of the LCMO layers on top [29]. To avoid these complications the samples studied in this thesis were grown on $La_{0.3}Sr_{0.7}Al_{0.65}Ta_{0.35}O_3$ (LSAT) substrates. These substrates have shown to be ideal for the growth of YBCO/LCMO superlattice given their stability at low temperatures and good lattice mismatch with both YBCO and LCMO [25].

2.2. Polarized Neutron Reflectometry

Owing to the wave properties of the neutron, its probability to be reflected at the surface of a thin film depends not only on its energy, but also on the depth-profile of the neutron potential in the film. Neutrons interact with the atomic nuclei and therefore the neutron potential is sensitive to the chemical composition. If a material is also magnetic, the interaction of the neutron spin and the magnetic induction introduces an additional term to the potential. Hence, the dependence of the reflectivity on the neutron momentum transfer contains essential information about the structural and magnetic depth-profiles of thin films and multilayers.

In this section an introduction to the polarized neutron reflectometry technique (PNR) is given. The basic theoretical framework is first discussed and later some experimental considerations are addressed.

2.2.1. Interaction of neutrons with matter

The two main contributions to the neutron potential in a material are the strong interaction with the nuclei and the coupling of the neutron spin with the magnetic induction. The strong interaction extends over distances much smaller than the neutron wavelength and can be considered as punctual. The interaction of a neutron with an isolated nucleus can thus be described in terms of the Fermi pseudo-potential [64]

$$V_F(r) = b \left(\frac{2\pi\hbar^2}{m_\mathrm{n}} \right) \delta(\boldsymbol{r}), \tag{2.1}$$

where b is the scattering length, $m_\mathrm{n} = 1.6749 \times 10^{-27}\,\mathrm{kg}$ is the neutron mass, $\boldsymbol{r}$ is the position of the neutron and the nucleus has been located at the origin of the coordinate system. The scattering length is in general a complex quantity and is a measure of the probability of the neutron to interact with the nucleus. Its value depends on the isotope and changes rather randomly over the periodic table giving neutrons a sizable sensitivity to most elements. The real part of b accounts for the scattering probability and, for thermal and cold neutrons ($E < 0.025\,\mathrm{eV}$), it is energy independent. The imaginary part of b accounts for the absorption and, in general, can be neglected for thermal and cold neutrons. Some exceptions are ^{3}He, ^{6}Li, Gd, Sm, B and Cd for which nuclear resonances at thermal energies lead to a significant increase in the absorption [65].

In a solid, the contribution of all nuclei to the potential must be added. For neutron reflectometry the momentum transfer is much smaller than the reciprocal lattice vectors and

the phase difference between the wavefunctions scattered by different nuclei in the unit cell can be neglected. As a consequence, the effective nuclear potential is the volume average of the Fermi pseudo-potential and for a sample constituted of a single isotope one gets [65]:

$$V_{\mathrm{n}} = \frac{1}{v} \int_v V_F(\boldsymbol{r}) d^3 \boldsymbol{r} = \frac{2\pi\hbar^2}{m_{\mathrm{n}}} Nb, \tag{2.2}$$

where N is the isotope number density. In a more general case, the solid is a compound and several different nuclei (or isotopes) contribute to the potential. The nuclear potential in equation (2.2) can then be generalized to:

$$V_{\mathrm{n}} = \frac{2\pi\hbar^2}{m_{\mathrm{n}}} \sum_i N_i b_i = \frac{2\pi\hbar^2}{m_{\mathrm{n}}} \rho_{\mathrm{n}}, \tag{2.3}$$

where the summation runs over the different kind of atoms (and isotopes) in the compound. The quantity $\rho_{\mathrm{n}} = \sum_i N_i b_i$ is usually referred to as the scattering length density and characterizes the nuclear interaction of neutrons in a compound. The scattering length for all elements and their natural isotopes has been tabulated for thermal neutrons [66], the determination of ρ_{n} is thus straightforward if the stoichiometry and density of a material are known.

The second contribution to the neutron potential is the magnetic one. The neutron carries a magnetic moment which can be written, in operator notation, as:

$$\boldsymbol{\mu} = -\mu_{\mathrm{n}} \boldsymbol{\sigma}, \tag{2.4}$$

where $\boldsymbol{\sigma} = \{\sigma_x, \sigma_y, \sigma_z\}$ is the spin $1/2$ operator represented by a vector of 2×2 Pauli matrices, and $\mu_{\mathrm{n}} = 9.662 \times 10^{-27}$ J/T is the magnitude of the neutron magnetic moment. Since the neutron gyromagnetic ratio is negative, the neutron spin and its associated magnetic moment are antiparallel. The interaction of the neutron magnetic moment and the magnetic induction can be written in terms of a Zeeman potential:

$$V_{\mathrm{m}} = -\boldsymbol{\mu} \cdot \boldsymbol{B} \tag{2.5}$$

where $\boldsymbol{B}$ is the magnetic induction. The magnetic induction in a material can be written in terms of the applied magnetic field, $\boldsymbol{H}_0$, and the sample magnetization, $\boldsymbol{M}$, as:

$$V_{\mathrm{m}} = -\boldsymbol{\mu} \cdot \mu_0 (\boldsymbol{H}_0 + (1 - D)\boldsymbol{M}), \tag{2.6}$$

where D is the demagnetization factor [65]. The total potential $V = V_{\mathrm{n}} + V_{\mathrm{m}}$ characterizes the interaction of the neutrons with the material. Inside a chemically and magnetically homogeneous layer in a thin film the neutron potential is constant in space. The interfaces between such homogeneous layers can thus be regarded as potential steps.

2.2.2. Specular reflectivity

The analysis of the PNR will be restricted to specular reflectivity. In this case the angles of incidence and reflection are the same and the momentum transfer is perpendicular to the sample surface. A sketch of the geometry of the measurement is shown in Figure 2.4. The sample surface is parallel to the xy-plane and the scattering plane corresponds to the zx-plane. Typically the magnetic field and the incident neutron spin are aligned along the y-direction. The reflectivity is measured as a function of the momentum transfer, q_z, which is defined as the difference between the reflected and the incident neutron wave vectors:

$$q_z = 2k \sin\theta = \frac{4\pi}{\lambda} \sin\theta, \tag{2.7}$$

where $k = 2\pi/\lambda$ is the magnitude of the neutron wave vector and has been assumed to be the same for the incident and reflected neutrons, λ is the neutron de Broglie wavelength and θ is the incidence angle. The assumption of elastic scattering is justified again by the small values
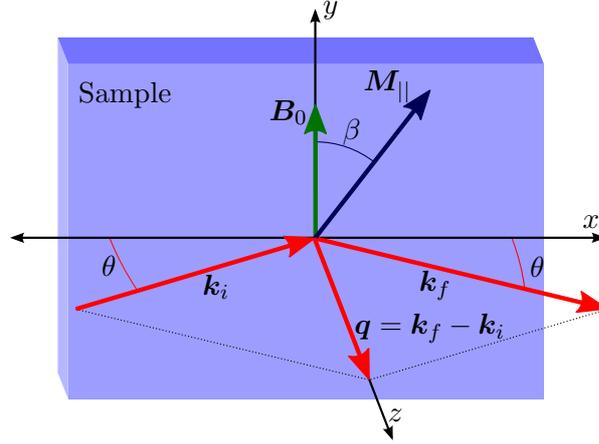
Figure 2.4: Geometry of a specular neutron reflectivity measurement. The incident and reflected wave vectors, $\boldsymbol{k}_i$ and $\boldsymbol{k}_f$, form an angle θ with respect to the sample surface. The momentum transfer is directed along the z direction. Only the magnetization of the sample along the xy plane, $\boldsymbol{M}_{||}$ is probed in neutron reflectivity. For all experiments shown in this thesis the magnetic field has been applied along the y direction.

of q_z probed in a reflectivity experiment. The neutrons are not sensitive to the atomic positions and hence are not sensitive to the collective phenomena leading to inelastic scattering.

The physics behind the reflection process can be simplified if the lateral homogeneity of the samples is assumed. In this case the neutron potential only depends on z and the neutron wavefunction in and out of the sample can be written as:

$$\Phi(\boldsymbol{r}) = \Psi(z)\mathrm{e}^{ik_x x}, \tag{2.8}$$

As a consequence, the k_x contribution to the kinetic energy, $\hbar^2 k_x^2/2m_\mathrm{n}$, is constant and only the z contribution is subjected to changes due to refraction effects. The problem can thus be reduced to the one-dimensional problem of a particle with energy $E = \hbar^2 k_0^2/2m_\mathrm{n} = \hbar^2 q_z^2/8m_\mathrm{n}$ interacting with a potential $V(z) = V_\mathrm{n}(z) + V_\mathrm{m}(z)$. Here $k_0 = q_z/2$ is the z component of the incident wave vector. The Schrödinger equation for the neutron wavefunction thus reads:

$$\left(\frac{d^2}{dz^2} + V_\mathrm{n}(z) + V_\mathrm{m}(z)\right)\Psi(z) = \frac{\hbar^2 k_0^2}{2m_\mathrm{n}}\Psi(z). \tag{2.9}$$

For a semi-infinite layer, $V(z) = V$ and the problem reduces to a particle in a potential step. This is a textbook problem and the reflectivity, known as Fresnel reflectivity and written in terms of q_z, is given by:

$$R(q_z) = \left|\frac{q_z - \sqrt{q_z^2 - \frac{8m_\mathrm{n}V}{\hbar^2}}}{q_z + \sqrt{q_z^2 - \frac{8m_\mathrm{n}V}{\hbar^2}}}\right|^2 \leq 1. \tag{2.10}$$

If the energy $\hbar^2 q_z^2/8m_\mathrm{n}$ is smaller than the potential V in the film, the square roots in equation (2.10) are imaginary and the denominator in the formula becomes the complex conjugate of the denominator. The reflectivity is thus one and total reflection occurs. The transmission probability of the neutron is finite only if the momentum transfer is larger than the critical momentum transfer, $q_z^\mathrm{c} = \sqrt{8m_\mathrm{n}V/\hbar^2}$. For values of q_z larger than q_z^c the square roots in equation (2.10) become real and the reflectivity starts to fall rapidly with q_z, the so-called total reflection edge is then observed in the reflectivity curve. The resulting reflectivity curve for a semi-infinite sample is shown, together with other different models, in Figure 2.5. In the limit $q_z \gg q_z^\mathrm{c}$ the reflectivity is simplified to $R(q_z) \approx |2m_\mathrm{n}V|^2/q_z^4\hbar^4$.

In the case of a finite film or a multilayer, the transmitted wave at the first interface will be subsequently reflected and transmitted at every interface. The resulting reflected wavefunction
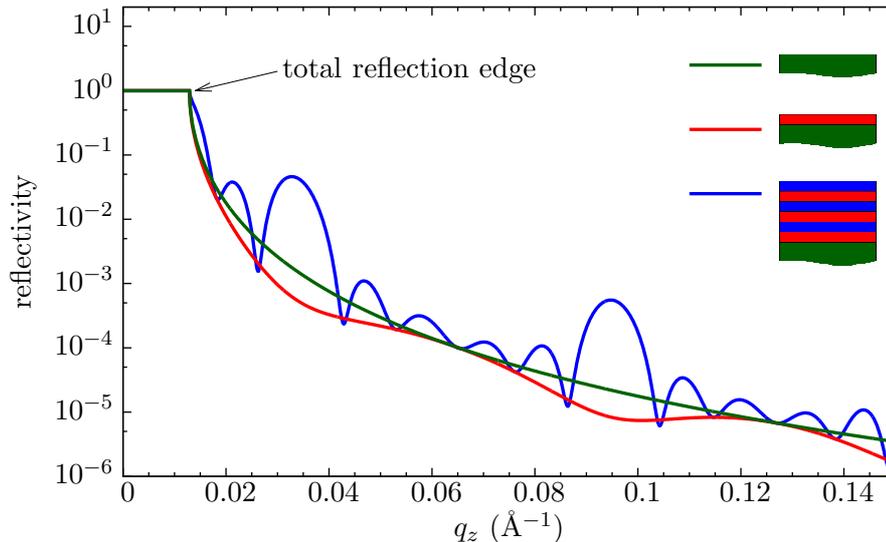
Figure 2.5: Calculated reflectivity curve for different systems: (green) a single semi-infinite substrate, (red) a single layer grown on top of the substrate, (blue) a superlattice consisting of three repetitions of a bilayer structure grown on top of the same substrate.

is the coherent superposition of the wavefunction components leaving the sample after all possible combinations of reflection and refraction processes. Depending on the scattering length density and thickness of the layers, constructive or destructive interference effects will introduce modulations to the $\sim 1/q_z^4$ dependence of the reflectivity. This effect is illustrated in Figure 2.5. The introduction of a thin film, in this case with a smaller ρ_n than the substrate, gives rise to a periodic reduction of the reflectivity. The frequency of the modulations in the reflectivity curve is directly related to the film thickness. If more layers are introduced to create a superlattice, the modulations in the intensity are more complex. Notably, the periodicity of the superlattice gives rise to strong peaks in the reflectivity curve, these are the so-called superlattice Bragg peaks (SLBP) and become narrower and more intense as the number of repetitions increases. From these examples it is clear that the reflectivity curve is largely dependent on the characteristics of the neutron potential depth-profile. A quantitative analysis requires, however, the ability to calculate the reflectivity curve for an arbitrary neutron potential.

To solve this problem the Schrödinger equation for the neutron wavefunction must be solved. Regardless of the complexity of the thin film, the standard procedure is to slice it into layers for which the neutron potential can be considered constant. For each layer, the problem of a neutron in a constant potential must be solved and the amplitude of the wavefunction in all layers is determined using the boundary conditions at the interfaces. This slicing process will introduce boundaries at the interfaces between layers with different chemical compositions, magnetic boundaries can also be introduced in case the magnetization is not homogeneous within one particular layer.

An additional consideration regarding the magnetic potential must be taken into account before proceeding to the calculation of the reflectivity. The external magnetic field $\boldsymbol{H}_0$ in equation (2.6) is constant in all the layers in the sample and outside the sample. Its contribution to the potential is therefore a constant offset and does not contribute to the potential steps which govern the reflection of the sample [67]. In addition, since the perpendicular component of the magnetic induction is continuous at the interfaces, the factor $(1 - D)\boldsymbol{M}$ is equal to the tangential component of the magnetization, $\boldsymbol{M}_{||}$ [65]. The magnetic potential can thus be simplified to:

$$V_m = -\mu_0 \boldsymbol{\mu} \cdot \boldsymbol{M}_{||}. \tag{2.11}$$

This lack of sensitivity to the component of the magnetization perpendicular to the interfaces constitutes an important limitation of the PNR technique.

In the following, a multilayer with N different layers is considered. The layer N will be assigned to the substrate and its thickness will be assumed to be infinite, the layer 0 corresponds to the atmosphere where $V \approx 0$. In layer j the scattering length density is given by $\rho_{\text{n},j}$ and the in-plane magnetization is given by $\boldsymbol{M}_{||,j} = \{M_j \sin \beta_j, M_j \cos \beta_j, 0\}$, where β_j is the angle between the applied field and the planar component of the magnetization, see figure 2.4. Since the interaction depends on the neutron spin orientation, the neutron wavefunction is two-dimensional and the Schrödinger equation for layer j reads:

$$\left[-\frac{\hbar^2}{2m_{\text{n}}} \frac{d^2}{dz^2} + \frac{2\pi\hbar^2}{m_{\text{n}}} \rho_{\text{n},j} + \frac{2\pi\hbar^2}{m_{\text{n}}} \rho_{\text{m},j} \begin{pmatrix} \cos\beta_j & \sin\beta_j \\ \sin\beta_j & -\cos\beta_j \end{pmatrix} - \frac{\hbar^2 k_0^2}{2m_{\text{n}}} \right] \begin{pmatrix} \Psi_{+,j}(z) \\ \Psi_{-,j}(z) \end{pmatrix} = 0. \quad (2.12)$$

Here $\Psi_{\pm,j}(z)$ is the probability amplitude of finding a neutron with a positive (up) or negative (down) spin projection onto the y-axis. As the magnetic field is applied along the y-direction, this direction has been chosen as the quantization axis. In equation 2.12 the so-called magnetic scattering length density has been defined as:

$$\rho_{\text{m}} = \frac{\mu_0 \mu_{\text{n}} m_{\text{n}}}{2\pi\hbar^2} M. \quad (2.13)$$

Equation 2.12 can be explicitly written to obtain:

$$-\frac{d^2}{dz^2}\Psi_{+,j}(z) + \left[4\pi\rho_{\text{n},j} + 4\pi\rho_{\text{m},j}\cos\beta_j - k_0^2 \right] \Psi_{+,j}(z) + 4\pi\rho_{\text{m},j}\sin\beta_j\Psi_{-,j}(z) = 0, \quad (2.14\text{a})$$

$$-\frac{d^2}{dz^2}\Psi_{-,j}(z) + \left[4\pi\rho_{\text{n},j} - 4\pi\rho_{\text{m},j}\cos\beta_j - k_0^2 \right] \Psi_{-,j}(z) + 4\pi\rho_{\text{m},j}\sin\beta_j\Psi_{+,j}(z) = 0. \quad (2.14\text{b})$$

Here the coupling between the $\Psi_{+,j}(z)$ and $\Psi_{-,j}(z)$ components of the wavefunction is explicit. This coupling is introduced by the $4\pi\rho_{\text{m},j}\sin\beta_j$ term, which represents the components of the magnetization perpendicular to the applied field, and gives rise to a probable change in the spin state of the neutron. This so-called spin-flip scattering can be understood in terms of the Larmor precession of the neutron spin around the magnetization projection onto the x-axis. If the magnetization is parallel to the applied field, this precession does not occur and the spin-flip processes are not possible.

Since the potential is constant within layer j, the wavefunction in the layer can be assumed as a superposition of $e^{-ik_j z}$ and $e^{ik_j z}$ plane waves. Introducing this Ansatz into equations (2.14) one gets.

$$\left[k_j^2 - k_0^2 + 4\pi(\rho_{\text{n},j} + \rho_{m,j}\cos\beta_j) \right] \Psi_{+,j}(z) + 4\pi\rho_{\text{m},j}\sin\beta_j\Psi_{-,j}(z) = 0, \quad (2.15\text{a})$$

$$4\pi\rho_{\text{m},j}\sin\beta_j\Psi_{+,j}(z) + \left[k_j^2 - k_0^2 + 4\pi(\rho_{\text{n},j} - \rho_{m,j}\cos\beta_j) \right] \Psi_{-,j}(z) = 0. \quad (2.15\text{b})$$

This coupled system of equations has a non-trivial solution only if the determinant is zero, this condition yields four possible values of k_j:

$$k_j = \pm\sqrt{k_0^2 - 4\pi(\rho_{\text{n},j} \pm \rho_{\text{m},j})}. \quad (2.16)$$

The wave vector k_j is therefore independent of β_j. This is expected as the quantum numbers of the neutron wavefunction should remain unchanged after the sample is, for example, rotated in the laboratory frame to change the value of β_j. In other words, inside the sample the quantization axis is set to the magnetization direction and it is the projection of the neutron spin with respect to the magnetization what determines the optical constants of neutrons in the layer.

The wave vector is a real number only if the z component of the incoming wave vector satisfies

$$k_0^2 = \frac{q_z^2}{4} > 4\pi(\rho_{\text{n},j} \pm \rho_{\text{m},j}). \quad (2.17)$$

If this is not the case, the wavefunction decays exponentially in the layer and the transmission probability decays exponentially with the thickness of the layer. Total reflection occurs only if

the layer is sufficiently thick. The critical momentum transfer at layer j depends in this case on whether the neutron spin is parallel or antiparallel to the magnetization and is given by:

$$q_{z,j}^{\mathrm{c}\pm} = \sqrt{16\pi(\rho_{\mathrm{n},j} \pm \rho_{\mathrm{m},j})}. \qquad (2.18)$$

where $q_{z,j}^{\mathrm{c}+}$ ($q_{z,j}^{\mathrm{c}-}$) corresponds to the critical q_z-value for neutrons with spin parallel (antiparallel) to the magnetization $\boldsymbol{M}_{\|,j}$. For values of q_z in the region between $q_{z,j}^{\mathrm{c}-}$ and $q_{z,j}^{\mathrm{c}+}$ the spin up neutrons will be totally reflected while the ones with spin down will penetrate the layer. This effect is used to create polarized neutron beams and to analyze the spin state of the scattered neutrons in experiments where the neutron polarization is relevant. In a multilayer each layer has a different critical momentum transfer value. Formally, total reflection only occurs if q_z is smaller than the critical momentum transfer of all layers. Since even in the total reflection zone tunneling might occur for very thin layers, the shape of the total reflection edge for a multilayer depends on the thickness of the layers and the stacking sequence.

The positive and negative real solutions of equation (2.16) represent the transmitted (toward the substrate) and reflected (toward the surface) components of the neutron wavefunction in layer j. The dependence of the wave vector on the spin state of the neutron originates from the sign in the square root of the equation. The spin up and down neutrons thus have a wave vector given by:

$$k_{j,+} = \sqrt{k_0^2 - 4\pi(\rho_{\mathrm{n},j} + \rho_{\mathrm{m},j})}, \qquad (2.19\mathrm{a})$$

$$k_{j,-} = \sqrt{k_0^2 - 4\pi(\rho_{\mathrm{n},j} - \rho_{\mathrm{m},j})}. \qquad (2.19\mathrm{b})$$

Magnetic samples are thus birefringent and the wave vector of the neutrons depends on their spin state.

To find the amplitude of the different wavefunctions in the layer a recursive algorithm first developed by L.G. Parrat can be applied [68]. Since in this thesis no spin-flip analysis is performed the calculations will be only presented here for the case where the magnetization and the magnetic field are collinear in all layers, i.e. $\beta_j = 0$. Under this assumption the equations (2.14) are uncoupled and the wavefunction for spin up and down neutrons are independent. In a compact form these wavefunctions in layer j can be written as:

$$\Psi_j^\pm(z) = t_j^\pm e^{ik_j^\pm z} + r_j^\pm e^{-ik_j^\pm z}, \qquad (2.20)$$

here $t_j^\pm$ is the amplitude of the wavefunction of the transmitted neutrons (moving toward the substrate) and $r_j^\pm$ is the corresponding amplitude for the reflected neutrons in layer j (moving toward the surface). The values of these amplitudes for spin up and down neutrons are different if the layer is magnetic. In the following the spin dependence will be dropped, the differences between spin up or down neutrons are implicit in the value of k_j according to the result (2.16).

A relation between the transmission and reflection amplitudes of layers j and $j + 1$ can be found by applying the wavefunction boundary conditions. The wavefunction and its first derivative must be continuous at the interface, from (2.20) one gets:

$$t_j e^{ik_j z_j} + r_j e^{-ik_j z_j} = t_{j+1} e^{ik_{j+1} z_j} + r_{j+1} e^{-ik_{j+1} z_j}, \qquad (2.21\mathrm{a})$$

$$t_j k_j e^{ik_j z_j} - r_j k_j e^{-ik_j z_j} = t_{j+1} k_{j+1} e^{ik_{j+1} z_j} - k_{j+1} r_{j+1} e^{-ik_{j+1} z_j}, \qquad (2.21\mathrm{b})$$

where z_j is the z-position of the boundary between layers j and $j + 1$. This equation can be more elegantly presented in a matrix form [65, 69]:

$$\begin{pmatrix} e^{ik_j z_j} & e^{-k_j z_j} \\ k_j e^{ik_j z_j} & -k_j e^{-k_j z_j} \end{pmatrix} \begin{pmatrix} t_j \\ r_j \end{pmatrix} = \begin{pmatrix} e^{ik_{j+1} z_j} & e^{-k_{j+1} z_j} \\ k_{j+1} e^{ik_{j+1} z_j} & -k_{j+1} e^{-k_{j+1} z_j} \end{pmatrix} \begin{pmatrix} t_{j+1} \\ r_{j+1} \end{pmatrix}. \qquad (2.22)$$

The matrix on the left-hand side can be inverted to yield:

$$\begin{pmatrix} t_j \\ r_j \end{pmatrix} = \frac{1}{2} \begin{pmatrix} \left(1 + \frac{k_{j+1}}{k_j}\right) e^{i(k_{j+1}-k_j)z_j} & \left(1 - \frac{k_{j+1}}{k_j}\right) e^{-i(k_{j+1}+k_j)z_j} \\ \left(1 - \frac{k_{j+1}}{k_j}\right) e^{i(k_{j+1}+k_j)z_j} & \left(1 + \frac{k_{j+1}}{k_j}\right) e^{-i(k_{j+1}-k_j)z_j} \end{pmatrix} \begin{pmatrix} t_{j+1} \\ r_{j+1} \end{pmatrix}. \qquad (2.23)$$

Hence, the amplitude coefficients in layers j and $j+1$ are linked by the transformation matrix:

$$Q_{j,j+1} = \frac{1}{2} \begin{pmatrix} \left(1 + \frac{k_{j+1}}{k_j}\right) e^{i(k_{j+1}-k_j)z_j} & \left(1 - \frac{k_{j+1}}{k_j}\right) e^{-i(k_{j+1}+k_j)z_j} \\ \left(1 - \frac{k_{j+1}}{k_j}\right) e^{i(k_{j+1}+k_j)z_j} & \left(1 + \frac{k_{j+1}}{k_j}\right) e^{-i(k_{j+1}-k_j)z_j} \end{pmatrix}. \qquad (2.24)$$

The transformation matrix not only relates the amplitude of the reflected and transmitted wavefunctions on either side of the interface but also contains the phase change information related to the position of the interface, z_j. As an exercise, the reflectance of layer j can be calculated assuming that the reflected amplitude in layer $j+1$ is zero and setting the origin of the z-axis at the interface. For $r_{j+1} = z_j = 0$ one obtains:

$$\mathcal{R}_j = \frac{r_j}{t_j} = \frac{t_{j+1}\left(1 - \frac{k_{j+1}}{k_j}\right)}{t_{j+1}\left(1 + \frac{k_{j+1}}{k_j}\right)} = \frac{k_j - k_{j+1}}{k_j + k_{j+1}}. \qquad (2.25)$$

The sign of the reflectance thus depends on the difference between the wave vectors in layers j and $j+1$. Therefore, if the scattering length density in layer j is larger than in layer $j+1$, the reflectance $\mathcal{R}_j < 0$ and the incoming and reflected wavefunctions have a π phase difference at the interface. This effect gives rise to the observed strong suppression of the even order SLBP in superlattices with symmetric layer thicknesses.

By applying repeatedly the transformation in equation 2.23, the wavefunction amplitudes in any layer can be written in terms of the ones in the substrate. Since the thickness of the substrate is assumed to be infinite, the probability of having reflected neutrons in this layer is zero and $r_N = 0$. In particular, the amplitude of the wavefunction outside the sample is found by setting $j = 0$ and it is possible to write:

$$\begin{pmatrix} t_0 \\ r_0 \end{pmatrix} = \prod_{j=1}^{N} Q_{j-1,j} \begin{pmatrix} t_N \\ 0 \end{pmatrix} = M \begin{pmatrix} t_N \\ 0 \end{pmatrix} = \begin{pmatrix} M_{11} & M_{12} \\ M_{21} & M_{22} \end{pmatrix} \begin{pmatrix} t_N \\ 0 \end{pmatrix}. \qquad (2.26)$$

The matrix M is the so-called reflectivity matrix and contains all the information about the thickness and scattering lengths of the layers in the sample. In terms of the components of the reflectivity matrix, the reflectivity of the sample can finally be calculated as:

$$R(q_z) = \left|\frac{r_0}{t_0}\right|^2 = \left|\frac{M_{21}}{M_{11}}\right|^2. \qquad (2.27)$$

Since no particular assumptions have been made about the values of k_j, the calculated reflectivity using the Parrat recursion formalism accounts properly for the total reflection and all refraction effects.

The Parrat formalism can be extended to the case where the magnetization is not parallel to the applied field. In this case the wavefunctions for spin up and down neutrons are coupled and the spin-flip probability amplitudes must be taken into account. The total neutron wavefunction has 8 components and the transformation and reflection matrices are 8x8 [65]. The standard formalism in these conditions becomes numerically inefficient and alternative extensions like the super-matrix [70] or super-recursion [67] algorithms are used to calculate the reflectivity of samples with arbitrary magnetization.

The calculation of $R(q_z)$ in terms of the magnitudes of r_0 and t_0 reflects the experimental lack of information regarding the phase of the neutron wavefunction. This limitation forbids the direct determination of the magnetic depth-profile from the reflectivity data. In practice, to analyze the reflectivity data a preliminary model must be proposed based on the known properties of the sample. The model is optimized after a fitting process and its validity is evaluated in terms of its capacity to reproduce the measurements.

2.2.3.   Roughness and interdiffusion

The above described algorithm assumes that the position of the interfaces, z_j, is well determined and that the neutron potential at the interfaces shows a step-like increase. In practice, however, this is never the case as either the flatness or the sharpness of the interfaces, in general both, are not perfect. If the z-position of an interface changes laterally, it is said to be rough. In this case z_j is well defined locally but over the in-plane coherence length of the neutron beam ($\sim 1 - 100\,\mu$m [69]) it exhibits a distribution of values $P(z_j)$. The roughness of the interface, σ_j, is defined as the width of this distribution. Interdiffusion, on the other hand, occurs when ions on either side of one interface migrate to the other side. In this case the scattering length density does not show a step-like change at z_j, instead it changes smoothly from one layer to the other. The width and the profile of the crossover depend on the particular characteristics of the interdiffusion effect.

In specular reflectivity one measures the in-plane average of the scattering length density as a function of the depth. Therefore, roughness and interdiffusion have the same effect and it is not possible to tell the difference between these two effects.

The interface roughness can be introduced within the Parrat formalism by approximating the distribution $P(z_j)$ to a Gaussian distribution with width σ_j. The lateral average of the $Q_{j,j+1}$ matrix in equation (2.24) gives rise to a modification of the transformation matrix in the form [65, 71]:

$$Q'_{j,j+1} = \frac{1}{2} \begin{pmatrix} A\left(1 + \frac{k_{j+1}}{k_j}\right) e^{i(k_{j+1}-k_j)\overline{z}_j} & B\left(1 - \frac{k_{j+1}}{k_j}\right) e^{-i(k_{j+1}+k_j)\overline{z}_j} \\ B\left(1 - \frac{k_{j+1}}{k_j}\right) e^{i(k_{j+1}+k_j)\overline{z}_j} & A\left(1 + \frac{k_{j+1}}{k_j}\right) e^{-i(k_{j+1}-k_j)\overline{z}_j} \end{pmatrix}, \tag{2.28}$$

where $\overline{z}_j$ is now the average position of the interface and the factors A and B are given by:

$$A = e^{-(k_{j+1}-k_j)^2\sigma_j^2/2}, \tag{2.29a}$$

$$B = e^{-(k_{j+1}+k_j)^2\sigma_j^2/2}. \tag{2.29b}$$

The reflectivity of the interface j can thus be calculated as:

$$R_j = |\mathcal{R}_j|^2 = \left|\frac{k_j - k_{j+1}}{k_j + k_{j+1}}\right|^2 e^{-2k_j k_{j+1}\sigma_j^2} = R_j^{\text{flat}} e^{-2k_j k_{j+1}\sigma_j^2}. \tag{2.30}$$

The effect of interface roughness is evident, the reflectivity is reduced by the so-called Nevot-Croce factor $e^{-2k_j k_{j+1}\sigma_j^2}$ with respect to the reflectivity of a flat surface, R_j^{flat}. The reduction of the reflectivity increases with k_j and k_{j+1} and is therefore more important at high q_z values. The extension of this approach to the case where the magnetization and the applied moment are not parallel is nevertheless difficult and constitutes a limitation to this formalism.

An alternative approach, which can be applied in any case, is the interdiffusion model. To account for interdiffusion and roughness, the interface can be sliced into many thin layers with constant scattering length density. From layer to layer the scattering length density is slightly changed to model the smooth transition at the interface. The effects on the reflectivity of this procedure are analogous to the introduction of the Nevot-Croce factor if the derivative of the scattering length density depth-profile at the interface is a Gaussian function of width σ_j.

Panel (a) in Figure 2.6 shows an example of the effects of roughness on the reflectivity curve of a sample. The reflectivity for a multilayer consisting of 10 repetitions of a symmetric bilayer structure has been calculated assuming perfectly flat interfaces and introducing a roughness of 20 nm at every interface. The reflectivity of the rough sample decreases faster with q_z. In practice the background and the limited neutron flux introduce a limitation to the minimal reflectivity that can be measured, the accessible range in q_z is thus reduced by the roughness.

Although in specular reflectivity roughness and interdiffusion effects cannot be distinguished, differences may appear in off-specular reflectivity. Indeed, if the roughness exhibits some correlation between different interfaces it leads to strong off-specular scattering [72]. Off-specular scattering will not be treated in this thesis, further information can be found in references [67, 72].
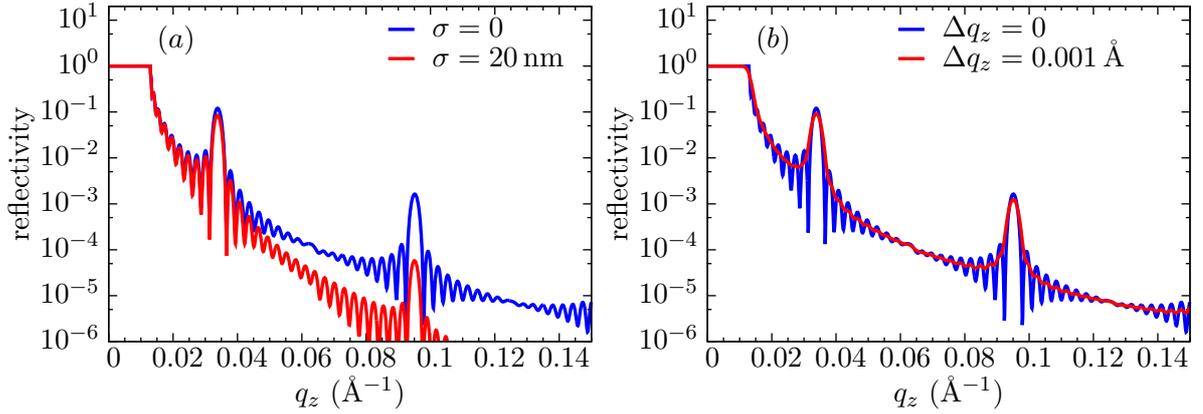
Figure 2.6: Effects of interface roughness and finite resolution on the reflectivity curves. Comparison of the reflectivity curves calculated for a multilayer consisting of 10 repetitions of a symmetric bilayer structure for (a) perfect and finite roughness and, (b) perfect and finite resolution.

2.2.4. Instrumental resolution

Another important assumption of the Parrat algorithm is that the value of q_z is perfectly well defined. In practice this is not true as there is always a finite width in the distribution of the quantities defining the momentum transfer, i.e. the incident angle, the reflected angle and the neutron wavelength. In a general case, the z-component of the momentum transfer can be written as:

$$q_z = \frac{4\pi}{\lambda}(\sin\theta_i + \sin\theta_r), \tag{2.31}$$

where θ_i and θ_r are the incidence and reflection angles, respectively. The dispersion of q_z can be estimated using the standard error propagation formula:

$$\Delta q_z = \frac{2\pi}{\lambda}\sqrt{(\cos\theta_i\Delta\theta_i)^2 + (\cos\theta_r\Delta\theta_r)^2 + (\sin\theta_i + \sin\theta_r)^2\left(\frac{\Delta\lambda}{\lambda}\right)^2}. \tag{2.32}$$

In an angle dispersive experiment the wavelength is selected with a monochromator and the wavelength dispersion is usually small ($\Delta\lambda/\lambda \approx 1\%$), the main contribution to the dispersion in q_z comes in that case from the angular divergences $\Delta\theta_{i,r}$ which are controlled with a system of slits before and after the sample or with the integration area when the measurement is performed with a 2D detector. If the slits are not changed during the measurement the dispersion in q_z, and hence the resolution, is almost constant. In an energy dispersive experiment the dispersion in the wavelength is determined by the time-resolution which results in wider distributions ($\Delta\lambda/\lambda \approx 7\%$), this is the main source of dispersion in q_z and in this case Δq_z increases almost linearly with q_z.

To account for the finite dispersion in q_z in the calculations, the reflectivity curve with perfect resolution is first calculated. This perfect reflectivity is then convoluted with a Gaussian function of width $\Delta q_z(q_z)$. The effect of resolution is illustrated in panel (b) of Figure 2.6 where the reflectivity curves calculated for a perfect and a finite and constant resolution are shown. As a consequence of a finite dispersion Δq_z the reflectivity curve is smoothed and the high frequency features of the reflectivity are averaged out.

2.2.5. Setup of a polarized neutron reflectometry experiment

In a polarized neutron reflectometry (PNR) experiment the reflectivity of polarized neutrons is measured as a function of the momentum transfer q_z. As specified in equation (2.7), this quantity depends on the incidence angle and the wavelength of the neutrons. Hence, q_z can be scanned by varying either one of these two values. This defines two possible measurement modes. In the angle dispersive mode a single wavelength is used and q_z is scanned
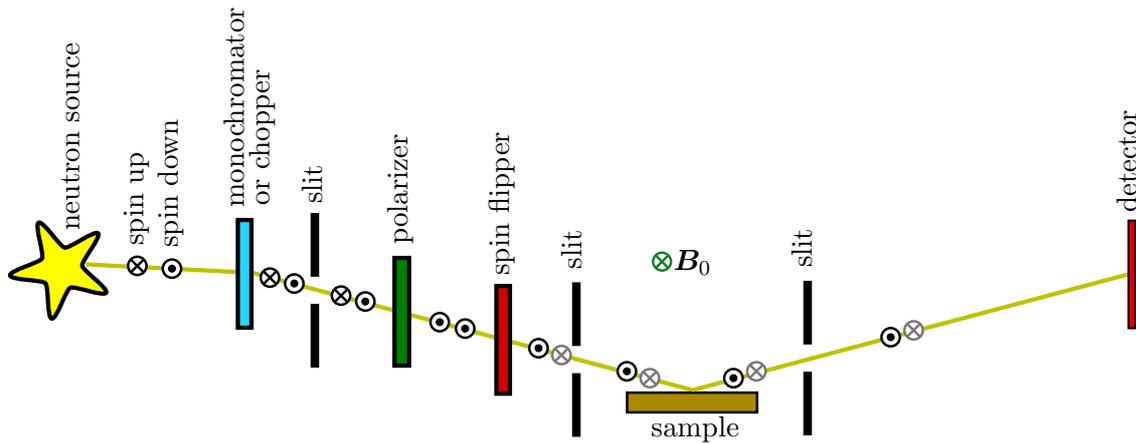
Figure 2.7: Schematic diagram of a polarized neutron reflectometry experiment. The spin up and down directions are defined parallel and antiparallel to the applied field $\boldsymbol{B}_0$, respectively.

by varying the angle of incidence. In the energy dispersive (or time-of-flight) mode, on the other hand, the angle is kept fixed and the reflectivity for different wavelengths is measured to extract the q_z dependence.

Figure (2.7) shows a general schematic diagram of the PNR experiment setup that has been used to perform the measurements presented in this thesis. For the experiments performed at SuperADAM and NREX, the neutrons are generated in a nuclear reactor. In the case of AMOR, the neutrons are generated by a spallation source. SuperADAM and NREX are angle-dispersive instruments for which a single wavelength is filtered by a monochromator. AMOR is a time-of-flight instrument and a double-chopper system is used to modulate the beam into pulsed bunches of neutrons with a well known wavelength distribution. The wavelength of each detected neutron is determined by the time it takes to travel from the chopper to the detector, to get this information a time-sensitive detector synchronized to the chopper must be used.

Although unpolarized neutrons are sensitive to the magnetism, the best way to investigate the magnetic properties of a given sample is to measure separately the reflectivity curves for neutrons with spin parallel (spin up) and antiparallel (spin down) to the applied field $\boldsymbol{H}_0$. The neutron beam is thus polarized by introducing a mirror which is positioned in such a way that only neutrons with a given spin direction (spin down in Figure 2.7) are transmitted. To measure the reflectivity of the neutrons with opposite spin one either introduces a spin-flipper, or inverts the magnetization in the polarizer. In SuperADAM and NREX a so-called Mezei spin-flipper is used. It basically consists of a coil that produces a magnetic field which is perpendicular to both the neutron wave vector and the spin axis of the neutron beam. This magnetic field induces a Larmor precession of the neutron spin and the current in the coil is tuned to produce a rotation of exactly $180°$ after the neutron leaves the device. This procedure cannot be applied if the beam consists of polydispersive neutrons with different speed. At AMOR the magnetization of the polarizer is therefore reversed to change the polarization of the incident neutron beam. In most of the measurements presented in this thesis no spin-polarization analysis has been performed to the reflected neutron beam.

A system of two slits is placed before the sample to control the angular divergence and thus the resolution. An additional slit system placed after the sample is used to reduce the angular acceptance of the detector and the background. The detector can be 1D or 2D sensitive, the latter is specially efficient for measuring the off-specular reflectivity. The detector is usually positioned about 2-3 m away from the sample to enhance the angular resolution. The reflectivity, in arbitrary units, is defined as the ratio between the incident and the reflected intensities:

$$R(q_z) = \frac{I_{\mathrm{ref}}(q_z)}{I_0(q_z)}, \tag{2.33}$$

where $I_{\mathrm{ref}}(q_z)$ is the neutron intensity measured at the detector. The incident intensity $I_0(q_z)$ is measured in a different way for each measurement mode. In the angle dispersive experiments a monitor is placed before the sample (not shown in Figure 2.7), this device can be regarded as a detector with a very small efficiency and large transmittance. The number of detected neutrons per time unit at the monitor is proportional to the total incoming flux. In an energy dispersive instrument, $I_0(q_z)$ is extracted from the wavelength distribution of the incoming neutron bunches. This distribution can be determined with a measurement of the direct beam.

An additional aspect needs to be discussed in the case of angle-dispersive experiments. Since the beam has a finite width in the z-direction, at grazing incidence the sample is completely submerged into the beam. As the angle of incidence increases, a larger fraction of the beam hits the sample and the effective incident intensity increases with $\sin(\theta)$. The incident intensity becomes independent on the incident angle only once the entire beam is reflected by the sample, this is achieved when the angle of incidence is larger than a critical value:

$$\theta_{\mathrm{c}} = \arcsin\left(\frac{b_w}{L}\right), \tag{2.34}$$

where b_w is the beam width, L is the size of the sample in the beam direction and the sample has been assumed to be in the center of the beam. To account for the changes in the effective intensity, the reflectivity for incident angles smaller than the critical value must be calculated according to:

$$R(q_z) = \frac{I_{\mathrm{ref}}(q_z)}{I_0(q_z)\sin(\theta)}, \qquad \text{if } \theta < \theta_{\mathrm{c}}. \tag{2.35}$$

This is the so-called footprint correction.

To analyze the PNR data two programs have been used. A modified version of the Superfit package, developed at the Max Planck Institute for Intelligent Systems [73]; and the GenX software, developed by M. Björck and G. Andersson [74].

2.3. X-ray absorption spectroscopy

The x-ray absorption cross-section of an atom depends on the density of the empty states, the charge distribution of the initial and final states and the polarization state of the incident photons. In this section it is shown that the study of the x-ray absorption at the $L_{2,3}$ edges of transition metals for linear and circular polarization provides element-specific information regarding the orbital occupancy and the net spin and orbital moments in the $3d$ levels of the atom.

2.3.1. The photon absorption probability

The electromagnetic radiation contains both electric and magnetic fields and thus interacts with all charges and magnetic moments that exist in a solid. As the nuclei are much heavier than the electrons, the effect of the electromagnetic radiation on the former is negligible and in the study of the interaction of radiation with matter only the latter are taken into account.

The Hamiltonian describing the interaction of electrons in an atom with an electromagnetic field can be written in terms of the vector potential $\boldsymbol{A}(\boldsymbol{r})$ as [75]:

$$
\begin{aligned}
H_{\mathrm{int}} = & -\frac{2e}{2mc^2}\sum_j \boldsymbol{A}^2(\boldsymbol{r}_j) - \frac{e}{mc}\sum_j \boldsymbol{A}(\boldsymbol{r}_j)\cdot\boldsymbol{p}_j \\
& -\frac{e\hbar}{mc}\sum_j \boldsymbol{S}_j\cdot[\nabla\times\boldsymbol{A}(\boldsymbol{r}_j)] - \frac{e^3\hbar}{2mc^4}\sum_j \boldsymbol{S}_j\cdot[\dot{\boldsymbol{A}}(\boldsymbol{r}_j)\times\boldsymbol{A}(\boldsymbol{r}_j)].
\end{aligned}
\tag{2.36}
$$

Here $\boldsymbol{r}_j$, $\boldsymbol{p}_j$ and $\boldsymbol{S}_j$ are the position, momentum and spin operators of the j-th electron in the atom, respectively. The first term in equation 2.36 describes the electromagnetic field itself, the second term accounts for the effect of the electric field on the electron motion, the third

term contains the coupling between the radiation and the spin and, finally, the fourth term accounts for the spin-orbit coupling.

The vector potential can be written in terms of the photon annihilation ($b_{k\alpha}$) and creation ($b_{k\alpha}^{\dagger}$) operators:

$$\boldsymbol{A}(\boldsymbol{r}) = \sum_{\boldsymbol{k},\alpha} \left(\frac{2\pi\hbar c^2}{V\omega_{\boldsymbol{k}}}\right)^{1/2} \left(\boldsymbol{e}_{\boldsymbol{k}\alpha} b_{\boldsymbol{k}\alpha} e^{i\boldsymbol{k}\cdot\boldsymbol{r}} + \boldsymbol{e}_{\boldsymbol{k}\alpha}^* b_{\boldsymbol{k}\alpha}^{\dagger} e^{-i\boldsymbol{k}\cdot\boldsymbol{r}}\right). \tag{2.37}$$

where $\boldsymbol{k}$ is the photon wave vector. The photon energy is given by $\hbar\omega_{\boldsymbol{k}} = \hbar c k$ and its polarization is given, in general, by two polarization vectors $\boldsymbol{e}_{\boldsymbol{k}\alpha}$ ($\alpha = 1, 2$). V is the volume of the system. The vector potential is thus linear in $b_{\boldsymbol{k}\alpha}$ and $b_{\boldsymbol{k}\alpha}^{\dagger}$ and only the terms in the Hamiltonian (2.36) which are linear in $\boldsymbol{A}$ contribute to the absorption. The quadratic terms describe two-photon processes and account for the photon scattering.

The interaction of the electromagnetic radiation and the spin do not play a significant role in the core-valence electronic transitions. Therefore, only the $H_1 = -(e/mc)\sum_j \boldsymbol{A}(\boldsymbol{r}_j) \cdot \boldsymbol{p}_j$ term in the Hamiltonian will be considered to calculate the transition probabilities. Using the explicit expression of the vector potential this term can be written as:

$$H_1 = -\frac{e}{mc}\sum_j \boldsymbol{A}(\boldsymbol{r}_j) \cdot \boldsymbol{p}_j = -\frac{e}{mc}\sum_j \sum_{\boldsymbol{k},\alpha} \left(\frac{2\pi\hbar c^2}{V\omega_{\boldsymbol{k}}}\right)^{1/2} b_{\boldsymbol{k}\alpha} e^{i\boldsymbol{k}\cdot\boldsymbol{r}} \boldsymbol{e}_{\boldsymbol{k}\alpha} \cdot \boldsymbol{p}_j, \tag{2.38}$$

since only absorption processes are considered, the photon creation component of the vector potential has not been included. The next step is to apply the so-called dipolar approximation for which $\boldsymbol{k}\cdot\boldsymbol{r} \ll 1$ and the exponential terms in (2.38) can be approximated by 1. Physically, the approximation assumes that the spatial changes of the electromagnetic field inside the atom can be ignored. Although for hard x-rays this is not valid, in the soft x-ray regime (where the measurements presented on this thesis have been performed) the approximation holds and the H_1 operator is simplified to:

$$H_1 = -\frac{e}{mc}\sum_j \sum_{\boldsymbol{k},\alpha} \left(\frac{2\pi\hbar c^2}{V\omega_{\boldsymbol{k}}}\right)^{1/2} b_{\boldsymbol{k}\alpha} \boldsymbol{e}_{\boldsymbol{k}\alpha} \cdot \boldsymbol{p}_j. \tag{2.39}$$

Fermi's Golden Rule states that the probability per unit time for the system to pass from an initial state Ψ_i to a final state Ψ_f by absorbing an incident photon with energy $\hbar\omega$ is given by:

$$W_{fi} = \frac{2\pi}{\hbar}|\langle\Psi_f|T|\Psi_i\rangle|^2\delta(E_f - E_i - \hbar\omega), \tag{2.40}$$

where E_i and E_f are the initial and final state energies, respectively. The initial and final states include a photon component which is not explicit. T is the transition operator which to first order can be approximated by $T \approx H_1$ [76]. Inserting the operator in (2.39) into (2.40), the probability to absorb a photon with energy $\hbar\omega$ is found as:

$$W_{fi} \propto \sum_j \sum_\alpha |\langle\Psi_f|\boldsymbol{e}_\alpha \cdot \boldsymbol{p}_j|\Psi_i\rangle|^2\delta(E_f - E_i - \hbar\omega). \tag{2.41}$$

In the last expression only photons with energy $\hbar\omega_{\boldsymbol{k}} = \hbar\omega$ have been considered in the expansion of the vector potential. The photon component of the initial and final states satisfies $\langle\Psi_f|b_\alpha|\Psi_i\rangle \propto \sqrt{I_0}$, where I_0 is the incident photon intensity. Therefore, the matrix elements of the photon annihilation operator introduce the proportionality between the transition rate and the intensity of the radiation. In addition, the transition probability can be written in terms of the position operators $\boldsymbol{r}_j$ by using the Heisenberg relation, $[\boldsymbol{r}_j, H] = (i\hbar/m)\boldsymbol{p}_j$ to yield [76]:

$$W_{fi} \propto \sum_j \sum_\alpha |\langle\Psi_f|\boldsymbol{e}_\alpha \cdot \boldsymbol{r}_j|\Psi_i\rangle|^2\delta(E_f - E_i - \hbar\omega). \tag{2.42}$$

In the absorption process one hole is created in a core state and one electron occupies an empty state. Assuming that neither the wavefunctions of the passive electrons nor the ones of the empty states are modified by the created core-hole, the probability W_{fi} can be written in terms of the single-particle transition probabilities [54]:

$$T_{fi} \propto \sum_{\alpha} |\langle \phi_f | \boldsymbol{e}_{\alpha} \cdot \boldsymbol{r}_j | \phi_i \rangle|^2 \delta(E_f - E_i - \hbar\omega), \tag{2.43}$$

where T_{fi} is the probability for an electron to be excited from a state ϕ_i to a state ϕ_f by absorbing a photon with energy $\hbar\omega$ and polarization given by the vectors $\boldsymbol{e}_{\alpha}$. The matrix elements of the $\boldsymbol{e}_{\alpha} \cdot \boldsymbol{r}_j$ operator depend on the projection of the electron wavefunction in the polarization direction of the initial and the final states. This gives rise to the so-called search light effect, the likeness of an electromagnetic field to excite electrons into a given empty state ϕ_f depends on the extension of its wavefunction in the direction of polarization [77]. The study of the absorption for radiation with different polarization directions thus provides information about the spatial distribution of the empty states in an atom. In this thesis this effect will be used to study the occupation of the Cu-3d and Mn-3d orbitals in cuprate/manganite superlattices.

The photon carries a total angular momentum $l_p = 1$ which must be added in the absorption process to the initial orbital momentum of the electron system l_i. The final total orbital momentum l_f must therefore satisfy:

$$|l_i - 1| < l_f < l_i + 1. \tag{2.44}$$

The parity of the dipole operator $\boldsymbol{e}_{\alpha} \cdot \boldsymbol{r}_j$ introduces an additional constraint between the initial and final electron states. In a simplified picture, the electron states in a solid can be regarded as simple atomic orbitals for which the parity is given by the angular momentum quantum number, l. Since the electric dipole operator is odd, the matrix element $\langle \phi_f | \boldsymbol{e}_{\alpha} \cdot \boldsymbol{r}_j | \phi_i \rangle$ is non-zero only if the final and initial states have a different parity. Therefore $l_i \neq l_f$ and the dipole transition selection rule reads [78]:

$$\Delta l = l_f - l_i = \pm 1. \tag{2.45}$$

The projection of the photon angular momentum along the photon propagation direction, m_{l_p}, depends on the polarization. In the absorption process this angular momentum is transferred to the system and the projection of the orbital momentum along the beam direction, m_l, of the initial and final states must satisfy:

$$\Delta m_l = 0, \pm 1. \tag{2.46}$$

Since the transition operator does not depend on the spin, the electronic transitions do not affect the spin state yielding:

$$\begin{aligned} \Delta s &= 0, \\ \Delta m_s &= 0. \end{aligned} \tag{2.47}$$

The selection rules in (2.45), (2.46) and (2.47) introduce an additional dependence of the transition probability on the electronic state of the atom. In the particular case of transition metals they give rise to the magnetic circular dichroism effect which is discussed in section 2.3.3.

The x-ray absorption coefficient is proportional to the summation over all possible initial and final states of the one-electron transition probabilities T_{ij}, and the δ function in (2.43) describes the density of unoccupied states with energy $E_f = E_i + \hbar\omega$. In the soft x-ray regime the absorption dependence on the energy is governed by the transition of electrons from the bound states to the continuum. It decreases smoothly with energy following an approximate $1/\omega^3$ dependence [79]. When increasing the energy above the binding energy of a core level, a new channel of transitions opens up and the absorption increases abruptly yielding a so-called absorption edge. The transitions can also occur to the empty high-energy bound states.

These states can have a large enough density to give rise to strong peaks in the absorption at the position of the absorption edge, the so-called white lines. As discussed in sections 2.3.2 and 2.3.3, for the first series of transition metals the variation in the intensity of the white lines with the photon polarization is directly linked to the orbital occupancy and the magnetic ordering in the partially filled $3d$ band.

Since the final states are excited states, the x-ray absorption spectroscopy cannot be considered a reliable method to probe the energy distribution of the electron states in the ground state. The interaction of the excited electrons with the created core-hole and with the passive electron can lead to significant shifts and distortions of the white lines. The total intensity of the white lines is related to the transition probabilities and thus depends only on the density of empty states in the ground state. Therefore, it can be quantitatively studied using x-ray absorption measurements [80].

2.3.2. X-ray linear dichroism

The x-ray linear dichroism (XLD) is based on the change of the absorption of linearly polarized x-rays with the polarization direction. Schematically, the origin of the XLD can be understood in terms of the already mentioned search light effect. The incident radiation induces oscillations of the electrons in the direction of the electric field (polarization direction) and therefore the electrons are preferably excited to states that are well extended in this direction. To quantify the influence of the x-ray polarization on the absorption for a particular system, the matrix elements in equation 2.43 must be calculated for all possible initial and final states and the corresponding transition probabilities summed up.

For this thesis the study of the electric and magnetic properties of the Mn and Cu ions is of foremost interest. These two atoms belong to the first series of transition metals and the discussion in this section is restricted to this group. For this family of ions the electric and magnetic properties are largely linked to the characteristics of their partially filled $3d$ orbitals. These characteristics can be indirectly studied by examining the x-ray absorption induced $2p \rightarrow 3d$ transition. Due to the strong $2p$ spin-orbit coupling in these atoms the degeneracy of this level is broken. Two levels, namely $2p_{3/2}$ and $2p_{1/2}$, with total angular momentum $j = 3/2$ and $j = 1/2$, respectively, are thus created. The energy separation between these levels is proportional to the spin-orbit coupling and amounts to approximately 11 eV and 20 eV for Mn and Cu, respectively. The transitions from the $2p_{3/2}$ and $2p_{1/2}$ levels to the continuum give rise to two edges in the energy dependent x-ray absorption, namely L_3 and L_2. For the YBCO, LCMO and LMO compounds studied in this thesis, the $3d$ levels are in the vicinity of the Fermi level and therefore the intensity of the white lines at the $L_{3,2}$ absorption edges is proportional to the $2p \rightarrow 3d$ transition probabilities. Although $2p \rightarrow 4s$ transitions are also possible, their corresponding transition probabilities are about 30 times smaller than for the $2p \rightarrow 3d$ ones [81]. These transitions will not be considered in the following discussion.

For each edge a total of $2j+1$ starting states, corresponding to the different possible values of m_j, contribute to the absorption. Neglecting the spin orbit coupling in the $3d$ band, the final states can be described by the 5 levels corresponding to different values of m_l. These levels are usually combined to create a set of real wavefunctions corresponding to the $3d_{x^2-y^2}$, $3d_{3x^2-r^2}$, $3d_{xy}$, $3d_{xz}$ and $3d_{yz}$ orbitals. This set of real orbitals, $3d_i$, will be used from now on in the discussion. Noting the initial and final levels as $|2p_{j,m_j}\rangle$ and $|3d_i\rangle$, the total x-ray absorption probability at the L_j edge for light linearly polarized in direction α can be calculated as:

$$\mu_\alpha(\omega) = C \sum_{m_j=-j}^{j} \sum_i |\langle 2p_{j,m_j}|\boldsymbol{e}_\alpha \cdot \boldsymbol{r}|3d_i\rangle|^2 \delta_i(E_{p_j} - E_d - \hbar\omega), \tag{2.48}$$

where C is a proportionality constant and $\boldsymbol{e}_\alpha$ is an unitary vector in the polarization direction. E_{p_j} and E_d are the energies of the $2p_j$ and $3d$ levels, respectively. The i-index in the δ function has been included to specify that it is related to the density of free states of each $3d$ orbital. If integrated over the energy range around the absorption edge, the δ_i function becomes simply

the number of holes in the orbital i, $\underline{n}_i$, and one gets:

$$\int_{L_j} \mu_\alpha(\omega)\mathrm{d}\omega = C\sum_i \left[\sum_{m_j=-j}^{j} |\langle 2p_{j,m_j}|\boldsymbol{e}_\alpha \cdot \boldsymbol{r}|3d_i\rangle|^2\right]\underline{n}_i = C\sum_i P_{i,\alpha}\underline{n}_i. \tag{2.49}$$

The total intensity of the white line can thus be regarded as an addition of the contributions from each of the $3d$ orbitals. The weight of each orbital in the white line is given by the summation of the transition rates over the $2p$ levels:

$$P_{i,\alpha} = \sum_{m_j=-j}^{j} |\langle 2p_{j,m_j}|\boldsymbol{e}_\alpha \cdot \boldsymbol{r}|3d_i\rangle|^2. \tag{2.50}$$

To calculate the value of $P_{i,\alpha}$ for different orbitals and polarizations the spherical coordinates representation is useful because it allows one to write all angular dependence in terms of spherical harmonic functions. For example, the transition operator for an arbitrary polarization direction can be written as:

$$\boldsymbol{e}_\alpha \cdot \boldsymbol{r} = re_x \sin\theta\cos\phi + re_y\sin\theta\sin\phi + re_z\cos\theta,$$
$$= r\sqrt{\frac{4\pi}{3}}\left[e_x\frac{(Y_1^{-1}-Y_1^1)}{\sqrt{2}} + e_y\frac{(Y_1^{-1}+Y_1^1)}{\sqrt{2}} + e_zY_1^0\right] \tag{2.51}$$

where Y_n^m is the spherical harmonic of degree n and order m, its dependence on the θ and ϕ coordinates is implicit. Being combinations of the eigenstates of the orbital momentum, the d_i orbitals can be represented in terms of spherical harmonics of second degree. Although the $|2p_{j,m_j}\rangle$ states are not eigenstates of the orbital moment, using the Clebsh-Gordon coefficients they can be written as combinations of the pure $|2p_{l,m_l,m_s}\rangle$ states for which the angular part is also written in terms of the spherical harmonics of first order [79]. Therefore, the matrix elements in (2.49) involve the multiplication of three spherical harmonics and can be evaluated without mayor difficulties. The radial part of the integral does not depend on the initial or final values of the angular momentum and becomes a common pre-factor.

The resulting transition probabilities for different polarization directions are shown in Figure 2.8 and were obtained from Ref. [82]. As seen in the figure, the transition probability vanishes when the polarization is directed along the nodal direction of an orbital and is maximized when there is the largest probability of finding an electron along the polarization direction. The search-light effect is thus quantified and replacing the calculated values of $P_{i,\alpha}$ in equation (2.49) the so-called charge distribution sum rules are obtained [82, 83]:

$$\int_{L_3+L_2}\mu_x\mathrm{d}\omega = \frac{C}{12}\left[6(\underline{n}_{xy}+\underline{n}_{xz}+\underline{n}_{x^2-y^2})+2\underline{n}_{3z^2-r^2}\right], \tag{2.52a}$$

$$\int_{L_3+L_2}\mu_y\mathrm{d}\omega = \frac{C}{12}\left[6(\underline{n}_{xy}+\underline{n}_{yz}+\underline{n}_{x^2-y^2})+2\underline{n}_{3z^2-r^2}\right], \tag{2.52b}$$

$$\int_{L_3+L_2}\mu_z\mathrm{d}\omega = \frac{C}{12}\left[6(\underline{n}_{xz}+\underline{n}_{yz})+8\underline{n}_{3z^2-r^2}\right]. \tag{2.52c}$$

Here μ_α is the measured absorption for polarization in the $\alpha = x, y, z$ direction. This result is general and is not affected by the strong core-hole interactions that affect only the shape of the absorption peaks. It can, nevertheless, suffer modifications if the sample is magnetic and a large spin-orbit interaction takes place in the $3d$-band [82]. This effect is known as x-ray magnetic linear dichroism [84, 85] and its origin is accounted for by the magnetic term $\boldsymbol{S}_j \cdot [\nabla \times \boldsymbol{A}(\boldsymbol{r}_j)]$ in the interaction Hamiltonian of equation (2.36). Owing to the relatively small orbit-coupling in Cu and Mn this effect is expected to be negligible and will not be further discussed.

In equations 2.52, the integral comprises both the L_3 and L_2 edges. This is due to the fact that in most transition metals the strong core-valence interactions lead to a mixing of the L_2
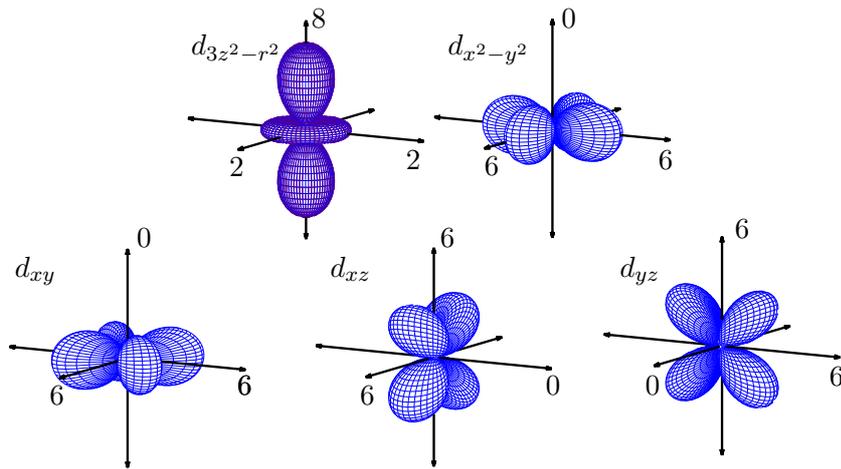
Figure 2.8: Transition probabilities from the $2p$ band to the $3d$ orbitals for different polarization directions. The arrows mark the direction of the x-ray polarization, the numbers represent the corresponding transition probability and have been taken from Ref. [82].

and L_3 white lines and in practice it is often not possible to isolate them [86, 87]. Nevertheless, for Cu there is only one hole in the initial and final configuration, the core-valence interactions are absent and the white lines are sharp and well separated. The L_3 and L_2 white lines can be separated and their contributions to the absorption are linked as:

$$\int_{L_3} \mu_\alpha d\omega = 2 \int_{L_2} \mu_\alpha d\omega = \frac{2}{3} \int_{L_3+L_2} \mu_\alpha d\omega. \tag{2.53}$$

The L_3 and L_2 bands therefore contain the same information regarding the orbital occupation. The density of states at the $2p_{3/2}$ band is twice as large as at the $2p_{1/2}$ band and therefore its contribution to the absorption is twice as large.

The integral over the $L_{3,2}$ edges of the polarization-averaged absorption, defined as $\overline{\mu} = (\mu_x + \mu_y + \mu_z)/3$, can be calculated using the expressions (2.52) to yield an important relation:

$$\int_{L_3+L_2} \overline{\mu} d\omega = \frac{C}{3}(\underline{n}_{xy} + \underline{n}_{xz} + \underline{n}_{yz} + \underline{n}_{x^2-y^2} + \underline{n}_{3x^2-r^2}) = \frac{C}{3}\underline{n}_{3d}. \tag{2.54}$$

This quantity is thus independent of the occupation anisotropy and is proportional to the number of holes in the $3d$ band, $\underline{n}_{3d}$. As long as the hole density in the $3d$ band is known, equation (2.54) allows for the determination of the proportionality constant C.

Charge distribution sum rules for Mn and Cu

In the following the charge distribution sum rules are applied to Mn and Cu. As mentioned in section 2.1.1, the electronic configuration of the $3d$ band in stoichiometric $La_{2/3}Ca_{1/3}MnO_3$ is dominated by the crystal field splitting between the t_{2g} and e_g bands. The lower t_{2g} band is half-filled with one electron occupying each of the d_{xy}, d_{yz} and d_{xy} orbitals. The remaining $2/3$ electron density is distributed between the two e_g orbitals. Whether the electrons in the e_g band sit preferably in the $d_{x^2-y^2}$ or the $d_{3z^2-y^2}$ orbitals depends on the distortions of the O octahedron around the Mn ions.

The orbital polarization of the e_g band of LCMO can be determined from x-ray absorption measurements as follows. For this discussion the x, y and z axis are linked to the crystallographic a, b and c axis, respectively. For Mn, the charge distribution sum rules in

equation (2.52) read:

$$\int_{L_3+L_2} \mu_a \mathrm{d}\omega = \frac{C}{12} \left[6(2 + \underline{n}_{x^2-y^2}) + 2\underline{n}_{3z^2-r^2} \right], \tag{2.55a}$$

$$\int_{L_3+L_2} \mu_b \mathrm{d}\omega = \frac{C}{12} \left[6(2 + \underline{n}_{x^2-y^2}) + 2\underline{n}_{3z^2-r^2} \right], \tag{2.55b}$$

$$\int_{L_3+L_2} \mu_c \mathrm{d}\omega = \frac{C}{12} \left[12 + 8\underline{n}_{3z^2-r^2} \right]. \tag{2.55c}$$

In thin films, like the ones studied in this thesis, twinning effects lead to the mixing of the a and b crystallographic axis. Typically only the averaged absorption $\mu_{ab} = (\mu_a + \mu_b)/2$ is available experimentally. From equations (2.55) it becomes clear that this limitation has no consequence for Mn for which the t_{2g} band is exactly half-filled such that the intensity of the white lines in μ_a, μ_b and thus in μ_{ab} is identical. The auxiliary parameter A is defined as the normalized difference between the integrals of μ_{ab} and μ_c:

$$A = \frac{2\int_{L_3+L_2}(\mu_{ab} - \mu_c)\mathrm{d}\omega}{\int_{L_3+L_2}(2\mu_{ab} + \mu_c)\mathrm{d}\omega} = \frac{\underline{n}_{x^2-y^2} - \underline{n}_{3z^2-r^2}}{\frac{19}{3}} = \frac{3}{19}(\underline{n}_{x^2-y^2} - \underline{n}_{3z^2-r^2}). \tag{2.56}$$

In the last expression the numerator has been evaluated by using the expressions (2.55), for the denominator the property (2.54) has been applied assuming a hole density in the $3d$ band of $\underline{n}_{3d} = 19/3$. The sum of $\underline{n}_{x^2-y^2}$ and $\underline{n}_{3z^2-r^2}$ is equal to the hole density in the e_g band:

$$\underline{n}_{x^2-y^2} + \underline{n}_{3z^2-r^2} = \frac{10}{3}. \tag{2.57}$$

Combining the last two equations, the occupancy of the $3d_{3z^2-r^2}$ and $3d_{x^2-y^2}$ orbitals in terms of the measured intensity of the white lines are obtained as:

$$\underline{n}_{3z^2-r^2} = \frac{10 + 19A}{6}, \tag{2.58a}$$

$$\underline{n}_{x^2-y^2} = \frac{10 - 19A}{6}. \tag{2.58b}$$

Since the electrons are minority in the e_g band, the asymmetry in the occupation of the two e_g orbitals is better expressed in terms of the *electron* orbital polarization, P_{e_g}, defined as:

$$P_{e_g} = \frac{n_{3z^2-r^2} - n_{x^2-y^2}}{n_{3z^2-r^2} + n_{x^2-y^2}} = \frac{\underline{n}_{x^2-y^2} - \underline{n}_{3z^2-r^2}}{\frac{2}{3}} = \frac{19A}{2}, \tag{2.59}$$

where n_i is now the electron density in the i orbital.

The same procedure can also be applied to Cu. For optimally doped YBCO the valence state of the Cu ions in the planes and in the chains is close to $+2$ with one hole in the $3d$ band [53]. In YBCO the crystal field also splits the $3d$ band into the t_{2g} and e_g bands. In addition, the large Jahn-Teller distortion of the CuO_2 pyramids leads to a large orbital polarization which favors the occupation of the out-of-plane $3d_{3z^2-r^2}$ orbital. As discussed in section 3.4, important changes in the orbital polarization occur at the interface. The method presented here allows the quantification of these changes.

The first assumption is that the $3d$ hole in Cu resides in the e_g band. This is well justified by the strength of the crystal field ($\sim 2\,\mathrm{eV}$). The hole density in the t_{2g} band is therefore zero and equations (2.52) read:

$$\int_{L_3+L_2} \mu_{ab} \mathrm{d}\omega = \frac{C}{6} \left[3\underline{n}_{x^2-y^2} + \underline{n}_{3z^2-r^2} \right], \tag{2.60a}$$

$$\int_{L_3+L_2} \mu_c \mathrm{d}\omega = \frac{C}{6} \left[4\underline{n}_{3z^2-r^2} \right]. \tag{2.60b}$$

Here $\mu_{ab} = (\mu_a + \mu_b)/2$ and again the identical white line intensity for μ_a and μ_b has been assumed. In the case of Cu, holes are minority in the e_g band and the differences in the orbital occupation are better described in terms of the *hole* orbital polarization.

$$\underline{P}_{e_g} = \frac{\underline{n}_{x^2-y^2} - \underline{n}_{3z^2-r^2}}{\underline{n}_{x^2-y^2} + \underline{n}_{3z^2-r^2}} = \frac{2 \int_{L_3+L_2}(\mu_{ab} - \mu_c)\mathrm{d}\omega}{\int_{L_3+L_2}(2\mu_{ab} + \mu_c)\mathrm{d}\omega} = A. \tag{2.61}$$

It should be remarked that the absorption integrated in equations (2.59) and (2.61) corresponds only to the intensity of the white lines. The non-resonant components of the absorption must therefore be subtracted from the experimental data. These non-resonant components include the absorption from other elements in the sample and the absorption edges.

2.3.3. X-ray circular dichroism

In a x-ray circular dichroism (XMCD) experiment one determines the change of the x-ray absorption with the helicity of circularly polarized photons. As was first observed by Schütz *et al.*, the magnitude of the XMCD in transition metals can be related to the magnitude of the spin and orbital magnetic moments of the atoms that are probed by the resonant transition [88].

To understand the origin of the XMCD effect one needs to recall that for circularly polarized photons the projection of the photon angular momentum in the propagation direction is $m_{l_p} = \pm 1$. This momentum must be transferred to the excited electron in the absorption process and the selection rule reads:

$$\Delta m_l = \pm 1. \tag{2.62}$$

The sign of the projection depends on the helicity of the photon which in this thesis will be defined as *positive* when the photon orbital moment is *antiparallel* to the applied field.

In the absence of spin-orbit coupling in the $2p$ band, all the states with different projections of the orbital and spin moments are degenerate. The transition probability only depends on the initial and final values of the orbital moment, m_l, according to the transition rate T_{fi} of equation (2.43). Since the spin is not involved in the interaction, the electrons with spin parallel and antiparallel to the photon angular momentum are excited with the same probability.

If there a spin-orbit interaction in the $2p$ band, as for transition metals, the spin and orbital momentum of the electrons are coupled and as a consequence the excited electrons are spin-polarized. The origin of this spin polarization is sketched in Figure 2.9. The incident photon is assumed to have a positive helicity and for simplicity the $3d$ band is assumed to be empty. In the ground state only the total angular momentum, m_j, is well defined. For each m_j, the electron state is a combination of $|m_l, m_s\rangle$ states with orbital, m_l, and spin, m_s, moments satisfying $m_l + m_s = m_j$. The contribution of each initial state $|m_l, m_s\rangle$ to the absorption probability is given by the multiplication of the probability of finding an electron in this initial state, given by the Clebsh-Gordon coefficients, and the transition probability to the $|m_l + 1, m_s\rangle$ state in the $3d$ band, given by T_{if}. The thickness of the arrows in the figure is proportional to the contribution of each initial state to the absorption probability and the color is associated with the spin projection of the excited electron. It becomes evident that for photons with positive helicity the excited electrons at the $2p_{3/2}$ and $2p_{1/2}$ bands have a predominant spin up ($m_s = 1/2$) and spin down ($m_s = -1/2$) character, respectively. An identical analysis shows that the spin polarization is exactly opposite if the incident photon has a negative helicity. Quantitatively, in the $2p_{3/2}$ band 62.5% and 37.5% of the excited electrons have their spin parallel and antiparallel, respectively, to the photon angular momentum. In the $2p_{1/2}$ band the same probabilities yield 25% and 75% [77].

An additional modulation to the transition probability must be taken into account if the $3d$ band is partially filled. In the following it is assumed that an external magnetic field is applied to the sample. If the sample is magnetic the majority of the electrons in the $3d$ band will have their spin pointing antiparallel to the applied field. This is due to the fact that the
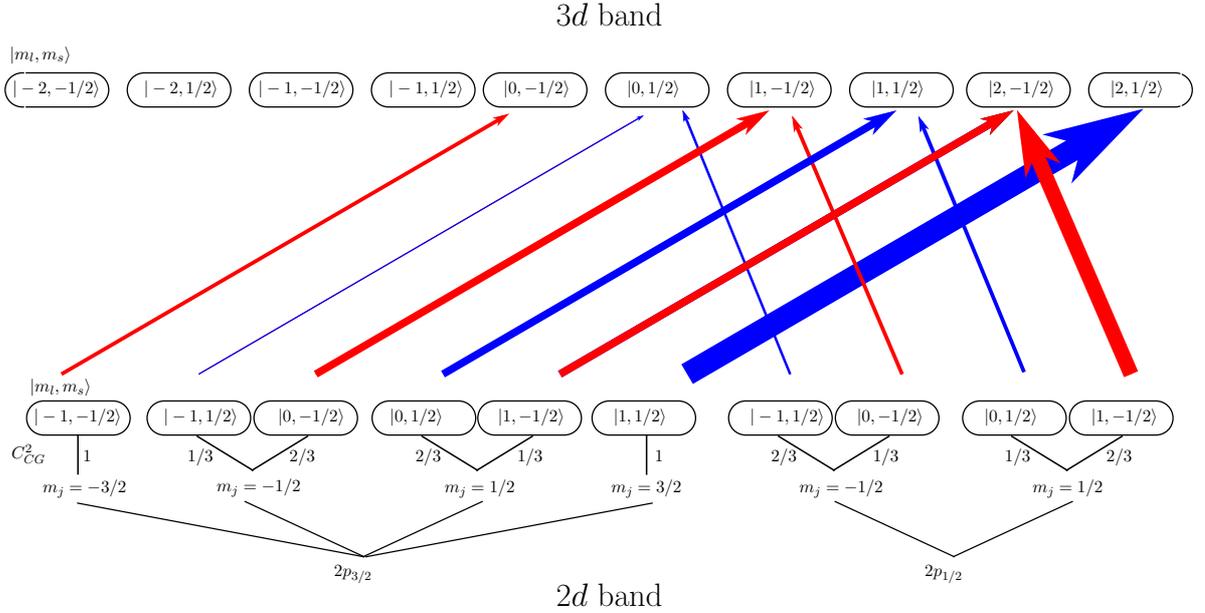
$3d$ band

Figure 2.9: Origin of the spin polarization of the excited electrons in the $2p \to 3d$ transition induced by circularly polarized photons. The incident photon helicity has been set to $+1$. For each m_j, the probability of finding an electron in the state $|m_l, m_s\rangle$ is given by the square of the Clebsh-Gordon coefficient, C_{CG}. The transition probability from a $|m_l, m_s\rangle$ state in the $2p$ band to a $|m_l+1, m_s\rangle$ state in the $3d$ band is given by T_{fi}. The arrows show only transition possible for each initial state $|m_l, m_s\rangle$, the thickness of the arrow is proportional to the contribution of the corresponding transition to the total absorption. The arrows are red (blue) when they involve electrons with spin parallel (antiparallel) to the photon angular moment.

electron spin and magnetic moment are antiparallel. The transition of electrons with spin antiparallel to the applied field becomes less likely than for electrons with spin parallel. The absorption probability therefore depends on the predominant spin orientation of the excited electrons and is different for photons with positive and negative helicity. The XMCD is defined as the difference between the absorption for positive and negative photon helicity. At the L_3 edge the absorption is larger for negative helicity and the resulting XMCD is negative. At the L_2 edge the spin polarization is opposite and the absorption is larger for positive helicity, the XMCD is thus negative. The expected shape of a spin-order induced XMCD is shown in Figure 2.10, which has been taken from Ref. [89].

Nevertheless, spin ordering in the $3d$ band is not the only possible source of an XMCD signal. As seen in Figure 2.9, for photons with positive helicity the electrons are excited mainly to $3d$ levels with $m_l \geq 0$. In analogy, for photons with negative helicity the electrons are excited to levels with $m_l \leq 0$. Therefore, if there is a net orbital moment in the $3d$ band and the occupancy of levels with positive and negative m_l is different, the x-ray absorption becomes once again dependent on the photon helicity and a XMCD signal is observed. Since the XMCD in this case is not related to the spin polarization, it has the same sign at both the L_3 and L_2 edges as shown in Figure 2.10.

The anisotropic distribution of the spins in the $3d$ bands also contributes to the XMCD signal. The transition probability from an initial state with a given m_l to final states with m_l+1 and m_l-1 is, in general, different as a consequence of the search-light effect. Therefore if the net spin is different at the $m_l - 1$ and $m_l + 1$ orbitals, an additional contribution to the XMCD will arise. The anisotropy of the spin is written in terms of the magnetic dipole operator $\boldsymbol{T}$ defined as [90]:

$$\boldsymbol{T} = \boldsymbol{S} - 3\hat{\boldsymbol{r}}(\hat{\boldsymbol{r}} \cdot \boldsymbol{S}), \qquad (2.63)$$

where $\boldsymbol{S}$ is the total $3d$ spin operator. As shown in Figure 2.10, the contribution of the magnetic dipole operator to the XMCD has the same distribution over the L_3 and L_2 edges as
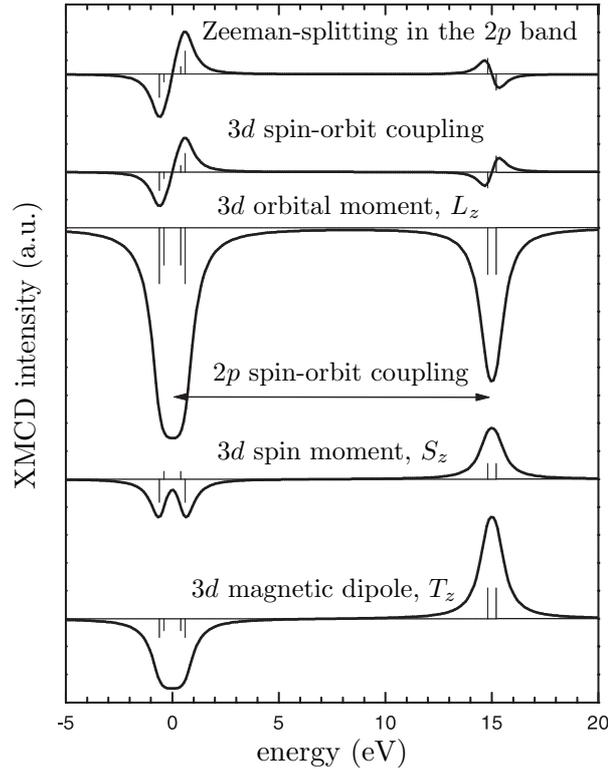
Figure 2.10: Different contributions to the XMCD signal at the L_3 and L_2 edges for the first series of transition metals. Only the contributions from the orbital moment (L_z), the spin moment (m_s) and the magnetic dipole operator (T_z) are non-vanishing after the integration of the XMCD intensity over the L_3 or L_2 edges. The figure has been taken from Ref. [89]

the one due to the spin moments. Therefore, this two contributions cannot be easily separated.

Figure 2.10 also shows that the Zeeman-splitting at the $2p$ band in presence of an applied field, or the spin-orbit coupling at the $3d$ band can lead to XMCD effects. Nevertheless, this contributions cancel-out after integrating the XMCD signal over the L_3 and L_2 edges, therefore they do not contribute to the quantitative analysis of the data.

XMCD sum rules

The intensity of the XMCD signal has been shown to be proportional to the imbalance in the occupation of spin up and spin down states, and to the imbalance in the occupation of states with positive and negative orbital moment. The so-called orbital and spin sum rules relate the integrals of the XMCD over the L_3 and L_2 edges to the net orbital and spin moment as follows [91, 92]:

$$\langle L_j \rangle = -\frac{2}{3} \frac{\int_{L_3+L_2} (\mu_+ - \mu_-) \mathrm{d}\omega}{\int_{L_3+L_2} \frac{\mu_+ + \mu_- + \mu_0}{3} \mathrm{d}\omega} n_{3d} \tag{2.64a}$$

$$\langle S_j \rangle - \frac{7}{2} \langle T_j \rangle = \frac{1}{2} \frac{\int_{L_3} (\mu_+ - \mu_-) \mathrm{d}\omega - 2 \int_{L_2} (\mu_+ - \mu_-) \mathrm{d}\omega}{\int_{L_3+L_2} \frac{\mu_+ + \mu_- + \mu_0}{3} \mathrm{d}\omega} n_{3d} \tag{2.64b}$$

where $\langle L_j \rangle$, $\langle S_j \rangle$ and $\langle T_j \rangle$ are the expectation values of the orbital moment, the spin moment and the magnetic dipole operator, respectively, in the direction of the beam, j. μ_+ and μ_- are the measured absorption for positive and negative helicity, respectively. μ_0 is the measured absorption for x-rays linearly polarized in the direction of the beam. In terms of the absorption for x-rays with circular polarization, the polarization averaged absorption can also be written as $\overline{\mu} = (\mu_+ + \mu_- + \mu_0)/3$ and therefore the factor $n_{3d} / \int_{L_3+L_2} \frac{\mu_+ + \mu_- + \mu_0}{3} \mathrm{d}\omega$ accounts for the unknown proportionality constant between the measured absorption and the transition probability. Once again, in equations (2.64) only the intensity of the white lines

is included in the integrals, in practice all the non-resonant contributions to the absorption must therefore be subtracted.

The validity of the orbital moment sum rule in equation (2.64a) is well accepted. However, some caution is required in applying the corresponding spin sum rule. In the first place, it involves the separated integration of the L_3 and L_2 edges which in practice is not always possible. The strong interactions between the core and valence holes in the excited state can lead to a sizable broadening of the white lines. If the spin-orbit coupling in the $2p$ band is not large enough, the two edges may overlap and a clear boundary between them can not be defined. Carra *et al.* initially proposed that this effect could lead to errors of about 5%, nevertheless, an underestimation of the spin magnetic moment of up to 40% has been reported [93].

Another possible source of error in the determination of the spin moment using the sum rules concerns the value of $\langle T_j \rangle$. As was already mentioned, this operator measures the asphericity of the spin wavefunction in the direction of the beam. Therefore it cannot be dismissed in systems with a large anisotropy. As the anisotropy of the spin and charge distributions are related, the $\alpha = x, y, z$ component of the magnetic dipole operator can be written as [82]:

$$T_\alpha = \sum_\beta Q_{\alpha\beta} S_\beta, \tag{2.65}$$

where $Q_{\alpha\beta} = \delta_{\alpha\beta} - 3\hat{r}_\alpha \cdot \hat{r}_\beta / r^2$ is the quadrupole charge operator and the sum runs over the x, y and z directions. If the $3d$ spin-orbit coupling is small, the off-diagonal terms in the last equation can be dismissed and to first order it is possible to write $T_\alpha = Q_{\alpha\alpha} S_\alpha$. The calculation of the expectation value of T_α includes a summation over all electrons in the $3d$ band that can be written as a summation over the $3d_i$ orbitals [83]:

$$\langle T_\alpha \rangle = \sum_i \langle 3d_i | Q_{\alpha\alpha} | 3d_i \rangle s_\alpha^i, \tag{2.66}$$

where s_α^i is the projection of the spin moment in orbital $3d_i$ in direction α. The trace of $Q_{\alpha\alpha}$ vanishes when calculated over either the t_{2g} or the e_g bands. Since for Mn the spin moment in the t_{2g} band is homogeneous and for Cu it is absent, the contributions to $\langle T_\alpha \rangle$ coming from this band are zero in both cases. The matrix elements in $\langle 3d_i | Q_{\alpha\alpha} | 3d_i \rangle$ in the e_g band can be calculated using the spherical harmonics yielding:

$$\langle 3d_{x^2-y^2} | Q_{xx} | 3d_{x^2-y^2} \rangle = -\langle 3d_{3z^2-r^2} | Q_{xx} | 3d_{3z^2-r^2} \rangle = -\frac{2}{7},$$

$$\langle 3d_{x^2-y^2} | Q_{yy} | 3d_{x^2-y^2} \rangle = -\langle 3d_{3z^2-r^2} | Q_{yy} | 3d_{3z^2-r^2} \rangle = -\frac{2}{7}, \tag{2.67}$$

$$\langle 3d_{x^2-y^2} | Q_{zz} | 3d_{x^2-y^2} \rangle = -\langle 3d_{3z^2-r^2} | Q_{zz} | 3d_{3z^2-r^2} \rangle = \frac{4}{7}.$$

Recalling that the x, y, z coordinates correspond to the a, b, c crystallographic axes, respectively, the expectation value of the magnetic dipole operator for an XMCD measurement with the incident beam aligned along the ab-plane or along the c-axis can be written as:

$$\langle T_{ab} \rangle = -\frac{2}{7}(s_{ab}^{x^2-y^2} - s_{ab}^{3z^2-r^2}), \tag{2.68}$$

$$\langle T_c \rangle = \frac{4}{7}(s_c^{x^2-y^2} - s_c^{3z^2-r^2}). \tag{2.69}$$

It is possible to extend this results for an arbitrary direction. If the incident beam points along the j-direction, which forms an angle θ with respect to the ab plane, the effective matrix elements of the quadrupole operator satisfy $Q_j = (\langle Q_{xx} \rangle + \langle Q_{yy} \rangle) \cos^2 \theta / 2 + \langle Q_{zz} \rangle \sin^2 \theta$ [82]. An identical angular dependence is obtained for $\langle T_j \rangle$ and the correction to the spin moment due to the spin anisotropy can be written as [94]:

$$\langle S_j \rangle + \frac{7}{2} \langle T_j \rangle = \langle S_j \rangle + (s_j^{x^2-y^2} - s_j^{3z^2-r^2})(3 \sin^2(\theta) - 1), \tag{2.70}$$

where s_j^i is the projection of the spin in orbital $3d_i$ in direction j. The size of $\langle T_j \rangle$ is therefore proportional to the spin anisotropy and will be important in systems with a large orbital polarization. Furthermore, the sign of the correction changes when going from normal to grazing incidence, the spin anisotropy can thus be measured by performing XMCD measurements with different incidence angles.

2.3.4. Setting up a XAS experiment

Since a x-ray source with a tunable energy is needed to perform the x-ray absorption spectroscopy (XAS) measurements, this experiment must be performed at a synchrotron facility. At the XTreme beamline of the Swiss Light Source, where all the XAS experiments reported in this thesis have been performed, a 2.4 GeV electron beam is directed towards an undulator system where the electrons perform an oscillating motion and thus radiate high-energy photons. The energy distribution and the polarization of the radiated x-rays depend on the gap and the shift between the two undulator magnets. The former controls the frequency of the oscillations, the latter controls the orientation of the oscillatory movement. A monochromatic beam is obtained with a mirror-grating system that introduces an energy-independent beam deflection [95]. The monochromatic beam is then focused onto the sample. Since soft x-rays are easily absorbed in air, the entire setup needs to be kept at ultra-high-vacuum conditions.

The absorption of the sample is measured indirectly by detecting the decay process of the excited ions. In the decay process one of the valence electrons falls to the empty state in the core, the energy excess can be released either by ejecting an Auger electron from the atom or by emitting a fluorescence photon.

The Auger electrons are scattered in the sample and may release further electrons in the material giving rise to a secondary electron cascade. If the excited ion is close enough to the surface, the emitted electrons may leave the sample which thus becomes charged. If the sample is grounded, its charge is balanced by a net electron flow toward the sample which can be measured as an electric current. This current is thus proportional to the number of excited atoms in the sample per unit time and, neglecting saturation effects, to the x-ray absorption cross section [96, 97]. This measurement mode is the so-called total electron yield (TEY). Since the electrons are strongly scattered in the sample, they rapidly loose their excess kinetic energy. Accordingly, their probability to leave the sample decays exponentially with the depth from the sample surface. The characteristic length scale of the escape depth is on the order of some nanometers. Its exact value depends on the electric properties of the probed material. The TEY mode is thus a very surface sensitive technique.

The emitted fluorescence photons can be measured by locating a photodiode in the vicinity of the sample. The characteristic length of the fluorescence photon extinction in the sample is on the order of 100 nm, therefore the so-called fluorescence yield (FY) method is considered a bulk sensitive technique. The current in the photodiode is proportional to the absorption cross-section only if the total absorption cross-section of the sample does not change drastically at the absorption edge, i.e. it works only in dilute samples [98]. In the XTreme setup the photodiode is positioned on the scattering plane at an angle of 90° with respect to the beam direction.

The intensity of the incident beam depends on the photon energy. To correct for this variation, the incident beam intensity is indirectly determined by measuring the TEY in a thin gold mesh that is located on the beam path before the sample. Gold has no absorption edges in the soft x-ray range and its absorption is therefore small and almost constant within the energy range of a measurement (~ 70 eV). The final TEY and FY signals are thus determined after normalizing the measured currents by the TEY current in the gold mesh.

Chapter 3

Magnetic proximity effect in a YBCO/LCMO superlattice

In this chapter the phenomenology of the Magnetic Proximity Effect of an almost symmetric $[\mathrm{YBa_2Cu_3O_7}(9.7\,\mathrm{nm})/\mathrm{La_{2/3}Ca_{1/3}MnO_3}(9.4\,\mathrm{nm})]_{10}$ superlattice is introduced. Details on the growth and the structural characterization of the epitaxial samples are described in section 3.1; the epitaxial growth of the film and its strain condition are confirmed by x-ray diffraction. Section 3.2 presents the electric and magnetic properties of the superlattice. It shows resistivity and magnetization measurements which establish that the individual layers retain their superconducting and ferromagnetic properties with critical temperatures of $T_\mathrm{C} \approx 88\,\mathrm{K}$ and $T^\mathrm{Curie} \approx 200\,\mathrm{K}$, respectively. The polarized neutron reflectometry (PNR) measurements and their modeling are discussed in section 3.3. It shows that the reflectivity curves are best described in terms of a strong suppression of the magnetization on the $\mathrm{La_{2/3}Ca_{1/3}MnO_3}$ (LCMO) side of the superlattice. The x-ray linear and circular dichroism results are presented in sections 3.4 and 3.5, respectively; while the circular dichroism confirms that a ferromagnetic Cu moment is induced on the $\mathrm{YBa_2Cu_3O_7}$ (YBCO) side of the interface, the linear dichroism provides evidence for a reconstruction of the Cu-$3d$ orbitals at the interface. Some results of the x-ray resonant magnetic reflectometry (XRMR) analysis are briefly discussed in section 3.6; the Cu moments are shown to be located on the YBCO side of the interface and the coupling between the Cu and Mn moments is confirmed. Finally, the concluding remarks are presented in section 3.7

3.1. Sample growth and structural characterization

The $[\mathrm{YBa_2Cu_3O_7}(9.7\,\mathrm{nm})/\mathrm{La_{2/3}Ca_{1/3}MnO_3}(9.4\,\mathrm{nm})]_{10}$ superlattice, from now on referred to as sample YLCM, was grown on a $\mathrm{La_{0.3}Sr_{0.7}Al_{0.65}Ta_{0.35}O_3}$ (LSAT) substrate by means of pulsed laser deposition (PLD). The PLD technique allows for a monolayer by monolayer growth of heteroepitaxial multilayers with very flat interfaces.

In PLD a pulsed laser beam is focused onto a target that has the stoichiometry of the desired film. Due to the high intensity of the laser pulse, the target is ablated and a plasma plume that expands from the target surface toward the substrate is created. The shape, size and stoichiometry of the plume depend on the laser energy, the spot size, and the background gas pressure in the growth chamber. The ions from the plume that arrive on the substrate can crystallize and start growing an epitaxial thin film. Such a crystalline growth can be achieved if the substrate is heated to a suitable temperature and if its crystallographic properties are suitable. The monolayer by monolayer growth can be controlled and monitored during the growth with *in situ* reflection high-energy electron diffraction (RHEED) [99].

For sample YLCM a laser fluence of about $2\,\mathrm{J/cm^2}$ per $25\,\mathrm{ns}$ pulse at the target surface was used. The sample was grown at $825\,^\circ\mathrm{C}$ in an oxygen partial pressure of $0.32\,\mathrm{mbar}$. After deposition the sample was annealed for $12\,\mathrm{h}$ at $485\,^\circ\mathrm{C}$ in an oxygen atmosphere to ensure full oxygenation of the YBCO layers [25].
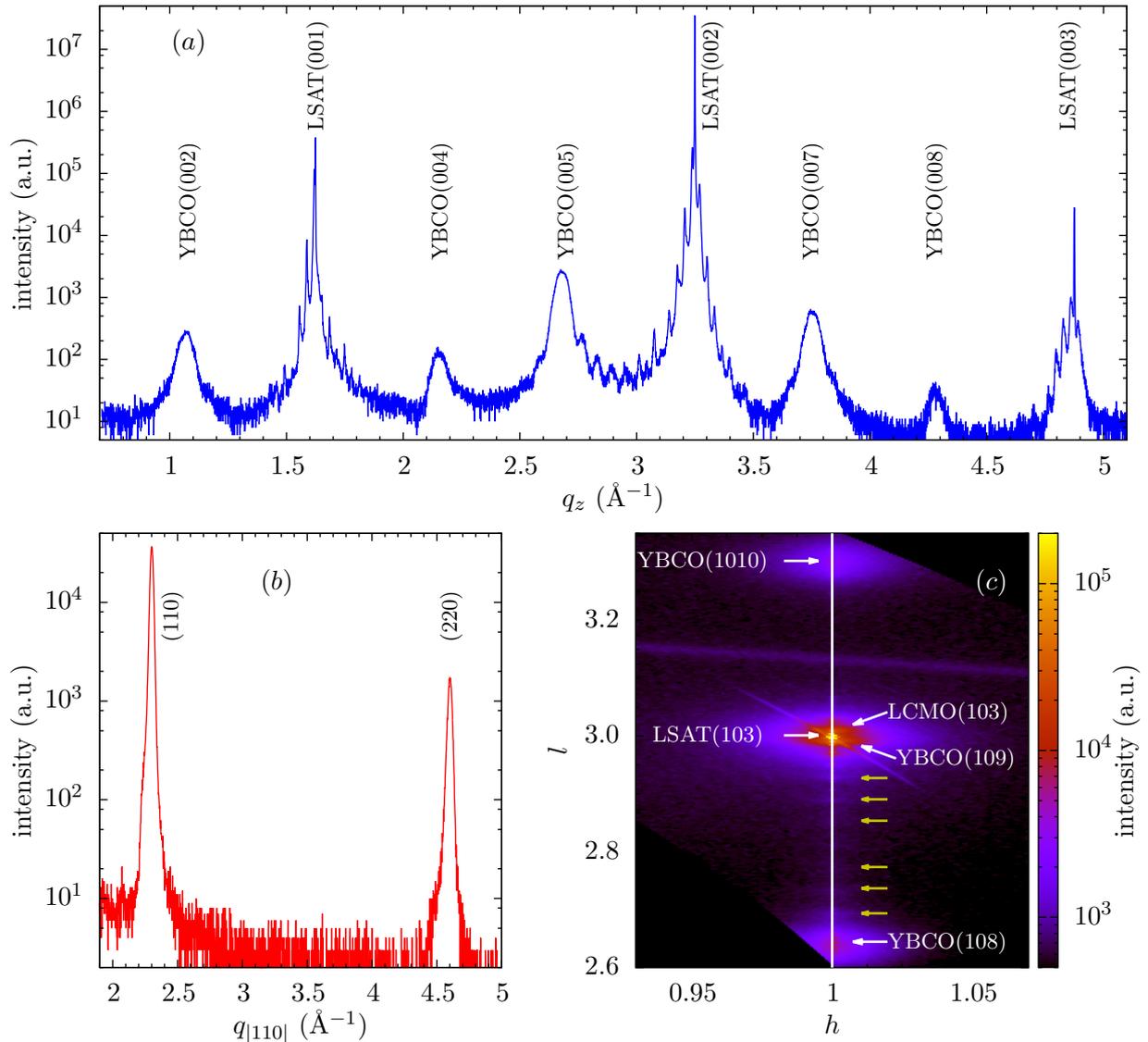
Figure 3.1: X-Ray diffraction data of the sample YLCM. (a) Standard x-ray diffraction with the momentum transfer along the z direction (perpendicular to the surface). (b) In plane diffraction pattern along the (110) direction. (c) Reciprocal space map around the LSAT(103) peak, the yellow arrows mark the position of the superlattice modulations of the diffracted intensity. A pseudo-cubic structure for LSAT and LCMO has been used for the assignment of the peaks.

It is worth mentioning that the LSAT substrate has been chosen because it is well lattice matched to both YBCO and LCMO. It also allows one to avoid the complications which develop below the structural transition at $105\,\mathrm{K}$ in the more commonly used $SrTiO_3$ (STO) substrates. As already discussed in section 2.1.3, this transition may give rise to a buckling of the interface that strongly reduces the intensity of the specular reflection for both neutron and x-ray reflectivity measurements and thus limits the information that these techniques can provide about the structural and magnetic depth-profiles of the superlattice.

To determine the structural properties of the sample a detailed x-ray diffraction study has been performed. The x-ray diffraction measurements were carried out using a Rigaku SmartLab triple-axis diffractometer with a $9\,\mathrm{kW}$ Cu-$K\alpha$ radiation source. The results are summarized in Figure 3.1. Panel (a) shows the standard x-ray diffraction pattern where the momentum transfer is perpendicular to the sample surface. Only peaks along the crystallographic c axis are identified confirming that the multilayer is epitaxial with the c axis perpendicular to the surface. For YBCO this means that the conducting CuO_2 layers, where superconductivity occurs, are parallel to the surface. No trace of other phases or impurities

has been observed. The high intensity peaks also exhibit a series of side peaks, the so-called superlattice peaks, that are due to the interference of the multiple reflections of the x-rays at the different interfaces. The high intensity of these modulations testifies to the high quality of the interfaces in the superlattice. The c lattice parameters as extracted from the position of the peaks amount to $c_{YBCO} = 11.71(2)$ Å and $c_{LSAT} = 3.8660(4)$ Å. The measured c lattice parameter for YBCO is slightly larger than the reported bulk value $c_{YBCO}^{bulk} = 11.6757(4)$ Å [49]. This difference arises from the strain that is induced by the substrate and gives rise to a slight compression of the in-plane lattice parameters. Due to the resemblance between the LCMO and LSAT perovskite structures, with a lattice mismatch of less than 0.1%, the LCMO peaks in the diffraction pattern overlap with the much stronger LSAT ones. For this reason the lattice parameter for LCMO cannot be accurately determined.

Panel (b) in Figure 3.1 shows the result of the in-plane diffraction measurement along the (110) axis. To perform this experiment the incident angle of the beam is set below the total reflection critical angle ($\omega_c \approx 0.3\,°$) to induce a superficial evanescent wave. Under proper geometric conditions this wave is diffracted by the crystallographic planes perpendicular to the surface and are correspondingly reflected according to Bragg's law. The scattering plane is thus the surface plane and the measurement allows the direct determination of the in plane lattice parameters. Two peaks have been observed corresponding to the (110) and (220) reflections of the LSAT pseudo-cubic structure. From these peaks the in-plane lattice parameter can be calculated as $a = 3.867(5)$ Å. It is virtually identical to the lattice parameter of cubic LSAT substrate.

Within the resolution of the in-plane diffraction experiment it is not possible to observe any additional peaks that could be attributed to the superlattice, this suggests that both the YBCO and LCMO structures exhibit a tetragonal phase and adopt the substrate in-plane lattice parameters. A nearly full strained epitaxial growth of the superlattice is confirmed by the high resolution reciprocal space map around the pseudo-cubic LSAT(103) peak, shown in panel (c) of Figure 3.1. Both the LCMO and YBCO peaks in the map are symmetric around and peaked at the $h = 1$ line. The in-plane lattice parameter is therefore the same for the substrate and the superlattice. There is no evidence of a lattice relaxation as would be suggested by a pronounced asymmetry of the peaks. The calculated in-plane lattice parameter corresponds to an average difference of 0.3 % and 0.06 % with respect to the bulk in-plane lattice parameters for YBCO and LCMO, respectively [49, 100]. Accordingly, the YBCO unit cell volume can be calculated as $V_{YBCO} = 175.1(3)$ Å^3 which differs from the bulk value by only 1 %. An even smaller change in the unit cell volume is expected for LCMO given the better lattice matching with LSAT. As marked with yellow arrows in Figure 3.1(c), the superlattice modulations of the intensity along the l direction (perpendicular to the surface) are also visible on the map.

3.2.   Electric and magnetic properties

The electric and magnetic properties of the sample have been determined with electric transport and dc magnetization measurements. The resistance measurements were performed using the four-point probe option of a physical properties measurement system (PPMS) from Quantum Design (model QD6000). The magnetization was measured on a small piece cut from the corner of the sample using the vibrating sample magnetometer (model P525) option of the PPMS system.

As depicted in Figure 3.2(a), both the superconducting and ferromagnetic properties of the YBCO and LCMO layers are retained. The resistance shows a sharp decrease at the onset of the superconducting transition at $T_C \approx 88\,K$ and vanishes below 72 K. The superconducting onset temperature is only about 5 K lower than the bulk value [47]. This indicates that the YBCO layers are close to optimal doping and that the superconducting properties are not strongly affected by strain effects induced by the substrate. As previously reported, the fairly broad superconducting transition may arise from the proximity coupling with the
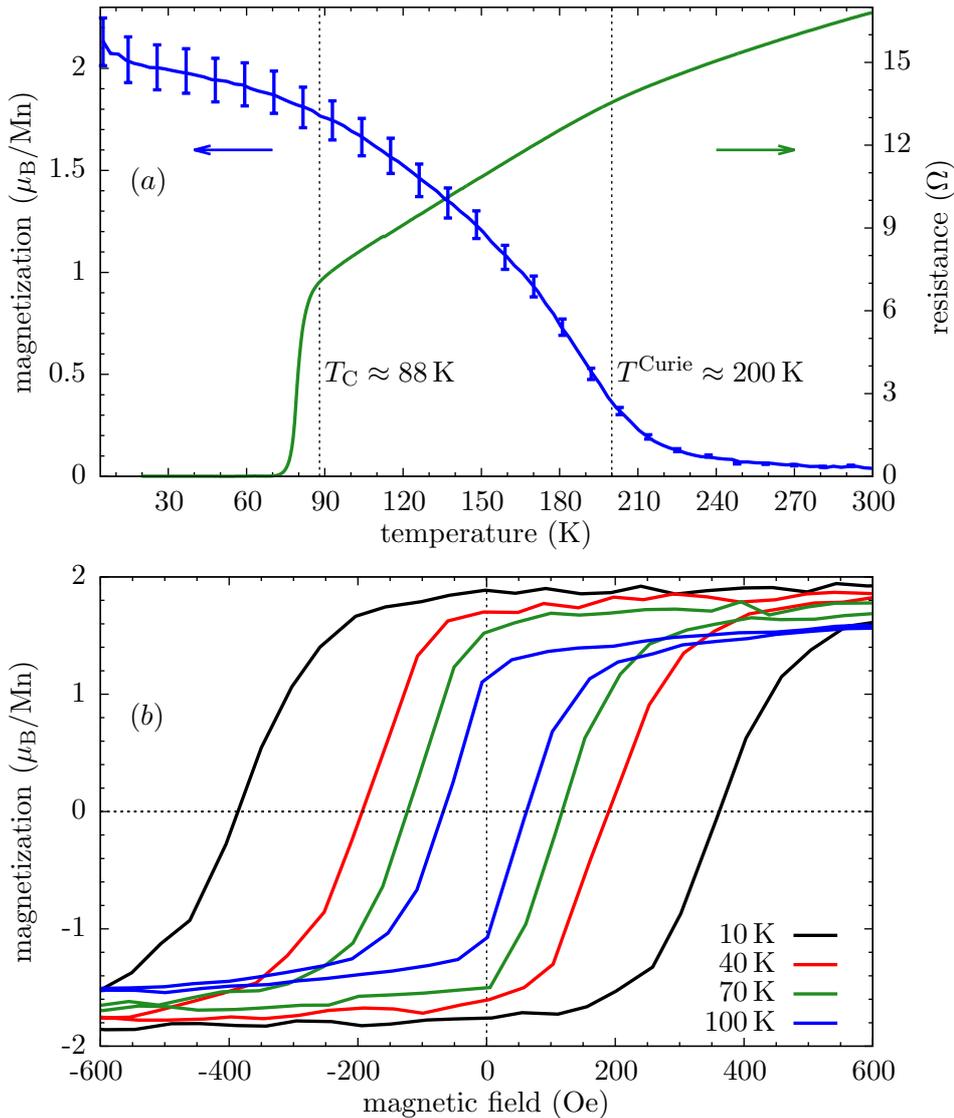
Figure 3.2: (a) Temperature dependence of the resistance and the magnetization in field-cooled (FC) mode with $H = 4\,\text{kOe}$ applied parallel to the layers of the YBCO/LCMO superlattice YLCM showing the onset of the superconducting transition at $T_C \approx 88\,\text{K}$ and the ferromagnetic transition at $T^{\text{Curie}} \approx 200\,\text{K}$. The 5 % error margin in the magnetization data represents the uncertainty in the sample volume and in the thickness and density of the LCMO layers. (b) Magnetic hysteresis loops measured at different temperatures.

ferromagnetic LCMO layers [22].

The field cooled (FC) magnetization curve was measured with a 4 kOe field applied parallel to the sample surface. The average Mn magnetization has been calculated using an area of $1.12(6)\,\text{mm}^2$, a thickness of the LCMO layers of $93.6(1.2)\,\text{nm}$, and the bulk density of the Mn ions of $17.37\,\text{nm}^{-3}$. The latter assumption is justified by the small lattice distortions of the LCMO unit cell and by the fact that the fitted value of the LCMO density from the PNR measurements matches the bulk one, as outlined in the next section. It should be noted that this is an average value since not all the Mn ions may contribute in the same way to the magnetization. The ferromagnetic transition at $T^{\text{Curie}} \approx 200\,\text{K}$ is evident from the sudden increase in the field cooled magnetic moment as well as from a kink in the temperature dependence of the normal state resistance. The latter feature originates from the insulator-to-metal transition in the LCMO layer which coincides with the ferromagnetic ordering.

The magnetization loops for different temperatures show typical ferromagnetic hysteresis curves as shown in Figure 3.2(b). Both the saturation magnetization and coercive field increase

toward low temperatures. At 10 K the saturation magnetization reaches about $1.9\,\mu_B/$Mn and the saturation field is around 1 kOe. This average magnetization value is significantly smaller than the reported one for bulk samples of about $3.5\,\mu_B/$Mn [101, 102]. In addition, a significant broadening of the hysteresis curve is observed at low temperatures. The coercive field increases from 65 Oe at 100 K to 375 Oe at 10 K. This effect has been observed previously in manganites with a reduced magnetization and was attributed to an inhomogeneous magnetic phase [103]. The interaction of ferromagnetic clusters embedded in a paramagnetic matrix leads to a spin-glass state for which the coercive field shows an anomalous increase at low temperatures. A similar coercivity enhancement at low temperatures has also been reported in manganite antiferromagnetic/ferromagnetic heterostructures, in this case the competition between the ferromagnetic and antiferromagnetic interactions at the interfaces leads to frustration and spin freezing [104, 105]. The reduced magnetization and the enhancement of the coercivity at low temperatures thus suggest the presence of magnetic inhomogeneities in the LCMO layers which could correspond to paramagnetic, canted ferromagnetic or even antiferromagnetic phases.

3.3. Polarized Neutron Reflectometry measurements

This section describes the polarized neutron reflectometry (PNR) measurements which have been performed on the YLCM superlattice. It shows how this technique can be used to obtain the structural and the magnetic depth profiles. Specifically, it details the changes to the magnetization of the Mn ions in the vicinity of the interfaces.

3.3.1. Determination of the structural parameters and the chemical depth profile

In a first step, the structural parameters of the superlattice have been obtained by analyzing the room temperature neutron reflectometry curves for which the potential is governed by the nuclear scattering length density (since the ferromagnetic order occurs only below $T^{Curie} \approx 200\,K$). Figure 3.3 shows the unpolarized neutron reflectometry measured on the YLCM sample at room temperature with the NREX and SuperADAM reflectometers of the Forschungs-Neutronenquelle Heinz Maier-Leibnitz (FRM II) in Munich (Germany) and the Institut Laue-Langevin (ILL) in Grenoble (France), respectively. The slight differences between the two curves are due to the different experimental configurations, for SuperADAM a high resolution setup was used whereas for NREX the signal-to-noise ratio was enhanced at the expense of a lower resolution. Both curves exhibit a sharp reflection edge and a set of well-defined superlattice Bragg peaks (SLBPs). The latter originate from the constructive interference between the neutron waves that are reflected from all the interfaces of the super-lattice. The position, width and intensity of the SLBPs contain the information about the average value and the variation of the thickness of the individual YBCO and LCMO layers. Additional information about the roughness of the superlattice is contained in the form of the overall decrease toward large momentum transfer of the reflectivity curve beyond the reflection edge. In the absence of roughness this decrease follows a q_z^{-4} law, where q_z is the value of the momentum transfer normal to the sample surface. The roughness enhances this overall decrease of the intensity of the reflectivity curve.

The high resolution data from SuperADAM shows in addition a fast oscillation in the q_z range between the reflection edge and the 1st SLBP. These are the so-called Kiessig fringes that originate from the interference between the reflections from the surface (ambient/LCMO) and the bottom (interface with the LSAT substrate) of the superlattice. These features testify to the high quality of the YLCM sample. From their periodicity one can deduce the total thickness of the film. The thickness of the YBCO/LCMO bilayers can be inferred from the position of the SLBPs. The information about the thickness ratio of the YBCO and LCMO layers is contained in the intensity variation of the even and odd order peaks. For example, the even order Bragg peaks are entirely suppressed if the YBCO and LCMO layers have exactly the same thickness. This is a destructive interference phenomenon that originates
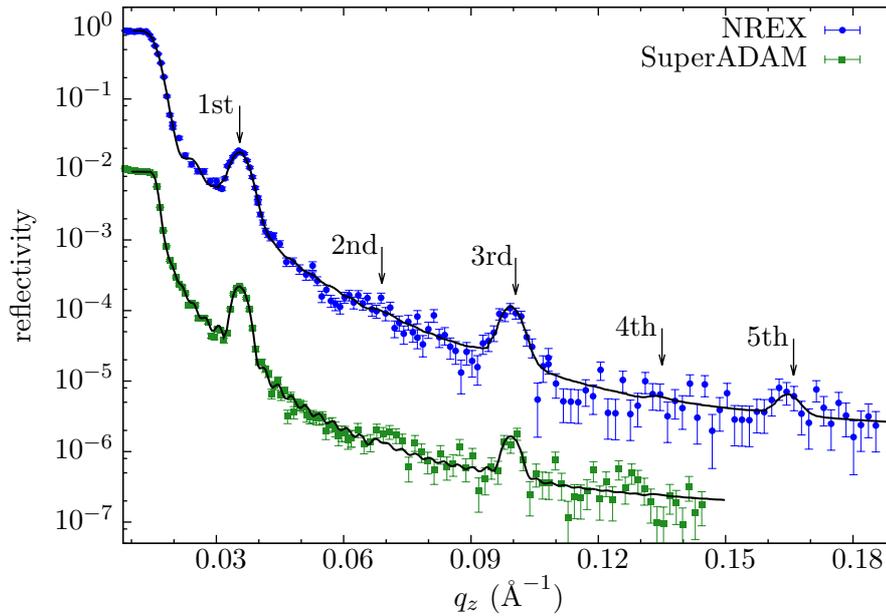
Figure 3.3: Unpolarized neutron reflectivity curves of the YLCM superlattice measured at room temperature with the NREX and SuperADAM instruments. The curves are vertically shifted for clarity. Symbols show the experimental data band solid lines the best fits that were obtained by fitting both curves simultaneously. The arrows mark the positions of the SLBPs.

from the π-phase shift between the neutron waves that are reflected at the YBCO/LCMO and the LCMO/YBCO interfaces. It arises because the scattering potential exhibits a step-like increase at one of the interfaces and a corresponding decrease on the other one. In the reflectivity curves in Figure 3.3 the intensity of the 2nd and 4th order SLBPs is indeed much weaker than the one of the 1st and 3rd order SLBPs. The finding that the suppression of the even order SLBP intensity is not complete, i.e. that a small increase is observed at the position of the 2nd and the 4th order SLBPs, shows that there is a small mismatch between the thickness of the YBCO and LCMO layers.

The two room temperature unpolarized neutron reflectometry curves have been simultaneously fitted using a simple model where the YBCO/LCMO bilayer structure is repeated ten times, the calculation was performed using the GenX software [74]. No special assumptions were made as for the density or thickness, neither in the very first YBCO nor in the very last LCMO layers. Only the roughness of the latter has been treated independently to account separately for the surface and interface roughness. The result of the best fit is shown by the solid lines in Figure 3.3 and can be seen to describe the experimental data (symbols) very well. The obtained values for the nuclear scattering length density, thickness and roughness are summarized in Table 3.1. The calculated scattering length density for the YBCO and LCMO layer agrees well with previously reported results on similar samples [25] and correspond to a percentage reduction of 3(1) % and 0.5(8) %, respectively, with respect to the bulk values. For YBCO the difference is larger than the calculated change in the unit cell volume (1 %), this might be due to some ion vacancies created during the growth process. For LCMO the difference is within the error bars confirming that the density and stoichiometry of the layers are not significantly modified with respect to the bulk values. The YBCO layers are found to be slightly thicker than the LCMO ones, the calculated thicknesses correspond to approximately 8 and 24 unit cells per YBCO and LCMO layer, respectively. The high quality of the interfaces is evidenced from the small calculated value of the roughness which is always smaller than the c-axis parameter of the YBCO unit cell. In terms of the growth direction, the LCMO/YBCO interface is slightly rougher than the YBCO/LCMO one. The film surface roughness of 10(1) Å is very small and corresponds to only 0.5 % of the total film thickness.

	ρ_{n} ($10^{-6}\,\text{Å}^{-2}$)	d (Å)	σ (Å)
YBCO	4.53(5)	97.6(1.2)	7.0(1.1)
LCMO	3.58(3)	93.6(1.2)	9.3(1.1)
LSAT	5.117	–	–

Table 3.1: Nuclear scattering length density (ρ_{n}), thickness (d) and roughness (σ) of the YBCO and LCMO layers in the YLCM superlattice as obtained from the fit of the room temperature neutron reflectometry. The given roughness corresponds to the top interface of the layer in the growth direction. Also shown for reference is the substrate scattering length density that was not used as a fitted parameter but was calculated from the structural parameters reported in Ref. [106].

3.3.2. Low temperature measurements and the magnetic depth profile

Figures 3.4 and 3.5 show the low temperature PNR curves which have been measured on the YLCM sample after field-cooling in magnetic fields of 100 Oe and 4 kOe with SuperADAM and NREX, respectively. The magnetization loops in Fig 3.2 show that at 4 kOe the sample is already fully magnetized. At 100 Oe the sample is not fully saturated, the field-cooled magnetization data in Figure 3.9 show that the magnetization reaches about 80 % of the saturation value here. In fitting these PNR curves the structural parameters as obtained from the room temperature curves have been used as a constraint that can vary only within the error bar. This seems well justified, since the expected changes due to the temperature dependence of the lattice parameters of YBCO and LCMO are well within these error bars [25]. In addition, Figure 3.6 shows the off-specular scattering at 300 K and 4 K which confirms that the anomalous broadening and splitting of the specular reflection curves that was previously reported for similar superlattices on STO substrates at temperatures below 100 K [29, 63, 107] is absent for the present YBCO/LCMO superlattice on LSAT. The comparison of the maps in Figs. 3.6(a) and 3.6(b) shows that for the reflection edge and the SLBPs the width in the off-specular direction is small and does not change significantly between 300 and 4 K. The quality of the specular reflectivity curves at low temperature accordingly remains very high. As shown in Figs. 3.4 and 3.5, the intensity of the reflectivity curves does not fall off significantly faster at 10 K or 4 K than at 300 K and the signal remains well above the background level for the q_z values up to $0.14\,\text{Å}^{-1}$ which includes the 4th order SLBP.

The shape of the reflectivity curves below $T^{\mathrm{Curie}} \approx 200\,\text{K}$, as shown in Figs 3.4 and 3.5, depends on whether the incident neutron spin is parallel ($|+\rangle$) or antiparallel ($|-\rangle$) to the applied magnetic field. This is due to the additional magnetic potential which is comparable in magnitude to the nuclear one and for which the sign depends on the orientation of the ferromagnetic moments with respect to the neutron spins. It is also evident that the 2nd and the 4th order SLBPs, which were almost absent in the curves at 300 K, have gained a significant intensity and became very pronounced features in the PNR curves at 100 K, 10 K and 4 K. As was proposed in Ref. [30], this is a clear indication that the magnetic potential has a lower local symmetry than the nuclear one. For the latter the even order SLBPs were almost absent due to the similar thickness of the YBCO and LCMO layers. The magnetic potential due to the ferromagnetic order, does obviously not exhibit a step-like increase right at the YBCO/LCMO interface or a corresponding decrease at the LCMO/YBCO interfaces. Instead, there must be either a significant decrease of the ferromagnetic moment on the LCMO side of the interface or a corresponding increase on the YBCO side.

Due to the lack of the phase information in the reflectometry measurement, the shape of the depth profile of the magnetic potential cannot be directly extracted from the PNR data. The reflectivity curves can still be analyzed with different realistic models and their validity can be judged based on how well they reproduce the data [108]. As was the case in Ref. [30], it may still happen that different models lead to similar results and therefore cannot be distinguished. Nevertheless, this ambiguity may be overcome with reflectivity curves that extend up to larger q_z values where the differences between the various models become more
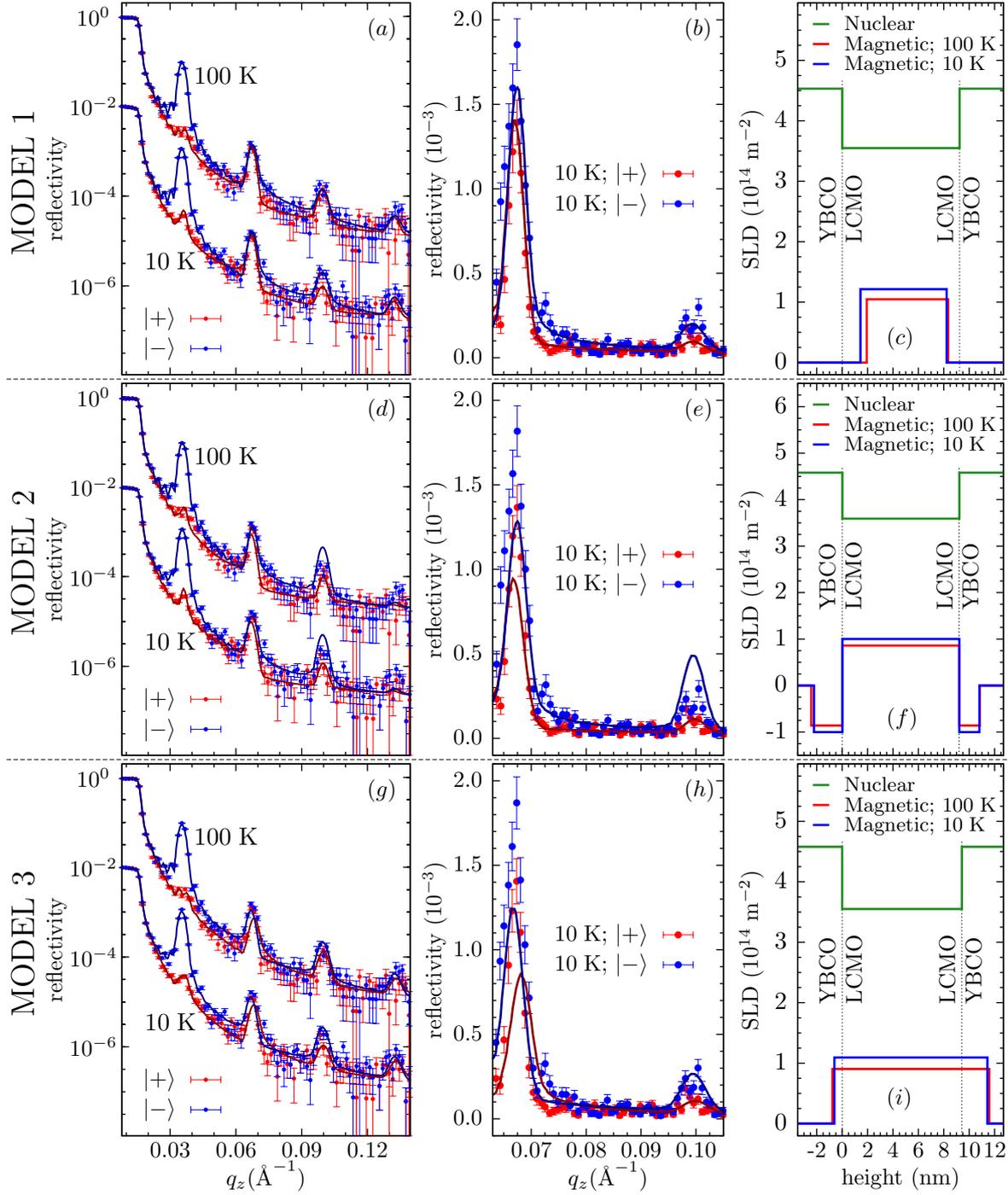
Figure 3.4: Left: (a) Polarized neutron reflectivity curves of the YLCM superlattice measured at low temperature after field-cooling in 100 Oe at SuperADAM for up $|+\rangle$ and down $|-\rangle$ polarization of the neutron spin with respect to the direction of the applied magnetic field. The lines show the best fit for the depleted layer model for $|+\rangle$ (red) and $|-\rangle$ (blue) neutron spin channels. For clarity the curves at 10 K are vertically shifted down by a factor of 10^2. (b) Close-up on a linear intensity scale in the region of the 2nd and 3rd SLBP to aid the comparison with the fit. The depth profiles of the used nuclear and magnetic scattering length densities are shown in (c). The same data are shown in (d)-(f) together with the best fit using the model of an inverse magnetic proximity effect and, in (g)-(i), for the model of an induced ferromagnetic moment in YBCO that is parallel to the one in LCMO.
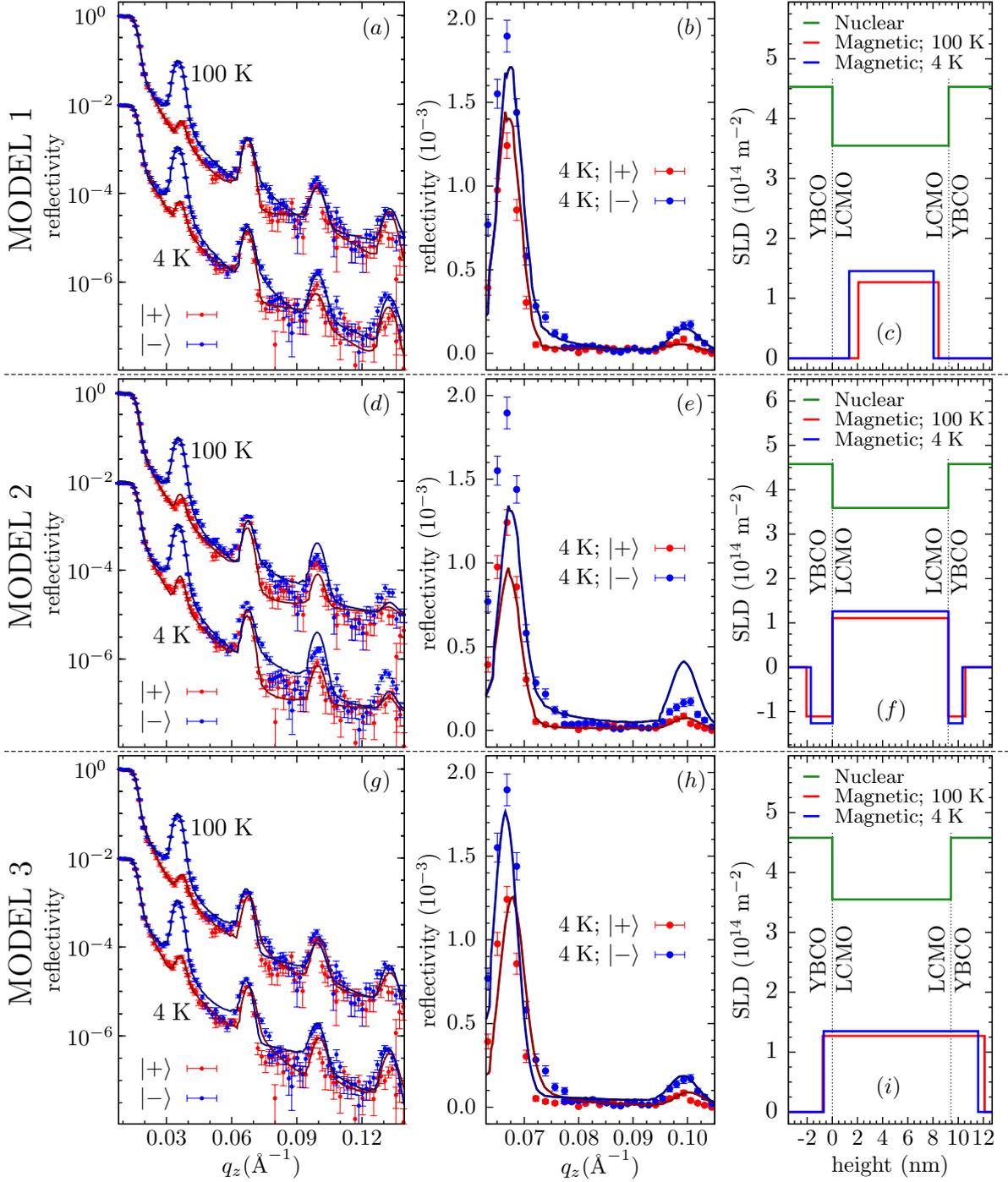
Figure 3.5: Same as in Figure 3.4 but for the PNR data measured at NREX with an applied field of 4 kOe.

pronounced as discussed in the following.

Three different models have been proposed to reproduce the polarized neutron reflectivity data, their suitability has been evaluated in terms of the quality of the best fit. Model 1 corresponds to the depleted layer model, a strong suppression of the ferromagnetic moment at the interface is modeled by introducing a non-magnetic layer on the LCMO side of each interface. The thickness of this layer is a fitting parameter.

Model 2 describes the inverse magnetic proximity effect, where ferromagnetic moments antiparallel to the Mn moments in LCMO are induced on the YBCO side of the interface. In the first place, one expects that these are the Cu moments which have been observed with the x-ray magnetic circular dichroism (XMCD) measurements [34, 109]. However, as will be
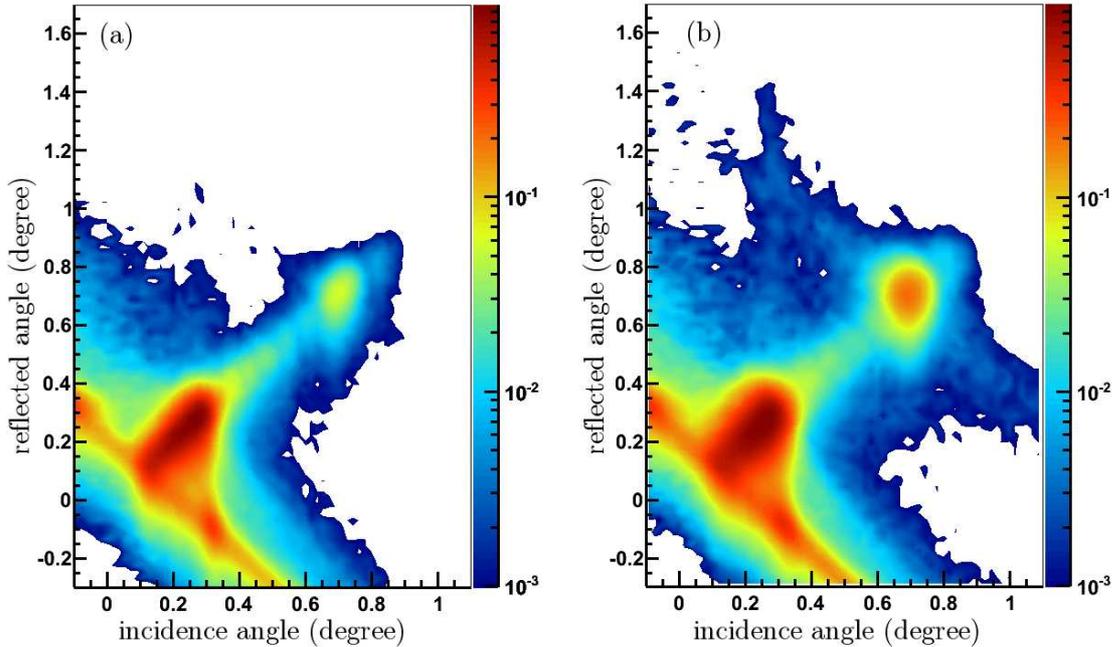
Figure 3.6: Maps of the off-specular reflection of the YBCO/LCMO superlattice measured (*a*) with unpolarized neutrons at 300 K and (*b*) for the $|+\rangle$ spin channel at 4 K after field-cooling in a field of 100 Oe.

described in section 3.5, the magnitude of these ferromagnetic Cu moments is only $\sim 0.18\,\mu_{\mathrm{B}}$. Therefore, it remains to be seen whether they can account for the observed large increase of the intensity of the even order Bragg peaks. On the other hand, the possibility that an additional, possibly even larger contribution arising from some Mn ions that may have been incorporated in the YBCO layers, for example due to an unwanted contamination or a diffusion across the interface during the growth, cannot be excluded.

Model 3 accounts for a similar case where the induced ferromagnetic moment on the YBCO side is parallel to the one of the Mn moments in LCMO and to the applied magnetic field. Such a contribution would have to arise solely from the Mn moments, since the XMCD data clearly established the antiparallel orientation of the Cu moments.

Figures 3.4 and 3.5 show the PNR curves at 100 K, 10 K and 4 K with the best fits for each model (solid lines) together with the obtained depth profiles of the nuclear and magnetic scattering length densities. As was already mentioned, the structural parameters have been constrained to lie within the error bars of the parameters derived from the unpolarized room temperature curves. For all three models a modified magnetic potential for the topmost LCMO layers has been used: the core magnetization has been fitted independently and a 2-3 nm thick non-magnetic layer has been introduced at the film surface. In all cases the calculated core magnetization in the topmost LCMO layer is smaller than the magnetization in the inner layers of the superlattice. This modification was necessary to reproduce the sizable differences between the $|+\rangle$ and $|-\rangle$ curves in the region right before and after the 1st order SLBP. This effect may arise from the interaction of the surface layer with the ambient which degrades the ferromagnetic order in the first few LCMO monolayers. The obtained reduced likelihood estimators for models 1, 2 and 3 of $l_1^{red} = 3.36$, $l_2^{red} = 5.65$ and $l_3^{red} = 6.40$, respectively, are in favor of model 1. The specific features where models 2 and 3 fail to describe the experimental data are discussed next.

The close-up in Figs. 3.4(*h*) and 3.5(*h*) reveals that model 3 predicts a shift in the position of the 2nd order SLBP towards lower (higher) q_z for the $|-\rangle$ ($|+\rangle$) curve. Such a shift is not observed in the experimental data where the maxima nearly coincide and the splitting of the curves is due to the different intensities of the peaks. The disagreement is especially obvious on the high q_z side of the 2nd order Bragg peak where the intensity of the fitted $|+\rangle$

T, H	$d_{\text{dep}}^{\text{bottom}}$ (Å)	$d_{\text{dep}}^{\text{top}}$ (Å)
10 K, 100 Oe	14.4(7)	10.1(7)
100 K, 100 Oe	19.4(7)	8.9(7)
4 K, 4 kOe	13.4(7)	12.0(7)
100 K, 4 kOe	20.7(7)	9.7(7)

Table 3.2: Thickness of the depleted layers at the bottom and top interfaces as obtained with model 1 at different temperatures and applied magnetic fields.

curve is higher than for the corresponding $|-\rangle$ curve, whereas in the experimental data the opposite trend is observed. Such a discrepancy was already noted in Ref. [30] and was used to discard model 3. Furthermore, a rather large value of the induced magnetization in the YBCO layers has to be assumed for model 3 to account for the large intensity of the 2nd order SLBP. For the fits in Figs 3.4 and 3.5 the ferromagnetic moment in the YBCO layer has been constrained to have the same value as the one in the LCMO layers. When it was released, the induced magnetization reached even larger values whereas the quality of the fit was not significantly improved. Already the constrained value appears to be unreasonably large, e.g. for the PNR curves taken at 4 kOe it reaches $\sim 2.9\,\mu_{\text{B}}$. Such a large ferromagnetic moment on the YBCO side of the interface cannot arise from the induced Cu moments, it would also require an unrealistically large concentration of Mn ions diffusing into the YBCO layers.

Model 2, as shown in the close-ups in Figs 3.4(e) and 3.5(e), can account reasonably well for the data in the vicinity of the 2nd order SLBP. Nevertheless, it largely overestimates the intensity of the 3rd order peak in the $|-\rangle$ curve. The intensity of this peak in the simulation could be reduced assuming an increased roughness of the magnetic potential. However, this would lead to a faster decay of the curve to the background level which is not observed. It would also further enhance the discrepancy at the 4th order SLBP where the fit already severely underestimates the peak intensity of the $|-\rangle$ curve. Furthermore, model 2 has the same problem as model 3 concerning the very large value of the induced moment in the YBCO layers that has to be assumed. Once more, for the fit in Figs 3.4(d) and 3.5(d) the ferromagnetic moment in the YBCO layer has been constrained to be the same as the one in the LCMO layers, i.e. at 4 kOe it reaches $\sim 2.7\,\mu_{\text{B}}$. This value is larger than the moment of $\sim 1\,\mu_{\text{B}}$ of Cu^{+2} and one order of magnitude larger than the value calculated from the XMCD measurements performed on the same sample, $\sim 0.18\,\mu_{\text{B}}$ (see section 3.5). If the induced magnetic moment is bound to, for example, $1\,\mu_{\text{B}}$ the intensity of the 2nd SLBP is largely reduced and the overall quality of the fit is strongly degraded.

Model 1 is clearly the one that reproduces the measured data the best. The position, spin splitting, and intensity of all SLBPs are reasonably well described. Only the overestimation of the intensity of the 4th order SLBP in the $|+\rangle$ curve at NREX can be regarded as a significant mismatch between the simulation and the data. The very fact that such a simple block-like model reproduces all features of the measurement is remarkable and confirms that it contains the main characteristics of the magnetic depth profile of the superlattice. These simulations clearly establish the trend that a sizable suppression of the ferromagnetic moment on the LCMO side of the interface is responsible for the occurrence of the even order SLBPs. The characteristic length of the decay of the ferromagnetic moment at the interface should therefore be directly related to the calculated thickness of the depleted layers which are shown in Table 3.2 for the different temperatures and fields. At 4 K and under an applied field of 4 kG the magnetization in the core of the layers is calculated as $3.1\,\mu_{\text{B}}/\text{Mn}$, which is closer to the bulk values. The net reduction in the averaged magnetization observed in the FC magnetization measurements is therefore explained by the depleted layers at the interface.

For the bottom interface the depleted layer thickness is as large as 20.7 Å showing that the suppression of the magnetization extends rather far into the LCMO layers. The similar values of the thickness of the depleted layer (within the error bars) at 100 Oe and 4 kOe show that the depleted layer is hardly affected by the external magnetic field. This excludes for example an
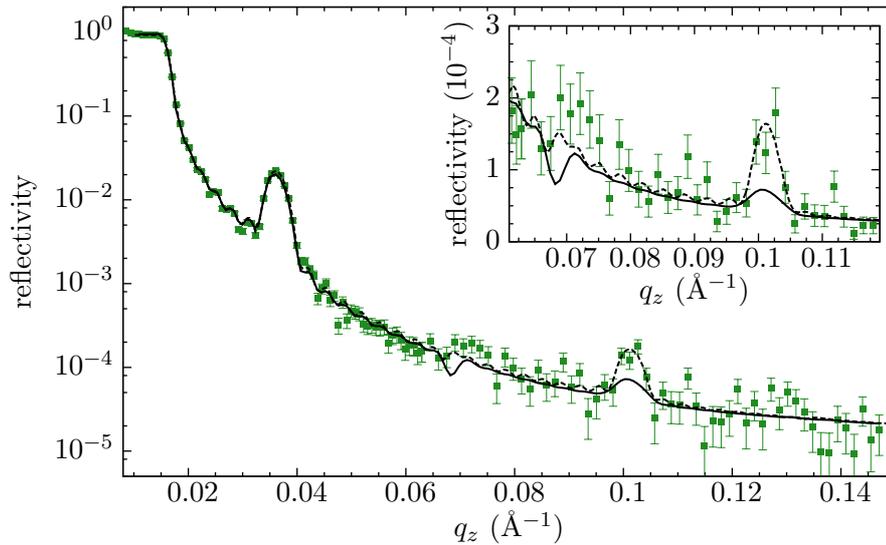
Figure 3.7: Room temperature reflectivity curves (symbols) of the YLCM superlattice measured with neutrons. The dashed lines show the best fit with a roughness of 7.0 Å and 9.3 Å at the LCMO bottom and top interfaces, respectively, that was also shown in Figure 3.3. The solid lines show a simulation in which a roughness of 17 Å and 10.2 Å was assumed for the LCMO bottom and top interfaces, respectively. Inset: Magnification around the high order SLBPs to highlight the difference between the two models.

explanation in terms of a different ferromagnetic phase that has a larger saturation field than the one in the center of the LCMO layers. It also appears that the thickness of the depleted layer is consistently larger for the bottom interface than for the one on top of the LCMO layer (in terms of the superlattice growth direction). Moreover, the average magnetization of the top LCMO interface is systematically larger for all models. The origin of this difference is not known. It may be related to a structural difference that is imposed by a different growth process. However, as already discussed, concerning the roughness such a significant difference between the top and bottom interfaces has not been found. Furthermore, a recent transmission electron microscopy (TEM) study on superlattices that were grown under identical conditions did not provide any indication for such a difference [25]. Surprisingly, but in good agreement with a previous study of similar superlattices on STO substrates [110], the TEM images reveal that both the YBCO/LCMO and the LCMO/YBCO interfaces involve the same kind of CuO_2-Y-CuO_2-BaO-MnO_2 layer stacking sequence for which the last YBCO unit cell is lacking the CuO chains. The expected asymmetry of the interfaces, where a CuO chain layer should be adjacent to one of the interfaces and a CuO_2 bilayer to the other one, could not be observed. This still leaves the possibility that the layer separating the CuO_2 and MnO_2 planes may have a different stoichiometry, i.e. it may have a variable Ba and La or Ca content.

The results of model 1 show that to model the temperature evolution of the PNR curves a mere modulation of the magnetization in the core of the LCMO layers is not enough, changes in the magnetic properties of the depleted layers should be introduced as well. Notably, at the lowest temperature of 4 K and 10 K, the thickness of the bottom (top) depleted layers is reduced (increased) with respect to the values at 100 K. These changes lead to a sizable reduction of the asymmetry between the two interfaces and, as will be discussed in section 3.3.3, are triggered below 90 K.

It should be emphasized that the depleted layers cannot be simply interpreted in terms of a roughness induced effect. The thickness of the depleted layer at the bottom interface (up to 20.7 Å) is much larger than the corresponding interface roughness ($\sim$7 Å). Furthermore, while the thickness of the depleted layer at the bottom interface is larger than at the top one, the interface roughness exhibits an opposite trend and is larger in the latter. This suggests that there is no correlation between these two quantities. Figure 3.7 shows that the PNR data
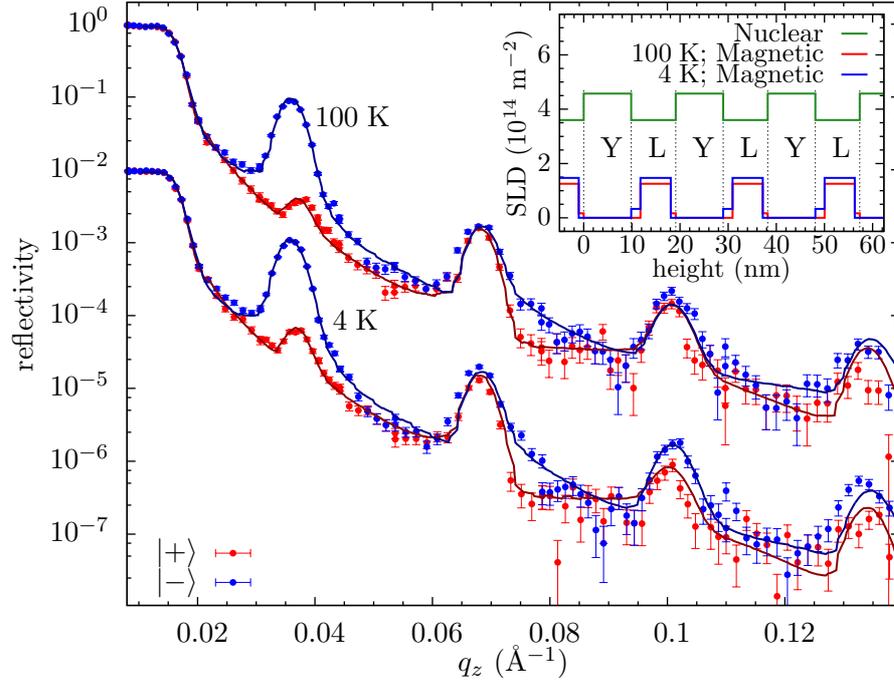
Figure 3.8: Low temperature PNR curves of the YLCM superlattice at 4 kOe. The solid lines are the results of the fit using Model 1a, here the magnetization in the depleted layers is fitted and the thickness of the top and bottom interfaces are set as common among all datasets.

are not in agreement with a model for which the interface roughness is assumed to match the average thickness of the depleted layers of 17 Å and 10.2 Å for the bottom and top LCMO interfaces, respectively. There is a clear trend that such an enhanced interface roughness would lead to a stronger suppression of the intensity of the higher order SLBPs than is observed in the experiment. It would also yield the wrong size and shape of the symmetry forbidden 2nd order SLBP. Besides, such a structural roughness could also not explain the observation that the thickness of the depleted layer exhibits a significant temperature dependence as discussed in section 3.3.3.

To obtain further information about the magnetic nature of the depleted layers, model 1 has been modified to allow for a finite magnitude of the ferromagnetic moments in the depleted layer (treating the net magnetization in the depleted layers as a fitting parameter). To keep the number of fitting parameters reasonably low and to make the comparison of the results for different temperatures and fields easier, the thickness of the depleted layers for the top and bottom interfaces have now been set to be common for all datasets. This modification is labeled as model 1a and the comparison of the fitted curves using this model and the PNR data at 4 kOe data is shown in Figure 3.8. The inset shows the obtained depth profile of the scattering length densities, for which the magnetic part is proportional to the ferromagnetic moment. In agreement with the results obtained for model 1, shown in Table 3.2, the thicknesses of the top and bottom depleted layers are calculated as 10.4(7) Å and 19.2(7) Å, respectively. It appears that the best fit obtained with model 1a is indeed very similar to the one of model 1 (see Figure 3.5) and results in a similar value of the reduced likelihood estimator of $l_{1a}^{red} = 3.50$. It is noteworthy that the magnetic properties of the interfaces show the temperature variation of model 1. As shown in Figure 3.8, between 100 K and 4 K the magnetic moment at the bottom interface is augmented while the one at the top interface is reduced. This behavior was already observed in model 1 where the thickness of the bottom interface is smaller at 4 K than at 100 K and the top interface showed the opposite trend. The fact that a good fit is obtained with a small magnetization in the depleted layers suggests that although the strong suppression of the net magnetization appears evident, it is not possible to rule out the presence of a small ferromagnetic moment in the depleted layers.
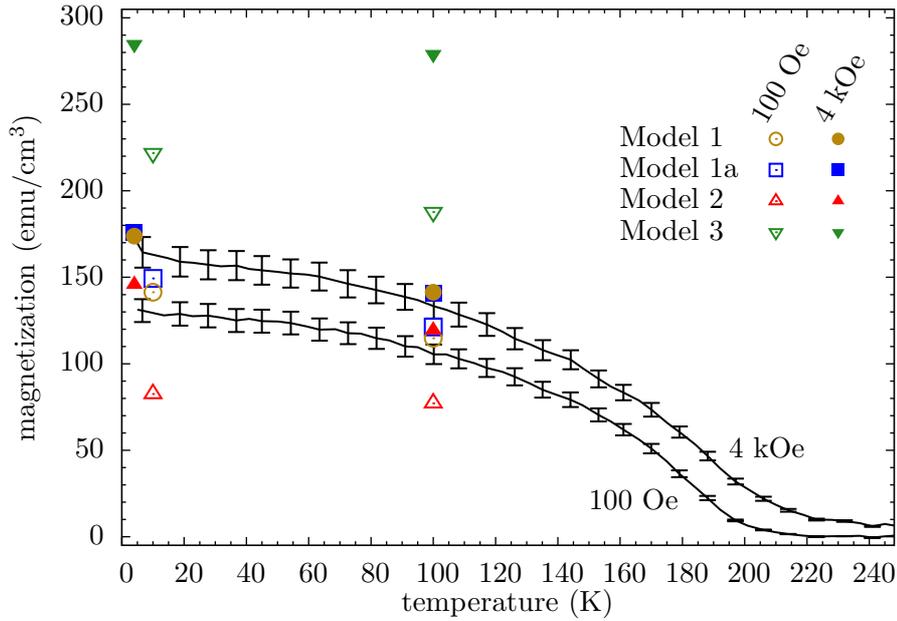
Figure 3.9: Comparison of the average magnetic moment as determined experimentally from field-cooled dc magnetization measurements at 100 Oe and 4 kOe (solid lines) and calculated from the magnetic potential obtained with model 1 (circles), model 1a (squares), model 2 (upwards triangles) and model 3 (downwards triangles) from the fits to the PNR curves measured at 100 Oe (open symbols) and 4 kOe (solid symbols). The size of the symbols of the calculated magnetic moments reflects the error bars. The error bars of the dc magnetization data arise from the statistical errors and the uncertainty of the volume of the small piece used for the dc magnetization measurements.

Finally, the validity of the fits as obtained with the different models has been tested by comparing the average magnetization of the fitted profile (see Figs. 3.4 and 3.5 c, f, and i; and 3.8) with the experimental value as obtained from dc magnetization measurements. The result is summarized in Figure 3.9 which shows the magnetic moment from the field-cooled dc magnetization measurements at 100 Oe and 4 kOe (solid lines) together with the magnetic moments as calculated from the best fits of models 1, 1a, 2 and 3 to the PNR curves at 100 Oe and 4 kOe (symbols). This comparison shows a very good agreement for models 1 and 1a and large discrepancies for models 2 and 3. For model 3 where the ferromagnetic moments in the LCMO and YBCO layers are assumed to be parallel, the calculated magnetic moment is almost twice as large as the measured one. For model 2 the calculated magnetic moments are significantly smaller than the measured ones. Evidently, this is the consequence of the assumption that the ferromagnetic moment in the YBCO layers is antiparallel to the ones in the LCMO layers. This comparison clearly argues against models 2 and 3 and emphasizes the relevance of models 1 and 1a in terms of the depleted layer on the LCMO side of the interfaces. The discrepancy between the calculated magnetic moment of models 1 and 1a and the experimentally measured value never exceeds 15 % and it is almost within the error bars. Given the simplicity of the model, with its simple block like potentials, this agreement can be considered as excellent. This analysis further confirms that the depleted layers properly account for the reduced magnetization from FC measurements as compared with bulk values. As the PNR and the FC measurements are independent, their match testifies to the good quality of the fits and their physical significance.

3.3.3. Temperature dependence of the magnetic depth profile

After comparing the PNR curves at 100 and 4 K as shown in Figures 3.4, 3.5 and 3.8 it becomes evident that the main changes in the shape of the reflectivity curves occur in the region around the 3rd order SLBP. At 100 K the intensity of this peak is similar for positive and negative neutron spin polarization. At 4 K, on the other hand, there is a clear
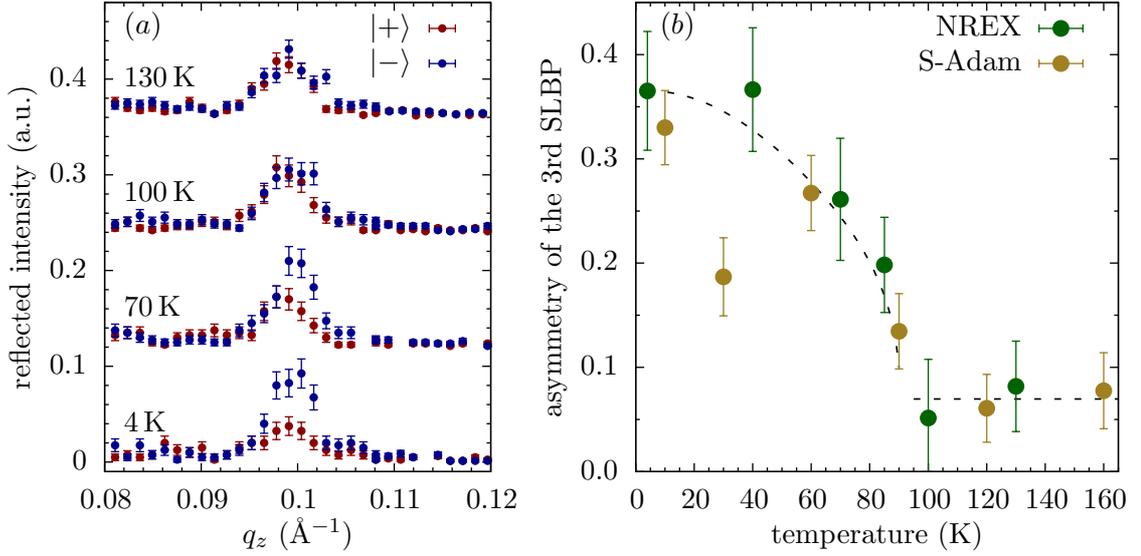
Figure 3.10: (a) Polarized neutron reflectometry curves of YLCM in the region around the 3rd order SLBP for different temperatures, the curves are shifted vertically for clarity. (b) Corresponding temperature evolution of the 3rd order SLBP asymmetry. The dashed line is a guide to the eye.

separation between the two curves and the peak for negative (positive) spin polarization has a higher (lower) intensity. As shown in Figure 3.10, the splitting does not evolve smoothly with temperature and seems to exhibit a rather sudden change in the vicinity of the superconducting transition temperature in the YBCO layers of $T_C \approx 88\,\text{K}$. Figure 3.10(a) shows the close-ups of the PNR curves at 100 Oe around the 3rd order SLBP plotted on a linear scale. It highlights clear changes between 100 and 4 K. It also shows that between 100 and 130 K the curves do not change significantly, which suggests that the temperature dependence of the 3rd order SLBP is not entirely governed by the one of the magnetization of the sample.

To quantify this effect the asymmetry of the 3rd order SLBP has been calculated as $(I_- - I_+)/(I_- + I_+)$, where $I_\pm$ is the integrated reflectivity around the peak for neutrons with spin parallel or antiparallel to the applied field. Its temperature evolution for the measurements performed using the NREX and SuperADAM reflectometers with an applied field of 100 G is summarized in panel (b) of Figure 3.10. As was already mentioned, the asymmetry does not show a smooth evolution but is suddenly enhanced below about 90 K. The observation of a common trend for the measurements performed at both instruments confirms that this is not an instrumental artifact and that the observed changes in the asymmetry are due to changes in the magnetic depth profile of the YLCM sample. As the magnetization data do not show any significant change below 90 K, the changes in the magnetic depth profile seem to be rather subtle and should not strongly affect the average magnetization of the sample.

To learn more about the changes in the magnetization that lead to the observed temperature evolution of the reflectivity curves, the effect on the asymmetry of the 3rd SLBP has been simulated for different possible changes in the magnetic depth profile. This study is summarized in Figure 3.11 where the fitted magnetic depth profile at 100 K with an applied field of 100 G has been taken as reference. For each panel in the figure the original (gray line) and modified (red line) magnetic depth profiles are shown in the graph on the left-hand side. On the right-hand side the corresponding reflectivity curves in the region of the 3rd SLBP are shown. The reference curve corresponding to the fitted magnetic depth profile is shown in dark colors, the reflectivity curve corresponding to the modified magnetic depth profile is shown in light colors and is shifted vertically for clarity. Panel (a) shows the effect of a modification of the asymmetry in the thickness of the depleted layers at the top and bottom interface for which the total thickness of the depletion zones is maintained. The corresponding reflectivity confirms that such a modification does not alter the intensities of the 3rd SLBP. Panel (b) shows the effect of an increase of the net magnetization of the LCMO layers for which the
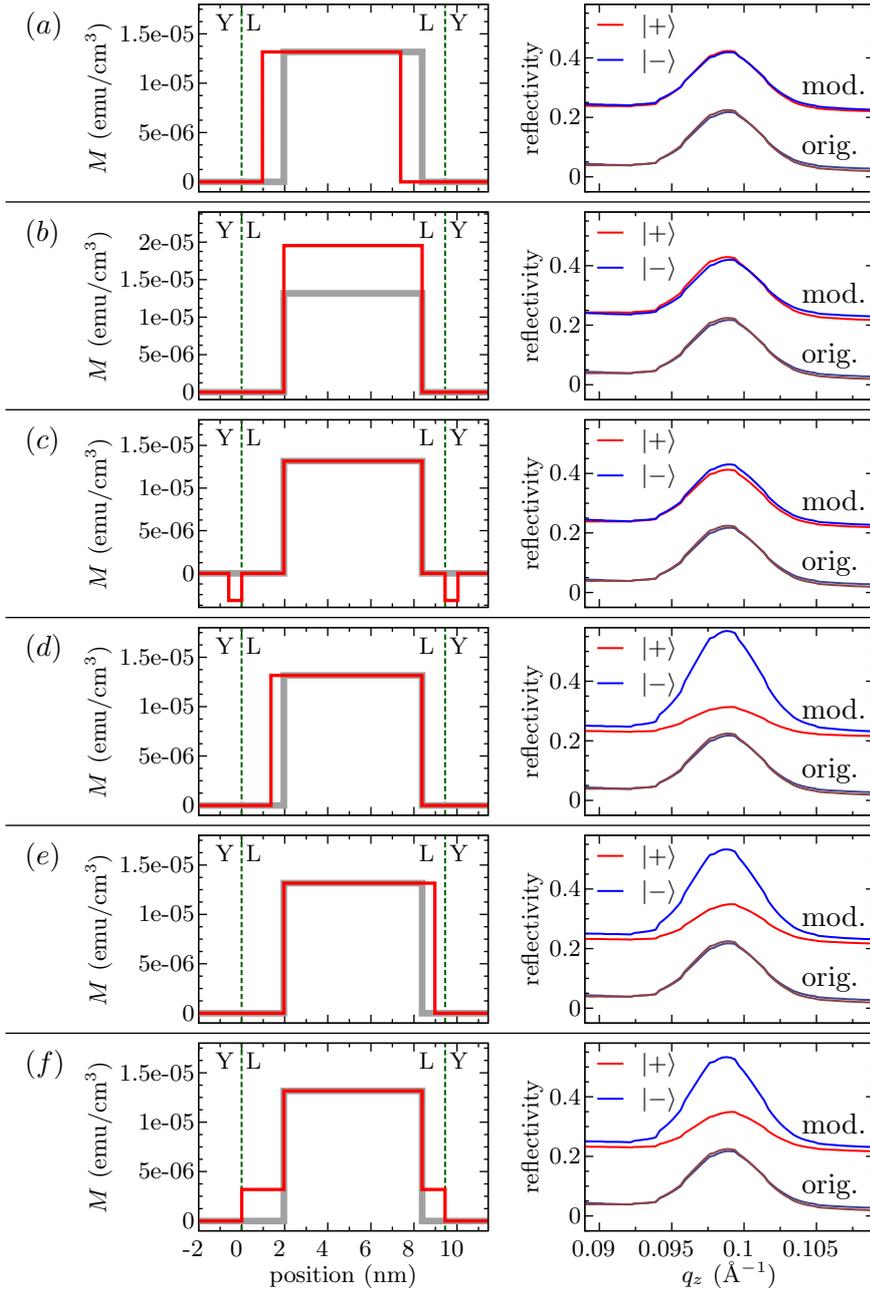
Figure 3.11: Effect on the 3rd SLBP asymmetry of different changes in the magnetic depth profile. The curves on the left-hand side show two possibilities for the magnetic depth profile. The fitted magnetic depth profile at 100 K with an applied field of 100 Oe is shown as a thick gray line and is common for all panels. The red line represents the modified magnetic depth profile which is different for each panel. On the right-hand side the corresponding reflectivity in the region around the 3rd SLBP is plotted. The reflectivity corresponding to the original magnetic depth profile at 100 K is plotted in dark colors. The simulated reflectivity for the modified magnetic depth profile is plotted in light colors and is shifted upwards for clarity.

shape of the magnetic potential remains unchanged. Once more, this does not give rise to a significant change of the 3rd SLBP. Panel (c) shows the case of an induced Cu moment in the YBCO layer which is antiparallel to the Mn moments in LCMO. Such a possibility is suggested by the resonant x-ray studies which are presented in section 3.5. To model this contribution a magnetization of $0.5\,\mu_B$ per Cu ion has been introduced over a distance of 6 Å from the interface. Although this is an exaggerated model the modifications to the reflectivity curves are not large enough to reproduce the effect in the experimental data. Interestingly, the reflectivity curve in the region around the 3rd SLBP is extremely sensitive to the reduction of

the depleted layer thickness on either interface. As shown in panels (d) and (e), a reduction by 6 Å in the depleted layer thickness at the bottom or top interface, respectively, yields a drastic change in the intensity of the 3rd SLBP and the asymmetry observed at low temperatures is reproduced. This change in the asymmetry can also be reproduced if a small magnetic moment is introduced in the depleted layers as shown in panel (f). This is not surprising, as was already discussed when comparing models 1 and 1a to fit the reflectivity data, within the detection limit it is not possible to tell between a reduction in the depleted layer thickness or the introduction of a small magnetization in the depleted layer. Modification (f) is therefore a combination of modifications (d) and (e),

The net effect of modifications (d), (e) and (f) is the enhancement of the magnetization at the interface. This analysis thus suggests that the enhancement of the asymmetry of the 3rd SLBP observed below $\sim 90\,K$ is related either to a net reduction of the total thickness of the depleted layers or to a small increase of the magnetization in the depleted layers. According to the fits of the PNR data for models 1 and 1a, it is the depleted layer at the bottom YBCO/LCMO interface that experiences these changes. The origin of these modifications of the magnetic properties of the LCMO layers is, however, not yet clear. Whether the similarity between the 90 K onset temperature for the changes in the 3rd SLBP asymmetry and the superconducting T_C is a coincidence or an evidence of an existing interaction between the superconducting and ferromagnetic order parameters is a question of remarkable interest that should be further explored. The confirmation of superconductivity-induced changes in the magnetic depth profile would represent a remarkable step toward the understanding of the interaction of the superconducting and ferromagnetic order parameters in these oxide-based materials.

It is worth mentioning that the diamagnetic response of the superconductor is a negligible effect in the YLCM superlattice and does not introduce significant temperature-dependent changes to the magnetic depth profile. Since the magnetic field is applied along the planes, the magnetic penetration depth is enlarged by the weak contribution to the shielding of the c-axis response. Both the in-plane penetration depth of about 100-200 nm and the c-axis penetration depth on the order of a micrometer are much larger than the thickness of individual YBCO layers [111, 112]. For an applied field of 100 G the corresponding negative magnetization due to the field shielding at the center of the YBCO layers is on the order of $10^{-5}\,\mu_B$ per Cu ion.

3.3.4. Summary

The analysis of the PNR data as shown above provides clear evidence for the presence of a so-called depleted layer on the LCMO side of the interfaces in which the ferromagnetic moment of the Mn ions is strongly suppressed as compared to the one in the central part of the LCMO layers. Although the induction of magnetism on the YBCO side of the interface cannot be ruled-out, it is clearly established that it cannot account for the large symmetry breaking of the neutron potential. This study thus provides an answer to the question first raised in Ref. [30] regarding the origin of the even order superlattice Bragg peaks at low temperatures. The depleted layers extend into the LCMO layers up to distances larger than the calculated interface roughness and therefore are not likely just the result of chemical and/or structural disorder. At the top interface the depleted layer extends over about 3 LCMO unit cells (with a lattice parameter of 3.9 Å) and at the bottom interface it involves even 4-5 LCMO unit cells. The depleted layer thickness also has a significant temperature dependence. When cooling from 100 K to 10 K or 4 K, the asymmetry between the interfaces is reduced and the total thickness of the depleted region decreases considerably. This enhancement of the magnetism at the interface is not smooth but rises sharply below $\sim 90\,K$ as suggested by the changes in the asymmetry of the 3rd order SLBP. Whether this effect is an evidence of the interaction between the superconducting and ferromagnetic order parameters needs to be further explored.

As will be discussed later in section 4.3, the observed depleted layers are not a consequence of the interface disorder but rather have an intrinsic electronic origin. This is evidenced by

the observation that the magnetic proximity effect and thus these depleted layers are almost absent for a corresponding YBCO/LaMnO$_{3+\delta}$ superlattice for which the manganite layers are insulating. The large ferromagnetic moments of the Mn ions persist here right up to the interface. Furthermore, as will be shown in sections 3.5 and 3.6, there is the observation of the XMCD and XRMR studies that a ferromagnetic (or strongly canted antiferromagnetic) order of the Cu moments is induced on the YBCO side of the interfaces of the YBCO/LCMO superlattice. The apparent antiparallel coupling between the induced Cu moments in the YBCO layers and the Mn moments therefore requires that the depleted layer maintains some kind of magnetic order. Likely, this involves canted antiferromagnetic order, a non-collinear magnetic order or a rotation of the magnetic moments away from the direction of the applied field that cannot be detected with the PNR technique which probes the average magnetic moment in the direction of the applied field.

3.4.   X-ray linear dichroism analysis

In the following the results of the x-ray absorption spectroscopy (XAS) and x-ray linear dichroism (XLD) measurements on sample YLCM will be presented. The analysis of the XAS curves in the TEY and FY curves for different polarization directions evidences a change of the Cu electronic environment at the interface that shifts the main absorption peak to lower energies. In addition to the shift, the Cu ions at the interface also show a change in the orbital occupation. All the XAS measurements shown in this section were performed at the XTreme beamline of the Swiss Light Source at Villigen, Switzerland [95].

3.4.1.   XLD at the Mn and Cu-$L_{3,2}$ edges, orbital reconstruction for Cu at the interface

As described in section 2.3.2, the intensity of the so-called white lines at the $L_{3,2}$-edges of the x-ray absorption spectra of transition metals is proportional to the number of holes in the $3d$ orbitals. For linear polarized x-rays the absorption cross-section is determined by the anisotropy of the charge distribution of the $3d$ orbitals. The study of linearly polarized x-ray absorption spectra for different polarization directions thus allows one to study the orbital specific occupancy. This information is essential for the understanding of the electric properties of the complex transition metal oxides, like the cuprate high-T_{C} superconductors and the manganites. In the case of the YLCM sample, it is particularly interesting to study the occupation of the in-plane $3d_{x^2-y^2}$ and the out of plane $3d_{3z^2-r^2}$ e_g-orbitals for both Cu and Mn ions. To perform this analysis of the orbital occupation, the XAS measurements have been performed at the $L_{3,2}$-edge of Mn and Cu using the total electron yield (TEY) and the fluorescence yield (FY) modes. The angle of incidence of the x-ray beam with respect to the sample surface has been set to $15\,^\circ$. The sample has been mounted vertically in a He-flow cryostat with the crystallographic c axis lying in the laboratory horizontal plane. The XAS curves have been measured for linear polarization in the laboratory vertical (σ polarization) and horizontal (π polarization) directions. To enhance the statistics and to ensure reproducibility, each absorption curve has been measured twice.

For the σ polarization the electric field is always parallel to the crystallographic ab plane. In the case of π polarization the main component of the electric field is along the crystallographic c-axis but there is still a residual component along the in-plane direction. The net absorption for the linear polarization parallel to the ab-plane and the c-axis, respectively, is therefore obtained with the following correction [82]:

$$\mu_{ab} = \mu_\sigma, \tag{3.1a}$$

$$\mu_c = \frac{1}{\cos^2(\theta)}\mu_\pi - \tan^2(\theta)\mu_\sigma, \tag{3.1b}$$

where $\mu_{\sigma,\pi}$ are the measured absorption data for σ and π polarization, respectively, and $\theta = 15\,^\circ$ is the incidence angle. Such a correction could be avoided by using smaller grazing

incidence angles, but this can lead to saturation effects which influence the shape and the intensity of the absorption curves in the TEY mode and thus complicate their analysis. [96].

Figure 3.12(a) shows the x-ray absorption curves on the Mn-$L_{3,2}$ edge measured for the polarization parallel to the c axis and parallel to the ab plane in the TEY mode. The plotted data were obtained after applying the corrections (3.1) to the raw data for vertical and horizontal polarization. The contributions to the absorption from other elements have been subtracted using a linear background correction as outlined in appendix A. The data have been normalized to one well above the edge to yield the absorption per Mn ion. The two main absorption peaks in the surface sensitive TEY absorption curves correspond to the white lines at the Mn-L_3 and Mn-L_2 edges with energies around 641 eV and 652 eV, respectively. These edges arise from electronic transitions from the core $2p$ band to the valence $3d$ band. A closer look into the absorption curves allows the identification of a multiplet structure that is a consequence of the splitting of the $3d$ levels due to the crystal field and the distortions of the MnO$_6$ octahedron in the manganite [113, 114]. In addition, for these transition metals there is a finite overlap between the wavefunctions of the $2p$ core hole that is created during the absorption process and the remaining holes present in the $3d$ band. This results in a core-valence interaction which leads to the broadening of the absorption spectra and the observed overlap between the L_3 and L_2 edges [86, 90]. As shown in Figure 3.12(b), in the FY data the absorption peaks appear heavily distorted due to self-absorption effects which become important when the main contribution to the absorption cross section arises from the studied edge. In this case the penetration depth of the x-ray beam has a strong energy dependence and the FY signal is no longer proportional to the absorption cross-section [98, 115, 116]. The TEY measurements can be distorted by self absorption effects as well, due to the small escape length of the electrons the corrections are however typically small. The strong distortion of the Mn-$L_{3,2}$ absorption spectra in the FY mode prohibit a meaningful analysis.

The intensity of the x-ray absorption curves for linear polarized light is proportional to the number of holes in the $3d$ band. Nevertheless, due to the spatial anisotropy of $3d$ orbitals the contribution of each hole depends on its orbital character and on the polarization direction, see section 2.3.2. The observed linear dichroism, defined as the difference between the x-ray absorption for polarization parallel to the ab planes and to the c axis, is a signature of an anisotropic hole distribution or, in other words, of a difference in the orbital occupation. The nominal composition of the LCMO layers of La$_{2/3}$Ca$_{1/3}$MnO$_3$ corresponds to a density of $\underline{n}_{3d} = 6.33$ holes- or $n_{3d} = 3.66$ electrons- per Mn ion in the $3d$ band. Three of these electrons occupy the three lower energy bands due to the t_{2g} levels, the $n_{e_g} = 0.66$ remaining electrons density correspond to itinerant e_g electrons that are responsible for the conductivity and the ferromagnetic exchange coupling between the Mn ions [18, 39]. Since the levels in the t_{2g} band are equally occupied with one electron and their asymmetric contributions are cancelled out, the dichroic signal arises only from the holes in the e_g band. As described in section 2.3.2, assuming a hole density of $\underline{n}_{e_g} = 3.33$ for the Mn-e_g band it is possible to estimate the e_g electron orbital polarization as:

$$P_{e_g} = \frac{n_{3z^2-r^2} - n_{x^2-y^2}}{n_{3z^2-r^2} + n_{x^2-y^2}} = \frac{19A}{2}, \tag{2.59}$$

where $A = 2(I_{ab} - I_c)/(2I_{ab} + I_c)$, and I_α is the integrated intensity of the white lines in the x-ray absorption curve measured with the polarization parallel to the α direction. To perform the integration of the white lines a hole-independent absorption baseline containing all non-resonant contributions must be subtracted. At the Mn-$L_{3,2}$ edge the contributions of other elements to the absorption are properly removed with the linear background correction and the absorption baseline contains only the so-called edge-jumps. These steps have relative amplitudes of 2/3 and 1/3 for the L_3 and L_2 edges, respectively, as depicted in Figure 3.12(a).

The calculated values of P_{e_g} for different temperatures are shown in Table 3.3. Within the error bars, no important changes in the occupation ratio are observed with temperature and a value of 22% for the electron orbital polarization is found. The e_g electrons therefore occupy preferably the out of plane $d_{3z^2-r^2}$ orbital. This rather large electronic orbital polarization is
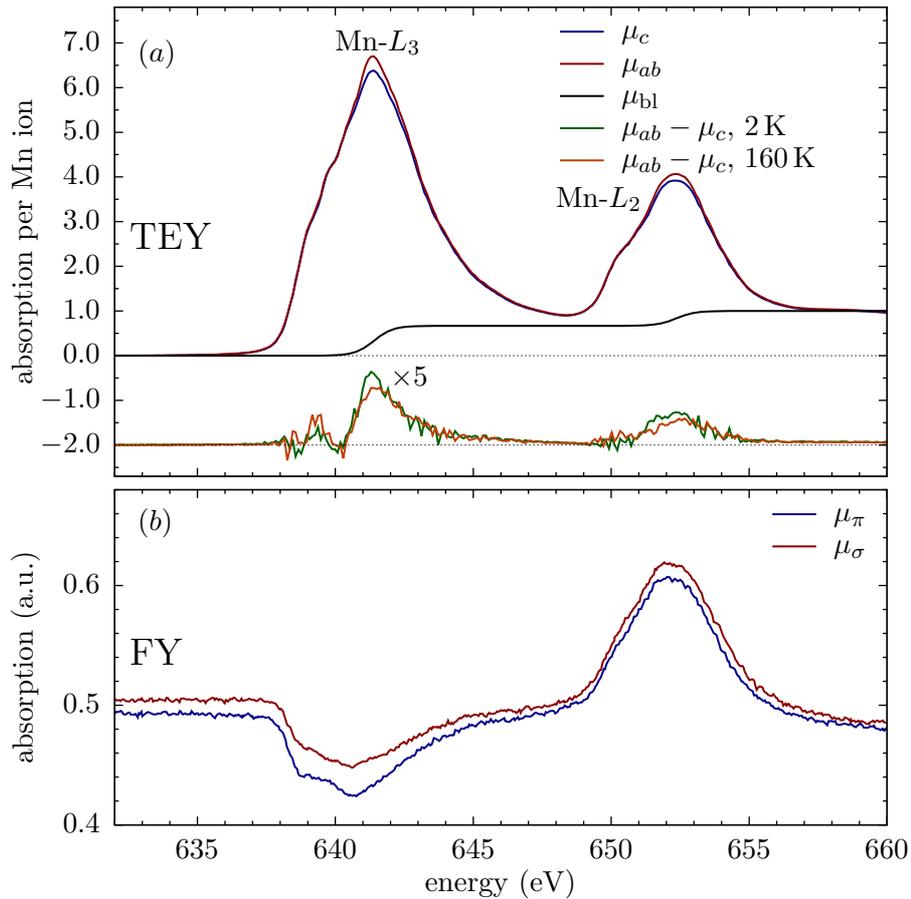
Figure 3.12: X-ray absorption curves at the Mn-$L_{3,2}$ edge of sample YLCM for linear polarization parallel to the c axis and the ab plane, respectively. Panel (a) shows the results for the surface sensitive TEY mode, the x-ray linear dichroism (XLD) at $2\,\mathrm{K}$ and $160\,\mathrm{K}$ is magnified and shifted vertically for clarity. A linear background subtraction and a post-edge normalization have been applied. The absorption baseline, μ_{bl}, used for the calculations is represented by a black line. Panel (b) shows the raw FY spectra that are heavily distorted by self-absorption effects.

found in spite of a very small observed XLD, this apparent contradiction can be understood by recalling that the calculation made is only for the e_g band electron density. The much larger electron density in the t_{2g} band does not contribute to the orbital polarization. The observation of a sizable XLD in LCMO is surprising, for stoichiometric bulk LCMO the e_g energy levels are degenerated and no orbital polarization is expected. A similar orbital polarization has been previously reported on $\mathrm{La_{2/3}Sr_{1/3}MnO_3}$ thin films grown on LSAT and has been attributed to the sample surface where the symmetry is broken and the electrons do not experience the Coulomb repulsion from the missing apical oxygen $2p$ electrons [117]. Lateral strain induced by the substrate could also produce an orbital polarization, nevertheless the lattice mismatch between LSAT and LCMO is less than 0.1% and the effect is almost negligible. The spin-orbit coupling in the $3d$ band could also lift the degeneracy of the e_g orbital. However, contrary to the experimental data, in this case the orbital polarization would be expected to be reduced at high temperatures as the magnetic correlations become weaker. The lack of bulk sensitive measurements makes difficult to tell whether the observed orbital polarization comes from the surface of the LCMO layer or it extends throughout the superlattice. Even though the total orbital polarization remains temperature independent, the XLD spectra in Figure 3.12 are still exhibiting some characteristic changes that arise from a spectral weight shift which may be ascribed to a temperature dependence of the spin-orbit coupling.

The XAS curves measured in the TEY and FY modes on the Cu-$L_{3,2}$ edge of YLCM are shown in Figure 3.13. The corresponding XLD signal calculated in terms of the difference

T (K)	2 K	35 K	60 K	110 K	160 K
P_{e_g} (%)	22(1)	22(1)	21(1)	22(1)	23(1)

Table 3.3: Calculated electron orbital polarization, P_{e_g}, for the Mn ions on the sample YLCM. The calculations were performed after integrating the intensity of the L_3 and L_2 white lines of the Mn linearly polarized x-ray absorption spectra using equation (2.59).
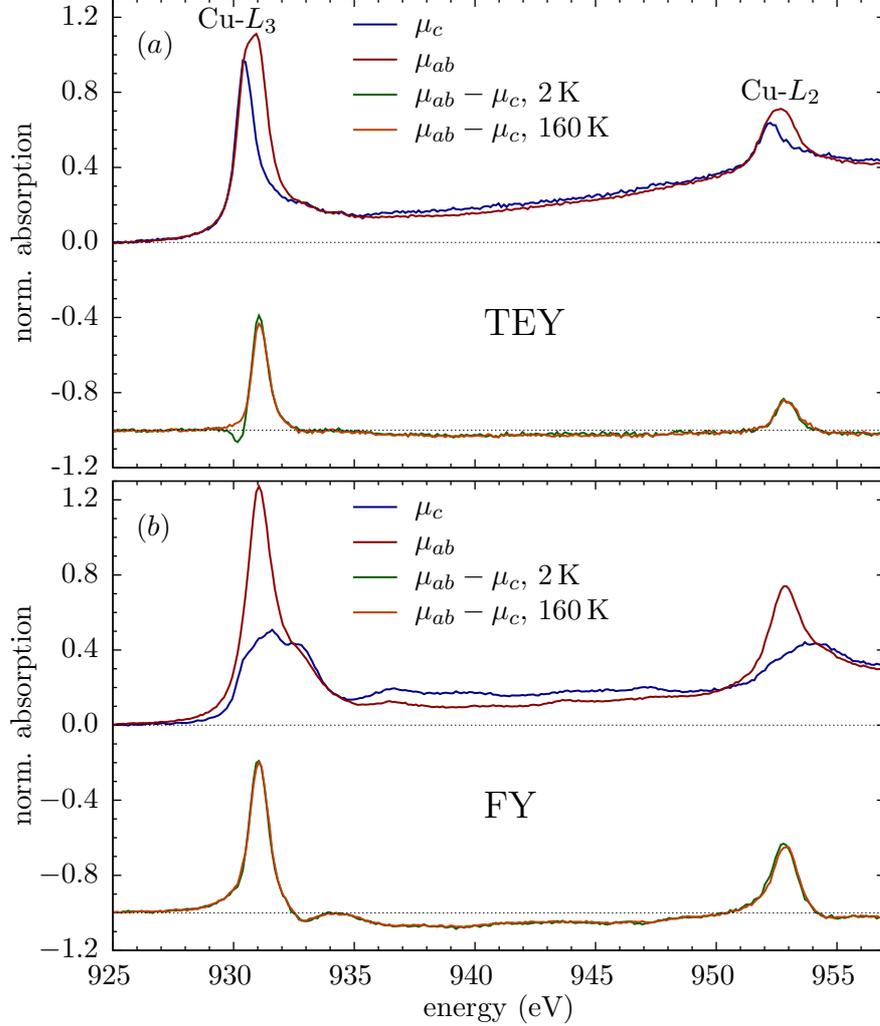

Figure 3.13: X-ray absorption curves at the Cu-$L_{3,2}$ edge of YLCM for linear polarization parallel to the c axis and the ab plane. Panels (a) and (b) show the TEY and FY curves, respectively. A linear background subtraction and a normalization with respect to the L_3 peak of the polarization-averaged absorption have been performed. The x-ray linear dichroism (XLD) at 2 K and 160 K are shown for each case and are shifted vertically for clarity.

between the absorption for polarization along the planes and along the c axis is also shown. The raw data have been corrected using equations (3.1) and a linear background subtraction has been applied following the procedure detailed in appendix A. After these corrections the absorption curves in the TEY mode are still affected by a large background and a normalization after the edge is not reliable. To make the absorption and XLD curves directly comparable, at least at the L_3 edge, the data have been normalized to the maximum of the polarization-averaged absorption, $\overline{\mu} = (2\mu_{ab} + \mu_c)/3$, at the L_3 edge. The peaks in the absorption correspond to the white lines of the Cu-L_3 and Cu-L_2 edges located around 931 eV and 953 eV, respectively. These lines are characteristic of a transition from the d^9 ground state to the $\underline{c}d^{10}$ excited state, where $\underline{c}$ denotes a hole in the core $2p$ level and thus suggest that Cu is mainly in a Cu^{+2} valence state [53]. Since both the ground and the excited state involve

only one hole, the Cu absorption spectra are not affected by core-valence interactions and the peaks are well separated with a clear differentiation between the two absorption edges. The FY signal in the case of Cu does not show the large distortions observed in the Mn case and a qualitative analysis is possible. The self-absorption effects for Cu are expected to be smaller since the high energy of the $L_{3,2}$ edge for Cu enhances the absorption cross section of the other ions in the compound. In addition, for Cu there is only one hole in the $3d$ band which makes the absorption cross section significantly smaller than in the case of Mn. Both, the large total absorption of the media and the small absorption of the Cu ions contribute to the mitigation of the self absorption effects. It should be nonetheless kept in mind that self-absorption effects might still be present. Although these effects cannot change the sign or produce artificial features in the XLD signals, the quantitative analysis of the FY data may still require some corrections.

After comparing both the XLD and XAS curves for TEY and FY modes important differences are evident. To discuss the implications of these differences it is important to recall that the sensitivity of the TEY mode decays exponentially with the distance from the surface. The characteristic length scale is in the range of a few nanometers. In comparison, the characteristic length describing the decay of the sensitivity in the FY mode is of the order of 100 nm which is comparable to the total film thickness. The TEY mode on the Cu edge is thus mainly sensitive to the Cu ions next to the interface with the topmost LCMO layer whereas the FY measurement is almost equally sensitive to all Cu ions in the film.

The XLD curves for the FY mode show a large anisotropy and the absorption is by far largest when the polarization is along the ab plane. At the L_3 edge the XLD intensity reaches about 80% of the average absorption. This is a signature of the CuO$_2$ planes in YBCO where the $3d$ hole occupies predominantly the Cu-$3d_{x^2-y^2}$ orbital. This is due to the Jahn-Teller distortion and to the large hybridization with the O-$2p_{x,y}$ orbitals. A shoulder at the high energy side of the main peak is also observed in the FY mode and it is stronger for polarization parallel to the planes. This shoulder is the signature of the so-called Zhang-Rice singlets which originate from the antiferromagnetic coupling between the Cu-$3d$ hole and a ligand hole that is distributed over the neighboring oxygen ions [118, 119]. The peak corresponds to a transition from a $d^9\underline{L}$ ground state to a $\underline{c}d^{10}\underline{L}$ excited state ($\underline{L}$ represents the ligand hole). The interaction between the created core hole and the ligand hole raises the energy required for an electron to be excited from the core-band to the available hole in the $3d$ band slightly shifting the peak position. The broadness of the white lines, specially for polarization parallel to the planes, and the fact that the peak maximum differs by around 0.5 eV between the different polarizations suggest that additional transitions with different energies contribute to the absorption peak.

Since for the TEY mode the Cu contribution from the buried YBCO layer is residual and most of the absorption occurs in the top LCMO layer, the Cu absorption is strongly affected by the post-edge oscillations of the much more intense neighboring La-$M_{5,4}$ edge located around 850 eV. Here the white lines are narrower and the Zhang-Rice shoulder is barely visible. For this detection mode the absorption curve for polarization parallel to the c axis shows an intense peak and the XLD is correspondingly reduced to 60% of the average absorption. This suggests that the number of holes on the $3d_{3z^2-y^2}$ orbitals is much larger at the interface than in bulk YBCO. A redistribution of holes to the $3d_{xz}$ or $3d_{yz}$ orbitals would contribute equally to the absorption for out-of-plane and in-plane polarization. It is also unlikely since they are much lower in energy than the e_g levels due to the large crystal field interaction. Notably, the maximum for the out-of-plane polarization is shifted by -0.6 eV with respect to the peak for in-plane polarization. This shift has been attributed to a charge transfer at the interface [35, 37], and can also be explained in terms of a change in the crystal field splitting [120]. Both scenarios correspond to a significant change in the electronic structure of the Cu ions at the interface.
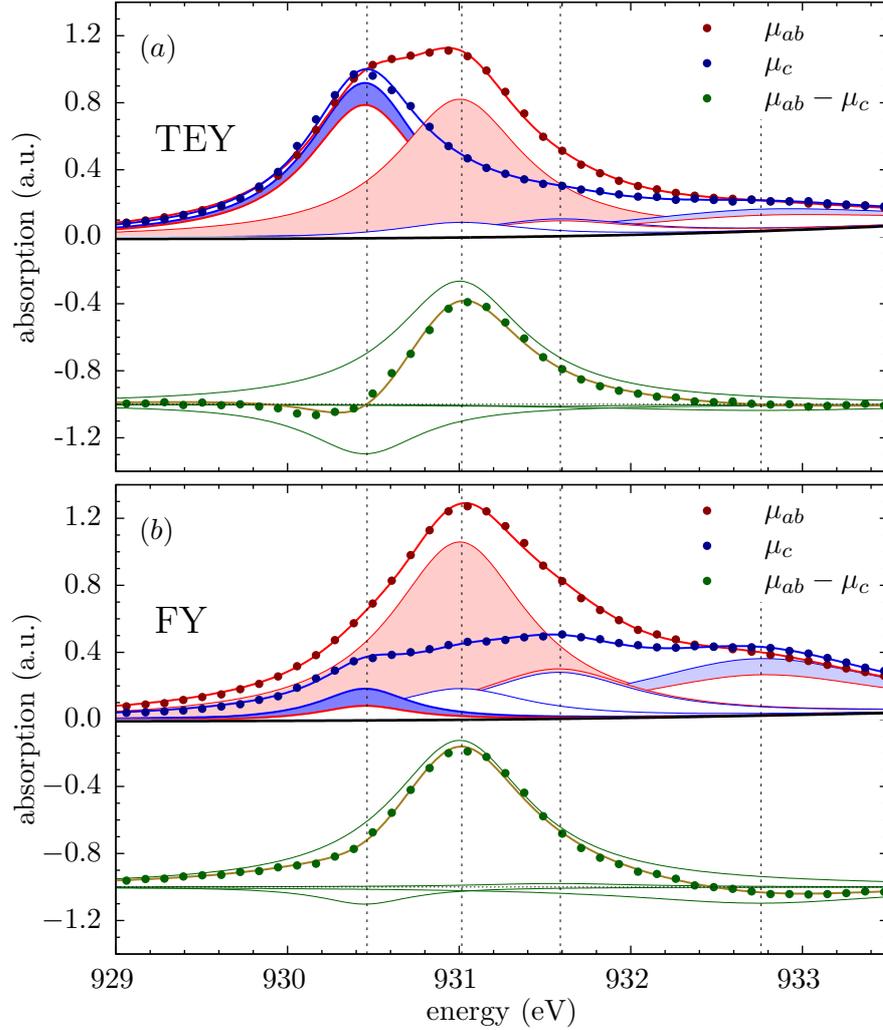
Figure 3.14: Close up of the x-ray absorption curves at the Cu-L_3 edge of YLCM for linear polarization parallel to the c axis (blue dots) and the ab plane (red dots) . Panels (a) and (b) show the results for TEY and FY modes, respectively. The thick lines represent the result of a fit including four Lorentzian peaks and a sigmoidal function to model the background. The individual fitted peaks (thin lines) and the background (black line) are also shown. For each peak the region between the in-plane and out-of-plane contributions is filled with red or blue when the corresponding XLD (green lines plotted below) is positive or negative, respectively. The experimental (green dots) and calculated (olive line) XLD are calculated as the direct subtraction of the experimental and fitted absorption data for different polarizations and are shifted vertically for clarity. The vertical dotted lines mark the position of the peaks.

3.4.2. Multiplet analysis of the XLD at the Cu-L_3 edge

Further information regarding the electronic properties of the Cu ions in YLCM can be obtained from the multiplet structure of the L_3 white line. The multiplet analysis has been performed by fitting the absorption curves around this absorption edge using a set of Lorentzian functions which represent each of the transitions that contribute to the white line. By comparing the intensity of these contributions for the two measurement modes and for the two polarizations one can obtain useful information about the orbital reconstruction at the interface. To model the background and the edge jumps a linear and a sigmoid functions have been introduced and fitted. The background modeling is somewhat arbitrary and care should be taken when comparing the calculations made for the two different detection modes as their corresponding backgrounds might differ considerably. Although the background selection does not modify the XLD signal, it does affect the quantitative analysis as a normalization to the peak area must always be performed. The results of the fits are depicted in Figure 3.14. As

	$\underline{P}_{e_g}$ (%)		w (%)	
	TEY	FY	TEY	FY
Peak 1	-26(4)	-56(18)	41(3)	4.7(7)
Peak 2	84(10)	76(5)	36(4)	45(2)
Peak 3	-5(30)	5(9)	8(2)	20(2)
Peak 4	-20(40)	-23(11)	15(4)	31(3)

Table 3.4: Calculated values for the hole orbital polarization ($\underline{P}_{e_g}$) and spectral weight (w) for YLCM obtained from the fits of the linearly polarized x-ray absorption spectra for TEY and FY mode at the Cu-L_3 edge.

can be seen, a reliable fit is obtained by using a set of four Lorentzian peaks. The absorption spectra is thus a mixture of the contributions of Cu ions in the CuO_2 planes, the Cu-O chains and the interface.

As outlined in section 2.3.2, for each of these contributions it is possible to estimate the hole orbital polarization using the fitted areas and the expression (2.61):

$$\underline{P}_{e_g,i} \equiv \frac{\underline{n}_{x^2-y^2} - \underline{n}_{2z^2-r^2}}{\underline{n}_{x^2-y^2} + \underline{n}_{2z^2-r^2}} = A_i. \tag{3.2}$$

Here once again $A_i = 2(I_{ab,i} - I_{c,i})/(2I_{ab,i} + I_{c,i})$, this time $I_{\alpha,i}$ corresponds to the fitted area of the peak i for polarization along the direction α. This quantitative analysis also allows the estimation of the fraction of the probed Cu ions where a particular transition occurs. To do that, the polarization-averaged absorption of peak i, $2\mu_{ab,i} + \mu_{c,i}$, must be integrated over the L_3 edge. As discussed in section 2.3.2, in the averaged absorption all dependences on the polarization direction are canceled, it is thus directly proportional to the hole density in the Cu-$3d$ band and to the number of probed Cu ions contributing to the particular transition [82]:

$$\int_{L_3} (2\mu_{ab,i} + \mu_{c,i}) = 2I_{ab.i} + I_{c,i} = CN_i \left[2(2\underline{n}_{3z^2-r^2} + 6\underline{n}_{x^2-y^2}) + 8\underline{n}_{3z^2-r^2} \right] = 12CN_i. \tag{3.3}$$

Here C is a proportionality constant, $\mu_{\alpha,i}$ is the fitted absorption of the peak i with polarization along direction α, N_i is the number of probed Cu ions where the transition corresponding to peak i occurs, and $\underline{n}_{x^2-y^2} + \underline{n}_{3z^2-r^2} = 1$ is the hole density in the $3d$ band. The spectral weight of each contribution in the averaged absorption is therefore directly related to the fraction of Cu ions where the transition takes place:

$$w_i = \frac{2I_{ab,i} + I_{c,i}}{\sum_j (2I_{ab,j} + I_{c,j})} = \frac{12CN_i}{12C\sum_j N_j} = \frac{N_i}{\sum_j N_j}, \tag{3.4}$$

where the summation runs over all the components of the absorption. The results for the hole orbital polarization and the weight for the four fitted peaks are summarized in Table 3.4. As discussed in section 2.3.2, the restriction of the analysis to the L_3-edge does not introduce an error in the calculation since the absorption intensity at both $L_{3,2}$-edges contains the same information regarding the orbital occupation.

Numbering the peaks from lower to higher energies, the main peak in the FY absorption corresponds to peak 2 and is located around $E = 931\,\text{eV}$. As already mentioned, this peak corresponds to the transition from a d^9 ground state to the $\underline{c}d^{10}$. For both the FY and the TEY modes the intensity of this peak is much larger for the in-plane polarization owing to the fact that the $3d$ hole in the CuO_2 planes resides mainly in the $3d_{x^2-y^2}$ orbital. The calculated orbital polarization of around 80% is correspondingly large for both detection modes. The weight of this contribution is only slightly reduced when changing from FY to TEY detection modes indicating a similar population of Cu ions with the described properties in the core of the layers and nearer to the interface.

The Zhang-Rice singlet contributions are identified as peaks 3 and 4 and are located at ~ 931.64 and $\sim 932.77\,\text{eV}$. The intensity of these absorption peaks is comparable or even

larger for polarization along the c axis than for in-plane polarization. As the hole density in the $3d_{3z^2-r^2}$ orbital in the CuO_2 planes is largely reduced the out of plane polarization mainly probes the absorption of Cu ions in the Cu-O chains. The Zhang-Rice singlets thus occur mainly in the chains where the holes occupy preferably the $3d_{z^2-y^2}$ orbitals. The polarization along the planes probes both the $3d_{z^2-y^2}$ orbitals and the orbitals along the ab plane. Since there are no holes in the latter, the overall absorption is smaller and that explains the decay in the intensity of the Zhang-Rice peak for the in-plane polarization. The weight of these contributions is reduced by about one half when passing from the FY to the TEY detection mode supporting the occurrence of the Zhang-Rice singlets mainly in the Cu-O chains. Transmission electron microscopy (TEM) measurements in similar YBCO/LCMO superlattices have shown that at the YBCO/LCMO interface the Cu-O chains are missing [25]. Looking from the interface, the first Cu-O chain in the YBCO layers appears therefore only after a CuO_2 bilayer. Due to the exponential decay of the electron escape probability its relative contribution to the absorption is therefore significantly reduced. These results are in good agreement with previous reports where the population of Zhang-Rice singlets in the chains has been found to be around three times larger than in the planes [53].

Peak 1 is of great importance for the analysis of the x-ray absorption spectra in YLCM. While for the FY mode this peak is the smallest of all contributions with a weight of only 4.7%, for the TEY mode it constitutes the largest contribution with a weight of 41%. This remarkably difference suggest that this transition occurs only for the Cu ions in the CuO_2 planes next to the interface. The shift of the peak position by $\sim 0.6\,eV$ toward lower energies evidences a significant charge transfer and a change in the electronic properties of the Cu ions. Moreover, the orbital polarization is inverted with respect to the one observed for the CuO_2 planes far from the interface (represented by peak 2) and a larger hole occupation is thus inferred for the $3d_{3z^2-r^2}$. This orbital reconstruction at the interface has been observed previously in similar YBCO/LCMO systems and has been attributed to the formation of a covalent bond between the Cu and Mn ions via the apical oxygen [35, 37]. The cluster calculations in Ref. [37] show that the strong hybridization between the Cu and Mn $3d_{3z^2-r^2}$ and the O $2p$ orbitals can lead to the creation of bonding and antibonding molecular orbitals. If the energy of the antibonding orbital is larger than the energy of the Cu-$3d_{x^2-y^2}$ one, the Cu hole will occupy this molecular orbital. As the hole is now shared by the Cu, O and Mn ions, the hole density in Cu is reduced and it has a predominantly $d_{3z^2-r^2}$ character which explains the sign change in the XLD. This model is also in good agreement with calculations for cuprate-manganite systems which have shown that the charge transfer is such that holes are transferred from the cuprate to the manganite (or electrons from the manganite to the cuprate) [61]. The cluster calculations predict a full occupation for the $d_{x^2-y^2}$ orbital which is not observed. As shown in Table 3.4 the orbital polarization for the Cu ions at the interface is only -26%. This is a limitation of the model, in a solid the energy levels broaden into bands and if the $d_{x^2-y^2}$ and $d_{3z^2-r^2}$ bands are near the Fermi level they will show partial occupations.

The sizable weight of peak 1 in the FY spectra confirms that the observed orbital reconstruction at the interface is reproduced systematically over all the interfaces in the sample. If the observed effects occurred only at the topmost interface, their contributions to the FY signal would fall below the detection limit. Furthermore, as the escape length of photons is at least eight times larger than the YBCO layer thickness [121], the escape probability within the same YBCO layer can be approximated as constant and the spectral weight of peak 1 should match the ratio between the total number of Cu ions and the number of modified Cu ions at the interface. The peak intensities thus suggest that about 4.7% of the Cu atoms are involved. The fraction of Cu ions at the interface can be estimated using the fitted values of the YBCO layer thickness and the YBCO c-axis lattice parameter. Since there are three Cu planes per unit-cell, the calculation of the total number of Cu planes per YBCO layer yields approximately 25. From this total only two layers or a fraction of 8% are located at the interface. This comparison shows that about 60% of the interfacial Cu atoms (and most likely only those) are involved in the proximity effect. This estimate of the peak intensities is subject to some uncertainty, for example, due to the modeling of the background, self-absorption
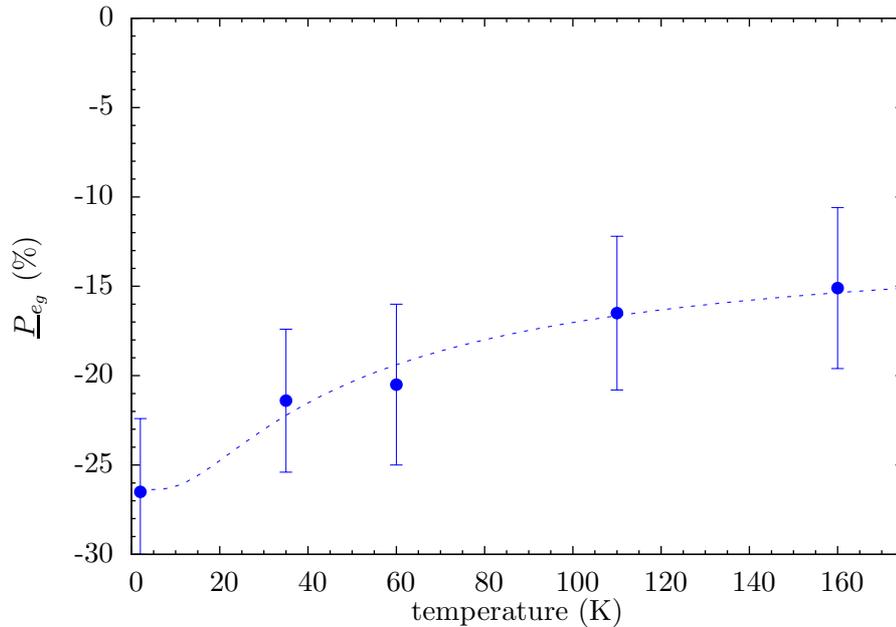
Figure 3.15: Temperature dependence of the hole orbital polarization for peak 1, located $E_1 = 930.44(4)\,\mathrm{eV}$, as obtained from the fits of the linearly polarized x-ray absorption data measured on sample YLCM. The dashed line shows the best fit to the data using a thermal activation-like exponential form $\mathrm{e}^{-\frac{\Delta E}{kT}}$ with $\Delta E = 4(1)\,\mathrm{meV}$.

effects, or to a reduced hole density of the Cu ions at the interface. In the latter case the fraction would be larger. The contribution of some broader peaks above $935\,\mathrm{eV}$ for which the background is difficult to determine has also been omitted. According to Ref. [54], these originate from transitions into hybridized Cu-4s and Cu-$3d_{3z^2-r^2}$ levels. Notably, these peaks are considerably weaker in TEY than in FY mode which suggests a significant reduction of the hybridization or, in other words, a weaker symmetry breaking of the local structure around the interfacial Cu atoms. Whether this is due to a reduction of the Jahn-Teller distortion or of the buckling of the CuO_2 plane needs to be further explored.

An additional consideration needs to be made when comparing the XLD spectra at $2\,\mathrm{K}$ and $160\,\mathrm{K}$ as shown in Figure 3.13. For the FY data, the linear dichroism for the two temperatures overlap, as expected for an orbital polarization resulting from a structural anisotropy. In the TEY case, on the other hand, a clear change in the shape of the XLD is observed on the low energy side of the Cu-L_3 white line. This temperature-dependents effects were rule out in Ref. [37] but for sample YLCM they are robust and reproducible. By comparing the results of the fitted absorption curves for different temperatures it becomes evident that this change in the shape of the XLD is produced by a change in the orbital polarization of peak 1, i.e. the peak that is assigned to the electronically modified Cu ions at the interface. As seen in Figure 3.15, the orbital polarization is decreased with the temperature and passes from $\sim -26\%$ at $2\,\mathrm{K}$ to $\sim -15\%$ at $160\,\mathrm{K}$, the changes, yet small, are above the error bars of the fitting procedure. These changes in the orbital polarization might have a thermal or a magnetic origin. As already mentioned, the energy difference between the antibonding and the $d_{x^2-y^2}$ orbitals is not large and, if it is on the meV range, the thermal energy could promote some holes to occupy the high energy levels thus reducing the orbital polarization. On the other hand, as will be discussed in section 3.5, the electronically modified Cu ions at the interface show a net ferromagnetic moment and therefore experience an exchange interaction that is induced by the Mn ions at the interface. Via the $3d$ spin-orbit coupling such a magnetic interaction can further modify the orbital configuration and thereby induce temperature-dependent effects.

Since an interpolation of the orbital polarization temperature dependence is needed for the quantification of the x-ray magnetic circular dichroism data, the orbital polarization have been fitted to a thermal activation-like function. The result of this interpolation is shown as a

dashed line in Figure 3.15 and can be seen to reproduce the trend of the orbital polarization. While this function fits the data better than a simple exponential or linear function it should be emphasized that there is no physical model to justify the thermal activation over other possible approaches.

3.4.3. Summary

The orbital polarization at the Mn and Cu edges of sample YLCM has been studied using XAS for light polarized parallel to the c axis and to the ab planes. For Mn, only the TEY measurements can be analyzed since the FY curves are heavily distorted due to self-absorption effects. In the case of Mn, a small difference in the absorption for different polarizations evidences a 20% electron orbital polarization in favor of the Mn-$3d_{x^2-y^2}$ orbital. This unexpected degeneracy of the e_g orbitals is most likely produced by a surface effect. This statement cannot be confirmed because of the lack of bulk sensitive FY data to compare with.

For Cu both the FY and TEY curves could be analyzed. The multiplet fitting of the absorption curves at the L_3 edge reveals that the main changes occur for the Cu ions at the interface where both a charge transfer (evidenced by a peak shift toward lower energies) and an orbital reconstruction take place. The orbital polarization changes from about 80% for Cu ions in the core to about -26% at the interface, the sign change means that the $d_{x^2-y^2}$ orbital becomes energetically favorable for the electrons. This phenomenology has been previously explained in terms of a covalent bonding between the Cu and Mn ions at the interface through the apical oxygen. According to this model the creation of molecular orbitals may promote the Cu hole to occupy the antibonding state, of $d_{3z^2-r^2}$ character. The hole density in Cu is thus transferred to the $d_{3z^2-r^2}$ orbital. Since the hole is shared by the Cu, O and Mn ions this accounts as well for the charge transfer.

The sizable spectral weight from ions at the interface for the FY mode confirms that the orbital reconstruction takes place in all interfaces of the superlattice. From the spectral weight it is possible to estimate that about 60% of the Cu ions at the interface are electronically modified.

3.5. X-Ray magnetic circular dichroism analysis

The PNR analysis has shown that the main feature of the magnetization depth profile is a strong suppression of the ferromagnetic moment on the LCMO side of the interface. The x-ray magnetic circular dichroism (XMCD) analysis discussed in the following shows that, in addition, a small Cu moment is induced on the YBCO side of the interface. Notably, this Cu moment is antiparallel to the Mn moment and the applied field.

3.5.1. XMCD at the Mn and Cu-$L_{3,2}$ edges, induced Cu moment at the interface

As described in section 2.3.3, the XMCD provides element specific magnetic information and therefore allows one to separately study the magnetic states of Cu and Mn ions. To perform the XMCD analysis on sample YLCM, x-ray absorption spectroscopy (XAS) measurements have been performed for circular polarized light with positive (left circular polarization) and negative (right circular polarization) helicity around the Cu-$L_{3,2}$ and Mn-$L_{3,2}$ edges in total electron yield (TEY) and fluorescence yield (FY) modes. Each curve has been measured with a magnetic field of $\pm 0.5\,\mathrm{T}$ applied parallel to the beam direction after a field of $\pm 3\,\mathrm{T}$ was temporarily applied to ensure saturation. Since the absorption cross-section depends on the relative orientation of the magnetization and the photon angular momentum directions, the dichroism has been determined by inverting both the polarization and the magnetic field direction. By using this procedure any instrumental artifacts arising from the changes in polarization or the magnetic field are averaged out. By convention, the photon positive and
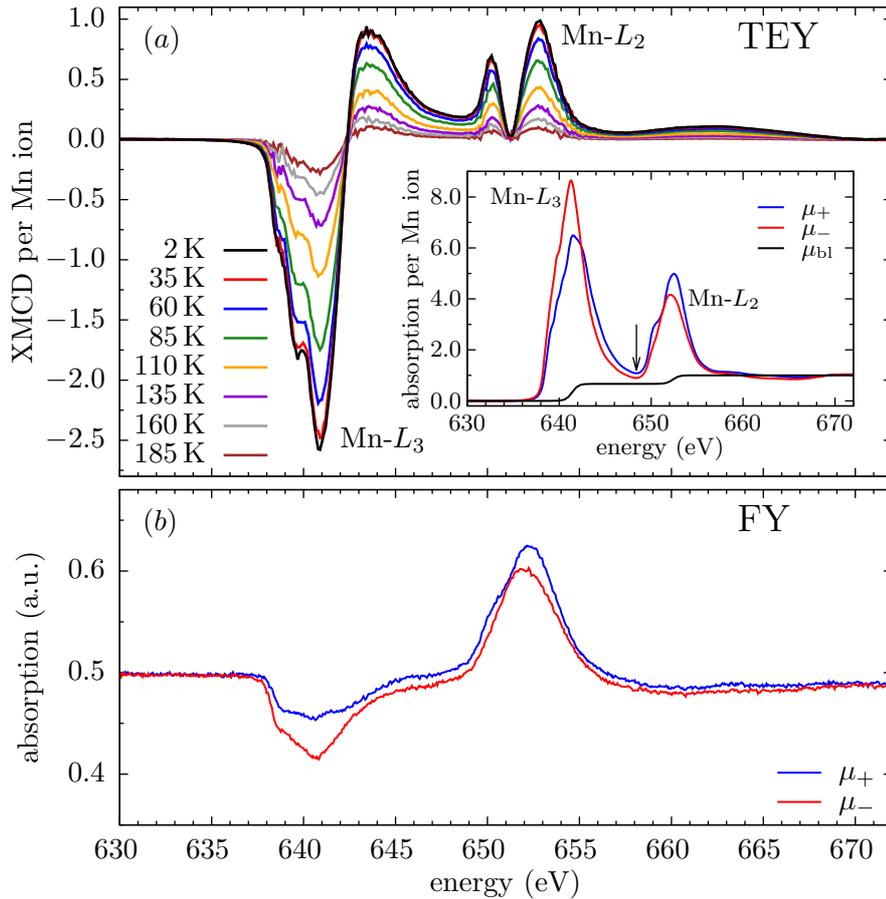
Figure 3.16: XMCD results for YLCM measured at the Mn edge. (a) XMCD signal in the TEY mode calculated as the difference between the absorption for x-rays with positive, μ_+, and negative, μ_-, helicity. Inset: x-ray absorption spectra for different polarizations measured at 2 K in TEY mode. Also shown is the absorption baseline, μ_{bl}, used to perform the quantitative analysis. The spectra have been corrected for a linear background before the edge and normalized to one well after the edge. The arrow marks the selected boundary between the L_3 and L_2 edges that was used to perform the sum rule calculations. (b) Raw x-ray absorption spectra measured in the FY mode, the distortion of the peaks due to self-absorption is evident.

negative helicity directions are defined for photon angular momentum antiparallel and parallel to the applied field, respectively. Since the electron spin is antiparallel to the magnetic moment, positive and negative helicity imply a photon angular momentum parallel and antiparallel to the expected electron spin. To enhance the signal-to-noise ratio and to test the reproducibility of the results, each absorption curve has been measured three times in the case of Cu and two times for Mn. The angle of incidence of the x-ray beam with respect to the sample surface has been set to 15°. The XAS and XMCD measurements shown on this section were performed at the XTreme beamline of the Swiss Light Source at Villigen, Switzerland.

The XMCD results on the Mn-$L_{3,2}$ edge are shown in Figure 3.16. Panel (a) shows the temperature dependence of the XMCD signal calculated as the difference between the measured absorption for positive and negative helicity in TEY mode. Due to the small escape length of electrons ($\sim$ 4 nm) the TEY signal arises predominantly from the very top LCMO layer at the surface of the superlattice. The inset displays the averaged absorption curves for positive and negative helicity at 2 K. The contributions to the absorption from other elements have been removed by subtracting a linear background before the edge as detailed in appendix A. A normalization to one well after the edge has also been applied to yield the absorption per Mn ion. As discussed for the linearly polarized x-ray absorption, the large hole density in the $3d$ band together with the crystal anisotropy and strong core-valence interactions lead to the overlapping of the L_3 and L_2 edges, this effect introduces some error when using
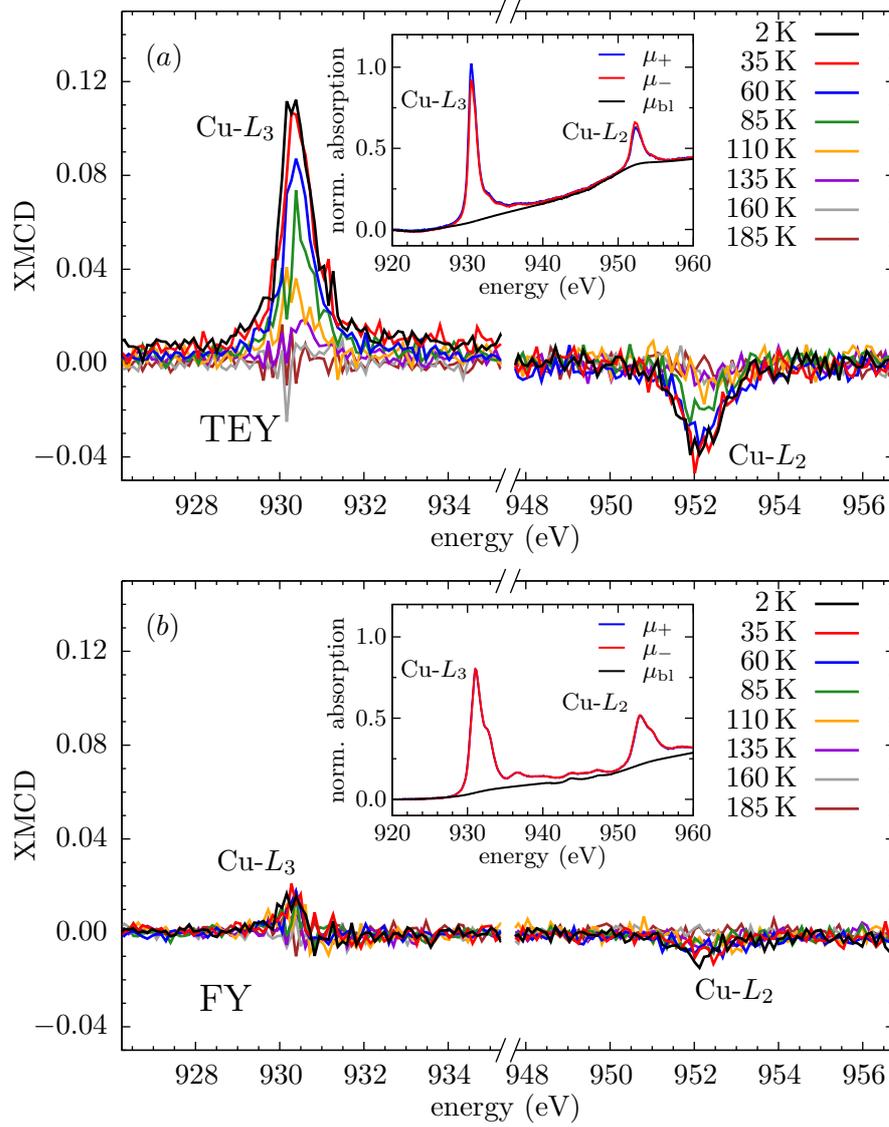
Figure 3.17: XMCD curves of YLCM as measured on the Cu $L_{3,2}$-edge. Panels (a) and (b) show the temperature dependence of the XMCD for the TEY and the FY modes, respectively. The insets show the corresponding XAS measured for positive, μ_+, and negative, μ_-, helicity at 2 K and the background used to perform the XAS integration required for the quantitative analysis, μ_{bl}. The absorption curves have been corrected for a linear background and normalized to the L_3 peak maximum of the polarization-averaged absorption.

the sum rules to determine the magnetization per Mn ion. The absorption curves for positive and negative helicity exhibit large differences, at 2 K the XMCD signal at the Mn-L_3 amounts to about 30% of the average absorption. The complex shape of the XMCD spectra is due to the aforementioned core-valence interactions. Nevertheless, the measured dichroism resembles the one of the bulk manganite systems that are characterized by the coexistence of Mn^{3+} and Mn^{4+} valence states. [122]. The magnetic origin of the dichroic signal is confirmed by the fact that it changes sign from one absorption edge to the other and by its temperature evolution. The top LCMO layer thus exhibits a strong ferromagnetic order. As the temperature increases the amplitude of the XMCD signal decreases and has almost vanished at 185 K, which is close to T^{Curie}.

Figure 3.16(b) shows the Mn-$L_{3,2}$ fluorescence yield spectra measured at 2 K. As for the linearly polarized x-rays, the FY spectra for Mn are heavily distorted due to self-absorption effects forbidding a quantitative analysis.

The XAS and XMCD curves at the Cu $L_{3,2}$-edge of YLCM are summarized in Figure 3.17

where the TEY and FY measurements are shown in panels (a) and (b), respectively. The insets show the corresponding absorption curves measured for positive and negative helicity at $2\,\mathrm{K}$. A linear background has been removed according to the process described in appendix A. To make the absorption and XMCD intensities directly comparable the absorption curves have been normalized with respect to the maximum of the polarization-averaged absorption, $\overline{\mu} = (\mu_+ + \mu_- + \mu_0)/3$, at the L_3 edge. The absorption for linearly polarized light in the direction of the beam, μ_0, has not been measured. It is nevertheless possible to calculate it as a combination of the absorption for in-plane and out-of-plane polarization [82]: $\mu_0 = \mu_{ab}\cos^2\theta + \mu_c\sin^2\theta$, where θ is the incidence angle.

The white lines for both the FY and TEY modes resemble their respective counterparts for the linearly polarized case. In the FY mode, the shoulder corresponding to the Zhang-Rice singlets is pronounced while it is barely visible for the TEY mode. The peak position for the white lines in the TEY detection mode is shifted by $0.6\,\mathrm{eV}$ toward lower energies evidencing that the main contribution to the absorption comes from the electronically modified Cu ions at the interface.

As observed in Figure 3.17, for both the TEY and the FY modes there is a clear XMCD signal. Its magnetic nature is confirmed by the sign change from one absorption edge to the other. This highlights the ferromagnetic order of the Cu moments. In the TEY mode at $2\,\mathrm{K}$ the amplitude of the XMCD signal at the L_3 edge corresponds to around 10% of the average amplitude of the absorption. It should be emphasized that this XMCD is larger than the reported in Refs. [24, 34]. The XMCD signal is reduced as the temperature increases and falls below the noise level for the measurement at $185\,\mathrm{K}$, similar to the case of Mn. For the FY curves, on the other hand, the amplitude of the signal is at least five times smaller and reaches about 2% at $2\,\mathrm{K}$. The finding that the dichroic signal is much larger in the TEY mode which is most sensitive to the Cu ions next to the interface shows that the ferromagnetically ordered Cu moments are confined to the interfaces. Remarkably, the XMCD is positive at the L_3 edge and negative at the L_2 one, as opposed to the XMCD data for Mn for which it is negative at the L_3 edge and positive at the L_2 one. This implies that the ferromagnetic Cu moment is antiparallel to the one of the Mn moments in LCMO and to the applied field. Such an antiparallel alignment is energetically unfavorable and thus evidences that the magnetization in Cu is induced via a strong coupling with the moments of the Mn ions on the other side of the interface.

3.5.2. Multiplet analysis of the XMCD at the Cu-L_3 edge

To better understand the origin of the magnetic dichroism for Cu, a multiplet fitting analysis has also been performed for the absorption curves at the L_3 white line. The results are shown in Figure 3.18. The peak positions are the same than for the curves with linearly polarized light. From the fits to the TEY absorption curves it becomes clear that the circular dichroism arises solely from the lowest energy peak. The ferromagnetic ordering is therefore only present for the electronically reconstructed Cu ions at the interface. The remaining three peaks, assigned to the Cu ions in the bulk of the YBCO layer, do not show any sizable dichroism. A similar result is found for the FY mode. In this case the net contribution of the ions next to the interface is smaller but it yields also the main component of the dichroic signal. The observation that only the electronically modified Cu ions at the interface are magnetic establishes a the direct link between the orbital reconstruction and the magnetism of the Cu ions for the first time.

The main peak, associated to the Cu ions in the CuO_2 planes, shows in the FY case a small dichroism in the opposite direction hence suggesting a magnetic moment parallel to the applied field. This magnetic signal is revealed by a crossover to negative values right after the main peak in the FY XMCD signal at the L_3 edge. Although barely above the noise level, its statistical significance seems to be confirmed by its reproducibility over the different temperature scans as shown in Figure 3.17. This small magnetization in the direction of the applied field could be assigned to a small paramagnetic moment and has been previously
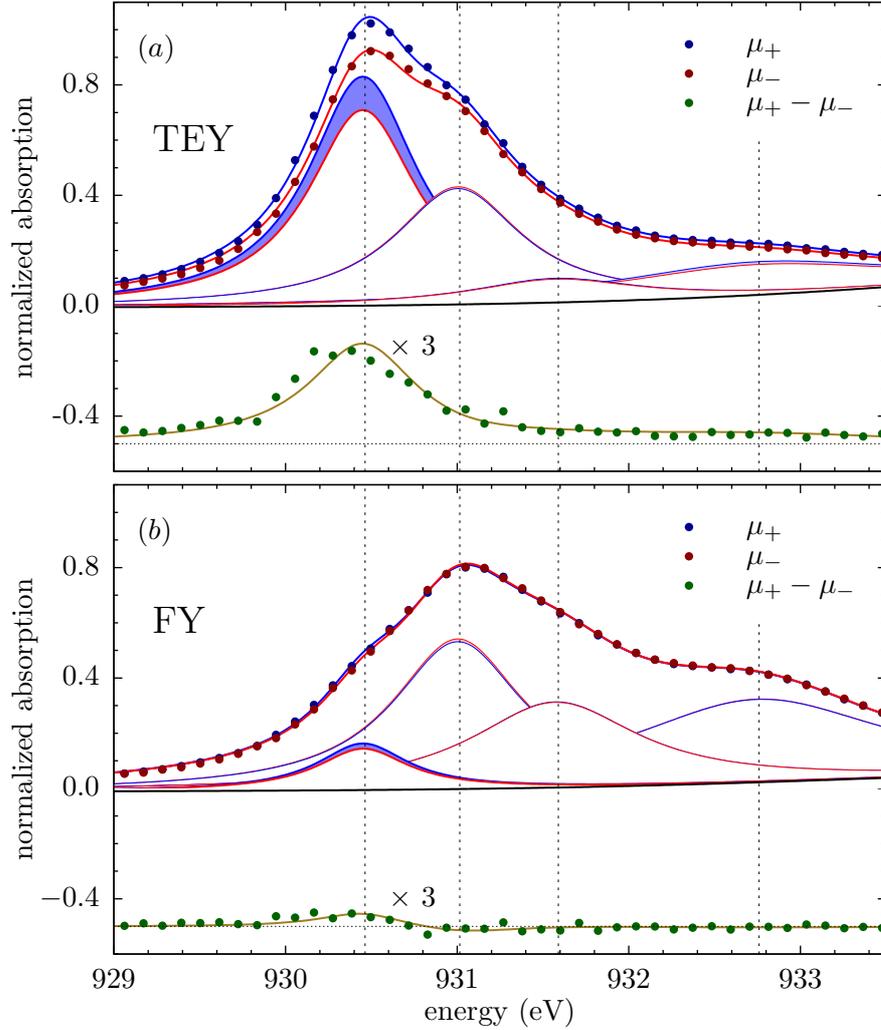
Figure 3.18: Circular polarized x-ray absorption curves measured with TEY (Panel (a)) and FY (Panel(b)) modes at the Cu-L_3 edge of YLCM for positive (blue dots) and negative (red dots) helicity. The thick lines show the fitted curves obtained by using a set of four Lorentzian peaks (thin lines) and a sigmoid function as the background (black line). For each peak the difference between positive and negative helicity is shaded in blue or red when the corresponding XMCD is positive or negative, respectively. The measured (green dots) and fitted (olive line) XMCD are calculated as the difference between the measured and fitted absorption data and are scaled and shifted vertically for clarity.

observed in optimally doped YBCO thin films [123].

The induction of the magnetization in Cu has been previously explained in terms of the covalent bonding at the interface [37]. As a result of the strong Hund's coupling on the Mn site, the energy of the hole shared by the Mn and Cu ions at the interface is minimized if the hole's magnetic moment is antiparallel to the large moment of the t_{2g} band on the Mn site. Since this hole is the only source of spin magnetization in the otherwise filled $3d$ band of the Cu ions at the interface, their net magnetization is antiparallel to the Mn magnetic moment.

3.5.3. Quantification of the induced Cu moment

The next step in the analysis of the XMCD data is the quantitative analysis using the so-called sum rules. As outlined in section 2.3.3, the element specific orbital and spin moments

can be calculated as follows:

$$\langle L_j \rangle = -\frac{2}{3} \frac{\int_{L_3+L_2}(\mu_+ - \mu_-)\mathrm{d}\omega}{\int_{L_3+L_2}\left(\frac{\mu_+ + \mu_- + \mu_0}{3} - \mu_{\mathrm{bl}}\right)\mathrm{d}\omega} \underline{n}_{3d} \tag{3.5a}$$

$$\langle S_j \rangle + \frac{7}{2}\langle T_j \rangle = \frac{1}{2} \frac{\int_{L_3}(\mu_+ - \mu_-)\mathrm{d}\omega - 2\int_{L_2}(\mu_+ - \mu_-)\mathrm{d}\omega}{\int_{L_3+L_2}\left(\frac{\mu_+ + \mu_- + \mu_0}{3} - \mu_{\mathrm{bl}}\right)\mathrm{d}\omega} \underline{n}_{3d} \tag{3.5b}$$

where $\langle L_j \rangle$, $\langle S_j \rangle$ and $\langle T_j \rangle$ are the expectation values of the projection along the beam direction of the orbital moment, the spin moment, and the magnetic dipole operator, respectively. Denoted as $\mu_\pm$ are the absorption data for positive and negative helicity, μ_0 corresponds to the absorption for x-rays linearly polarized along the j-direction and $\underline{n}_{3d}$ is the hole density in the $3d$ band. The absorption baseline, μ_{bl}, which contains all non-resonant contributions still present in the absorption data is now explicitly included.

To accurately use equations (3.5) the knowledge of the number of holes in the $3d$ band, the independent integration of the XMCD spectra over the L_3 and L_2 edges, the normalization with respect to the intensity of the white lines in the absorption spectra, and the precise determination of the expectation value of the magnetic dipole operator $\langle T_j \rangle$ are required. As will be discussed next, in practice these requirements are not always completely fulfilled and give rise to important limitations to the accuracy of the calculations that should be taken into account.

The first consideration concerns the hole density of the $3d$ band of Mn and Cu. The nominal composition of the LCMO layers is $La_{2/3}Ca_{1/3}MnO_3$ which corresponds to a hole density of $\underline{n}_{3d} = 6.33$ in the Mn-$3d$ band that will be used throughout the calculations. The long oxygen annealing process and high T_C of the film YLCM suggest that the stoichiometry of the YBCO layers is close to fully oxygenated $YBa_2Cu_3O_7$. Assuming valences of Y^{3+}, Ba^{2+} and O^{2-} the total valence for Cu in the fully doped compound should be $+7$ which would be distributed between two Cu^{2+} and one Cu^{3+} ions where the former reside on the CuO_2 planes and the latter on the CuO chains. Nevertheless, Cu^{3+} is unstable given the strong Coulomb repulsion that two holes would experience in the $3d$ band and it is energetically more favorable to distribute one hole among the neighboring oxygen sites to promote the above mentioned Zhang-Rice singlets and thus keep the Cu^{2+} valence. The existence of Cu^{3+} would be confirmed experimentally by a strong absorption peak around 940 eV which is not observed in the absorption spectra [118]. Actually, x-ray absorption measurements have shown that the valence state of the Cu ions in the CuO_2 planes does not change significantly from Cu^{2+} within the whole doping range starting from undoped $YBa_2Cu_3O_6$ to fully doped $YBa_2Cu_3O_7$ [53]. The Cu valence of the optimally doped compound is therefore close to $+2$ with one hole in the $3d$ band. Nevertheless, the shift of the absorption peak of the magnetic Cu ions at the interface and the strong orbital reconstruction at the interface suggest that some holes could be transferred from Cu to Mn. An upper bound to the induced Cu moment will be calculated by using $\underline{n}_{3d} = 1$ in equations 3.5. In case of a lower hole density the calculated moments should be interpreted as moments per Cu ion per 3d-hole.

The calculation of $\langle S_j \rangle$ requires the independent integration of the contributions of the L_3 and L_2 edges to the XMCD. In the case of Cu this is not a problem as the XMCD signal is well restricted to the position of the white lines and there is no dichroic intensity for energies between the edges. Nevertheless, in the Mn case both the XAS and the XMCD spectra show an overlap between the L_3 and L_2 edges and there is no clear separation between these two contributions. The standard procedure in this case is to set a boundary at the onset of the L_2 white line [87], for Mn this energy corresponds to 648.4 eV and its position is marked with an arrow in the inset of Figure 3.16(a). This procedure might transfer some spectral weight from the L_3 edge to the L_2 edge which would result in an underestimation of the magnetic moment (up to 40%) [93]. Since the contributions of the two edges to $\langle L_j \rangle$ have the same weight and sign, the calculation of the orbital magnetic moment is not affected by their overlap.

The proportionality constant between the measured electron or fluorescence yield intensities and the actual absorption cross section is generally not known. The data must be thus normalized by the $\underline{n}_{3d}/\int_{L_3+L_2}\left(\frac{\mu_++\mu_-+\mu_0}{3}-\mu_{\rm bl}\right)d\omega$ factor in equations (3.5) which relates the hole density to the polarization-averaged x-ray absorption. Since only the intensity of the white lines is proportional to the hole density, the non-resonant contributions to the absorption $\mu_{\rm bl}$ must be subtracted [87, 124]. For Mn, the linear background subtraction removes properly the absorption contributions from other elements and only the edge jumps contribute to $\mu_{\rm bl}$. The absorption baseline is thus modeled using a step-like sigmoid function with relative amplitudes 2/3 and 1/3 for the L_3 and L_2 edges, respectively, as depicted in the inset of Figure 3.16(a). For the case of Cu this procedure cannot be applied since the background signal is much larger and has an unknown shape. The baseline thus has been approximated by interpolating the absorption data in the regions around the white lines. In this procedure the fact that some sizable XLD signal is observed in the regions above the L_3 and L_2 edges, as shown in Figure 3.13, has been taken into account. This indicates that some spectral weight associated with the holes in the Cu $3d$ band contributes to the absorption in these regions and thus should be accounted for in the normalization. Since these holes have mainly out-of-plane character (they likely involve the hybridization between the Cu-4s and Cu-3$d_{3z^2-r^2}$ levels [54]), it has been assumed that the baseline in this energy range coincides with the measured absorption curve for the linear polarization parallel to the planes, μ_{ab}. To model the baseline at the position of the peaks a smooth interpolation scheme has been introduced which ensures the continuity of the absorption and its first derivative. The resulting absorption baselines are shown by the black solid lines in the insets of Figure. 3.17. Based on the calculation of the magnetic moments using different interpolation schemes, the uncertainty in the absolute value of the magnetic moment has been estimated as about 20%.

The contributions to the XMCD coming from the $\langle S_j\rangle$ and $\langle T_j\rangle$ ground state moments have the same distribution over the L_3 and L_2 edges and thus cannot be separated. The accurate determination of $\langle S_j\rangle$ thus depends on the accuracy with which $\langle T_j\rangle$ can be determined. Strictly speaking, S_j and T_j are the components of the spin and the magnetic dipole operators in the beam (and magnetic field) direction, which in this case has a tilt of $15\,^\circ$ away from the sample surface plane. Although this direction could be redefined as the quantization axis, the crystal anisotropy is more relevant for the discussion of the results and the z direction will be kept parallel to the crystallographic c axis and thus perpendicular to the sample surface. The magnetic dipole operator $\mathbf{T}$ is a measure of the asphericity of the spin moment. In the case of transition metals the contribution of $\mathbf{T}$ to the XMCD will be small as long as the charge distribution in the $3d$ orbitals is symmetric. For oxides, like crystal field effects, the Jahn-Teller distortion and the $3d$ spin-orbit coupling can produce a large anisotropy in the charge distribution and the value of $\langle T_j\rangle$ can be comparable or even larger than $\langle S_j\rangle$ [86]. As discussed in section 2.3.3, if the $3d$ spin-orbit-coupling is smaller than the exchange interaction and the crystal potential, $\langle T_j\rangle$ can be evaluated by summing up independent contributions for each of the $3d$ orbitals. For Cu and Mn the projections of the magnetic dipole operator summed over the t_{2g} band cancel out and for an angle of incidence θ with respect to the surface it is valid to write

$$\langle S_j\rangle + \frac{7}{2}\langle T_j\rangle = \langle S_j\rangle + (s_j^{x^2-y^2} - s_j^{3z^2-r^2})(3\sin^2(\theta)-1), \qquad (2.70)$$

where s_j^i is the spin projection of orbital i. The size of the magnetic dipole correction is therefore proportional to the difference in the spin components for the two e_g orbitals. In principle these spin contributions are not known and, unless the measurements are performed for at least two different angles, a large uncertainty will arise in the determination of $\langle S_j\rangle$. In an extreme case the spin moment in the e_g band would come exclusively from either the $d_{x^2-y^2}$ or $d_{3z^2-r^2}$ orbitals. In this scenario the correction is maximized and amounts to 10% and 80% to Mn and Cu, respectively. For Mn the symmetric contribution of the t_{2g} spins dominates and even in the extreme cases the correction falls within the already expected error in the magnetization due to the overlap of the $L_{3,2}$ edges. The anisotropy correction for Mn
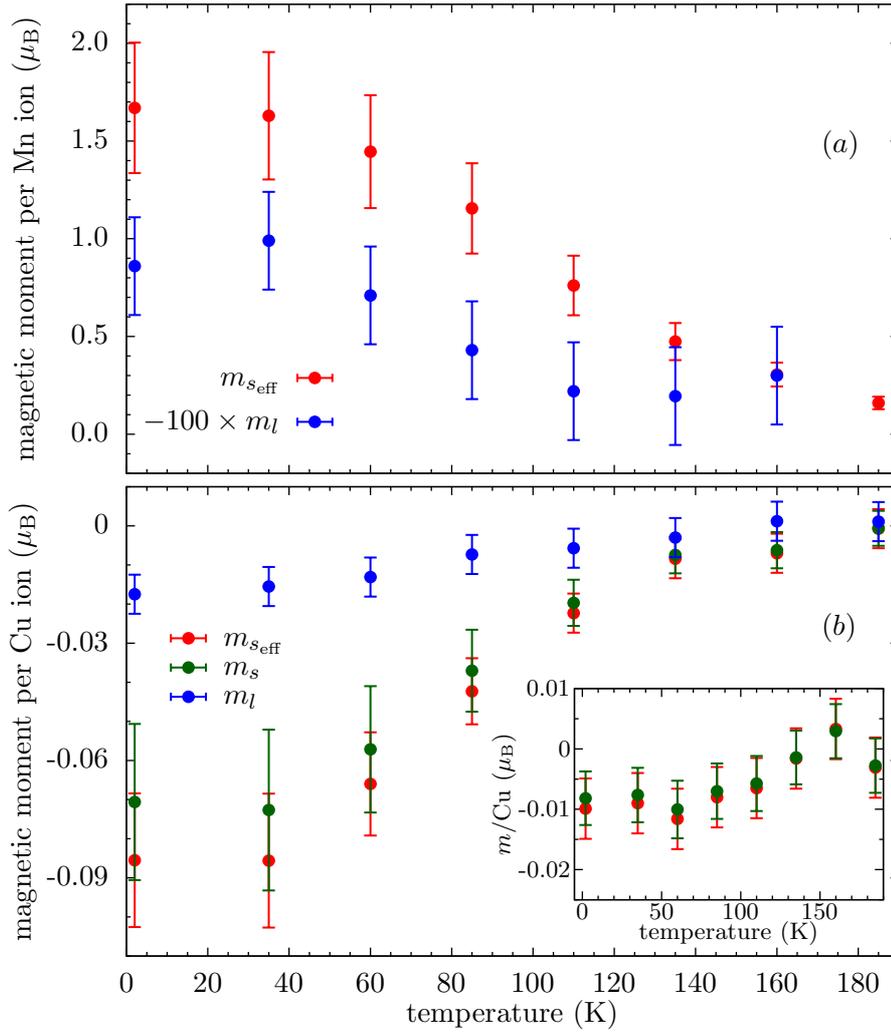
Figure 3.19: Temperature dependence of the spin and orbital magnetic moments per Mn (panel (a)) and Cu (panel (b)) ions calculated after applying the sum rules to the XMCD measured using the TEY mode on sample YLCM. The orbital moment has been calculated from the angular moment as $m_l = \mu_B \langle L_j \rangle$. The effective spin moment has been calculated directly from the sum rules and does not include the magnetic dipole corrections, $m_{s_{\mathrm{eff}}} = -2\mu_B(\langle S_j \rangle - \frac{7}{2}\langle T_j \rangle)$. For Cu, the calculated spin magnetic moment assuming a common spin polarization for the two e_g bands is shown as m_s. The inset in panel (b) shows the results for the data collected using the FY mode, the orbital moment in this case falls below the detection limit.

will be therefore dismissed. For Cu, on the other hand, the e_g hole is the only contribution to the spin and the correction is more important.

Nevertheless, such an extreme spin polarization is unlikely given the large Hund's coupling which promotes the parallel arrangement of spins in the $3d$ band. In a more realistic picture the ratio between holes with spin up and down, hence the spin polarization $\underline{P}_s = (\underline{n}^\downarrow - \underline{n}^\uparrow)/\underline{n}$, is the same for both the $d_{x^2-y^2}$ and $d_{3z^2-r^2}$ orbitals. The spin projection of a particular orbital can therefore be written as $s_j^i = \underline{n}_i^\downarrow - \underline{n}_i^\uparrow = \underline{P}_s \underline{n}_i$ and is proportional to its corresponding hole density. The difference in the spin moments for the two e_g orbitals can be thus written in terms of the difference of their hole densities and one obtains:

$$\langle S_j \rangle + \frac{7}{2}\langle T_j \rangle = \langle S_j \rangle(1 + \underline{P}_{e_g}(3\sin^2(\theta) - 1)), \tag{3.6}$$

where $\underline{P}_{e_g}$ is now the hole orbital polarization of the e_g band as defined in equation (2.61).

Figure 3.19 shows the orbital and spin magnetic moments per Mn (panel (a)) and Cu (panel (b)) ions as obtained using the sum rules (3.5) on the XAS and XMCD data measured using the TEY mode on sample YLCM, for Cu the calculations based on the FY data are also

shown. The orbital magnetic moment has been calculated from the angular moment expectation value as $m_l = \mu_B \langle L_j \rangle$. For both Mn and Cu, $m_{s_{\text{eff}}} = -2\mu_B (\langle S_j \rangle - \frac{7}{2} \langle T_j \rangle)$ represents the effective magnetic moment directly calculated using the sum rules without correcting for the magnetic dipole correction. As mentioned above, in the case of Mn the anisotropy correction is small and $m_{s_{\text{eff}}} \approx m_s$. In the case of Cu, $m_s = -2\mu_B \langle S_j \rangle = m_{s_{\text{eff}}}/(1 + \underline{P}_{e_g}(3\sin^2(\theta) - 1))$ is the magnetic moment after correction (3.6) has been applied using the interpolation for $\underline{P}_{e_g}$ shown in Figure 3.15. As already discussed, the magnetism in Cu occurs at the interface, where the Cu ions are subject to an electronic and orbital reconstruction. Since these Cu ions are associated with the lowest energy peak in the absorption curves, it is the temperature dependent orbital polarization calculated for this particular peak the one that should be introduced in the correction for the spin anisotropy.

As expected, the calculated spin magnetic moment per Mn ion is large and amounts to approximately $1.7\,\mu_B$ at $2\,\text{K}$. This value is smaller than the one obtained from the FC magnetization measurements shown in Figure 3.2 which yielded around $2.1\,\mu_B$ at low temperatures. This difference might be explained by the 2-3 nm thick non-ferromagnetic layer at the sample surface and by the expected underestimation of the magnetic moment due to the overlap of the two Mn-$L_{3,2}$ edges. The orbital magnetic moment appears inverted and amplified in Figure 3.19(a), as predicted by Hund's law, it is antiparallel to the spin magnetic moment. Despite the fact that it is about 100 times smaller than its spin counterpart, it is still well above the noise level and amounts to $0.017(5)\,\mu_B$ at $2\,\text{K}$. The observation of a net orbital magnetic moment can be explained by the spin-orbit coupling which lifts the so-called orbital quenching of the e_g orbitals in the octahedral crystal field [83]. This coupling is further confirmed by the fact that the spin and orbital magnetic moments follow the same temperature dependence.

For Cu the net spin magnetic moment per ion is one order of magnitude smaller than for Mn. Without the anisotropy corrections, it amounts to $-0.086(20)\,\mu_B$ and is well below the Cu^{2+} electronic magnetic moment of $1\,\mu_B$. Assuming that both e_g orbitals have the same spin polarization to account for the spin anisotropy, as expected due to the large Hund's coupling in the $3d$ band, the magnitude of the magnetization is further reduced by about 17%. Under this assumption the magnetic dipole correction is not larger by virtue of the reduced orbital polarization of the Cu ions at the interface. These results for the spin magnetic moment of the Cu ions are obtained after normalizing with respect to the total XAS spectra thus averaging over all the probed Cu ions. A better approximation can be made using the multiplet fittings to the absorption data at the L_3 edge shown in Figures 3.14 and 3.18. As shown in Table 3.4 from these fittings it turns out that about 41% of the probed Cu ions are electronically modified and contribute to magnetism. This spectral weight can be used to scale the calculated moment and obtain the average spin magnetic moment for the electronically modified ions at the interface. This procedure yields an estimate of the spin magnetic moment of $0.18(4)\,\mu_B$ and $0.21(5)\,\mu_B$ with and without the anisotropic correction, respectively. Since the XMCD technique is only sensitive to the projection of the magnetic moments in the beam direction, it is not possible to establish whether the Cu and Mn moments are aligned with the applied field or if the measured magnetic moments correspond to a canting of an antiferromagnetic order or other non-collinear arrangement.

The inset in Figure 3.19 shows the results for the FY mode. The calculated average magnetic moment is ten times smaller than the one calculated in the TEY mode and amounts to $-0.010(5)\,\mu_B$ at $2\,\text{K}$. While it is close to the noise level, it is sizable and shows a clear temperature dependence. The anisotropy correction is in this case within the error bars. As was the case for the orbital reconstruction, the observation of a magnetic signal in the FY mode evidences that the ferromagnetic Cu moment is induced at all the interfaces. This fact is further confirmed by x-ray resonant magnetic reflectometry (XRMR) measurements as will be discussed in section 3.6. The spectral weight of the Cu ions at the interface in the FY absorption spectra is around 4.7% and thus their average spin magnetic moment can be calculated as $0.21(8)\,\mu_B$ at $2\,\text{K}$. This value agrees well with the ones calculated for the TEY mode and testifies to the reliability of the multiplet analysis.
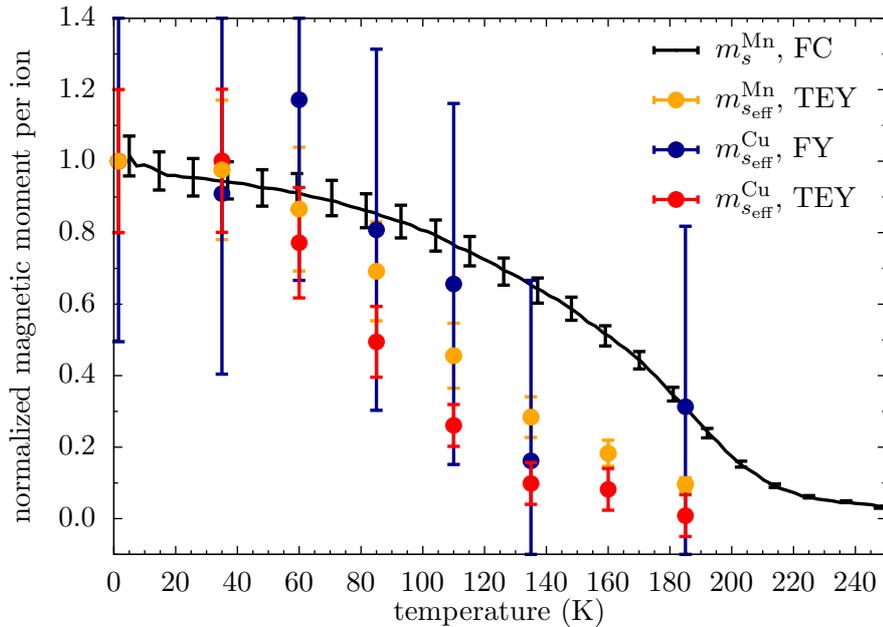
Figure 3.20: Normalized spin magnetic moments for Cu and Mn as calculated using the sum rules on the XMCD measured using the TEY and FY modes on sample YLCM. No anisotropy corrections are taken into account. The normalized FC magnetization measured under an applied field of 4 kOe measured on the sample is also shown.

A sizable orbital magnetic moment is also found for Cu as a consequence of the $3d$ spin-orbit coupling and is in this case parallel to the spin one, as expected for more than half filled $3d$ bands according to Hund's law. For Cu it is about 4-5 times smaller than the spin one and, as in Mn, both moments exhibit a similar temperature dependence. The m_l/m_s ratio at $2\,\mathrm{K}$ is calculated as $0.25(9)$ and $0.20(9)$ with and without taking into account the magnetic anisotropy correction, respectively. Both values agree with the ~ 0.2 reported value for XMCD measurements in YBCO thin films where the magnetic anisotropy has been taken into account [123]. This good agreement shows that the magnetic anisotropy correction has not been overestimated and confirms than an extreme spin anisotropy which would introduce corrections to the spin magnetic moment of up to 80% is unlikely. The covalent bonding model explains the antiferromagnetic coupling between the Mn and Cu ions via the $d_{3z^2-r^2}$ orbital, the magnetic ordering is transferred to the holes in the $d_{x^2-y^2}$ orbital via the Hund's coupling. A more precise study of the magnetic anisotropy in the e_g band of the Cu ions at the interface could be done by performing XMCD measurements using different incidence angles.

Figure 3.20 shows the Mn and Cu spin magnetic moment normalized to their value at low temperatures. The Mn and Cu moments as obtained from the TEY curves show the same temperature dependence confirming that the observed magnetization of Cu is induced by the Mn ions on the other side of the interface. Neither the Mn nor the Cu magnetic moments show any clear changes at T_C. This is not too surprising, the charge transfer and the missing chain at the interface most likely yield a strongly underdoped CuO_2 plane next to the interface that is not expected to be superconducting. This observation supports the PNR analysis which showed that the changes in the magnetic profile below $90\,\mathrm{K}$ occur inside the LCMO layers. The comparison of the Mn and Cu moments calculated from the TEY curves with a FC magnetization curve measured on the same sample shows some differences at intermediate temperatures. This is probably due to the inhomogeneity of the topmost LCMO layer arising from the direct contact with the atmosphere. Modulated by the doping level, antiferromagnetic, canted antiferromagnetic and ferromagnetic regions with different ordering temperatures could coexist near to the sample surface. The Cu spin magnetic moment calculated from the FY data seems to match better the FC magnetization data as expected given its bulk sensitivity. Nevertheless at high temperatures the moment falls below the

detection limit, a clear trend is therefore difficult to observe. The coupling between the Mn and Cu magnetic moments in all the interfaces is confirmed by XRMR measurements as will be discussed in section 3.6.

Although the observed magnetization and orbital reconstruction of Cu ions at the interface have been explained in terms of a covalent bonding with the Mn ions on the LCMO side, the possibility that the Cu XMCD signal may arise from a small number of Cu ions that are unintentionally incorporated within the ferromagnetic manganite layers has not yet been explored. Such an effect could happen due to chemical interdiffusion or another kind of cross contamination during the pulsed laser deposition growth. Against this possibility, it should be mentioned that previous electron energy loss spectroscopy (EELS) measurements performed on YBCO/LCMO superlattices grown under the same conditions of YLCM showed that the interfaces are atomically flat and no evidence of interdiffusion was found within the resolution of the experiment which corresponds to the first monolayer from the interface [25]. This negligible interdiffusion is further confirmed by the depth-sensitive x-ray resonant magnetic reflectometry (XRMR) measurements discussed in section 3.6. The observed depth profile for the magnetization in Cu is consistent with an antiparallel moment induced on the YBCO side of the interface.

3.5.4. Summary

The magnetic properties of the Cu and Mn ions in the sample YLCM have been studied by means of resonant x-ray absorption spectroscopy (XAS) for circularly polarized light in the TEY and FY modes. For Mn, the expected strong magnetism has been observed. The temperature dependence of the magnetization calculated using the TEY XAS spectra and measured from FC magnetization are different. This is probably due to the inhomogeneity of the topmost LCMO layer that is in direct contact with the atmosphere. An orbital moment that is antiparallel and about one hundred times smaller than the spin moment has also been observed. This provides evidence for a weak spin-orbit coupling in the Mn $3d$ band.

In the case of Cu the XMCD analysis confirms a net magnetization that is antiparallel to the applied field. The temperature dependence of the Cu and Mn magnetization is the same, confirming that the magnetism in Cu is induced by the proximity-coupling to the Mn on the other side of the interface. The multiplet fitting analysis shows that the magnetization originates exclusively from the electronically modified ions at the interface. A direct link between the orbital reconstruction and the magnetization of the Cu ions is thus established for the first time. The absorption cross section for Cu is highly sensitive to charge anisotropy and it is not possible to exactly determine the size of the magnetic dipole corrections in the sum rules. By neglecting the correction or assuming an homogeneous spin polarization, which is expected from the large Hund's coupling in the $3d$ band, the average spin magnetic moment per Cu ion at the interface is calculated as $0.21\,\mu_{\rm B}$ or $0.18\,\mu_{\rm B}$, respectively. As was already established from the spectral weight of the modified Cu ions in the FY spectra, this magnetization is confined to about 60% of the Cu ions right at the interface. The origin of the magnetism in Cu can be understood within the framework of the covalent bond at the interface, the energy of the shared hole is minimized when its magnetic moment is antiparallel to the one in the Mn-t_{2g} band.

The orbital magnetic moment of Cu is found to be five times smaller than the spin one, in good agreement with previous reports. This good agreement suggests that the anisotropy correction has not been overestimated and that an extreme spin anisotropy in the Cu-e_g band is unlikely. The covalent bonding picture predicts a net magnetic interaction only for the $d_{3z^2-r^2}$ holes, the magnetic order must be transferred to the holes in the $d_{x^2-y^2}$ orbitals via the $3d$ Hund's coupling. Future experiments performed for different incident angles will allow the exact determination of the magnetic dipole correction and thus will determine if the spin magnetic moment of Cu exhibits only a small spatial anisotropy as suggested here.

The similar temperature dependence of the Cu and Mn moments and the antiparallel alignment with respect to the applied field, both suggest that the Cu moment is coupled to

the Mn moment by which it is induced. Although the largest feature of the magnetic depth profile concerns the suppression of the magnetization on the LCMO side of the interface, the analysis presented in this section confirms that an additional ferromagnetic Cu moment is induced on the YBCO side.

3.6. X-ray resonant magnetic reflectometry analysis

In this section some relevant results obtained using x-ray resonant magnetic reflectometry (XRMR) measurements are briefly discussed. The XRMR technique combines the element-specific sensitivity of the resonant x-ray absorption and the depth sensitivity of the x-ray reflectivity and thus can provide element-specific information of the magnetic depth profile [32, 124].

The first question to be addressed concerns the location of the magnetic Cu ions that are responsible for the observed XMCD signal. The XMCD does not provide enough depth-sensitivity and thus it is not possible to tell for sure from the absorption measurements whether these magnetic ions are located on the YBCO or the LCMO side of the interface. The latter possibility would imply that some Cu ions have diffused through the interface into the LCMO layers. To investigate the location of the magnetic Cu ions, XRMR measurements at the Cu-L_3 edge have been performed. The x-ray reflectivity of YLCM has been measured using an incident x-ray energy of 930.5 eV with circular polarization with positive and negative helicity. The chosen energy coincides with the position of peak 1 in the XAS curves which is the one that has been assigned to the Cu ions at the interface. The XRMR measurements were performed on the UE56/2-PGM1 beamline at BESSY using the MPI-IS ErNST end-station [125]. The simulations of the x-ray reflectivity curves have been performed with the program ReMagX [126].

The results of this study are summarized in Figure 3.21 which has been taken from Ref. [109]. Panel (a) shows the resonant x-ray reflectivity measured at 300 K. The fitting process of the resonant x-ray reflectivity has the complication that it requires the knowledge of the scattering factor, and thus the index of refraction. This quantity depends on the electronic environment of the resonant element. The imaginary part of the scattering factor, $f''(E)$ is proportional to the absorption and can thus be determined by scaling the absorption measurements to tabulated values at energies far from the resonance. The real part of the scattering factor can be then calculated using the Kramers-Kronig transformation which relates the real and imaginary parts of the scattering factor. A more detailed description of the XRMR technique and the calculation of the optical parameters at an absorption edge is given in Refs. [109, 124, 127]. The good agreement between the measured reflectivity and the simulation testifies to the proper determination of the optical parameters by following the above mentioned procedure.

Panel (b) in the figure shows the q_z dependence of the normalized asymmetry calculated as $(R_- - R_+)/(R_- + R_+)$ where $R_\pm$ is the reflectivity measured with circularly polarized x-rays with positive or negative helicity, respectively. The data have been measured at 40 K and with an applied field of about 200 G. The sizable asymmetry evidences a difference in the index of refraction for circularly polarized x-rays with positive and negative helicity. This difference arises from the magnetic contributions to the scattering factor for which the sign depends on the relative orientation of the photon angular momentum and the magnetization of the sample. The asymmetry oscillates as a function of q_z with a periodicity that corresponds to the one observed in the reflectivity curve. The depth profile of the magnetic Cu thus exhibits the periodicity of the superlattice. This observation supports the previous analysis based on the FY XMCD curves which suggested that the Cu moments observed with the surface sensitive TEY mode are not exclusive to the topmost YBCO/LCMO interface but are induced at all the interfaces of the sample.

Furthermore, the asymmetry can be simulated by introducing a magnetic correction to the optical constants which can also be estimated from the absorption curves. The red line
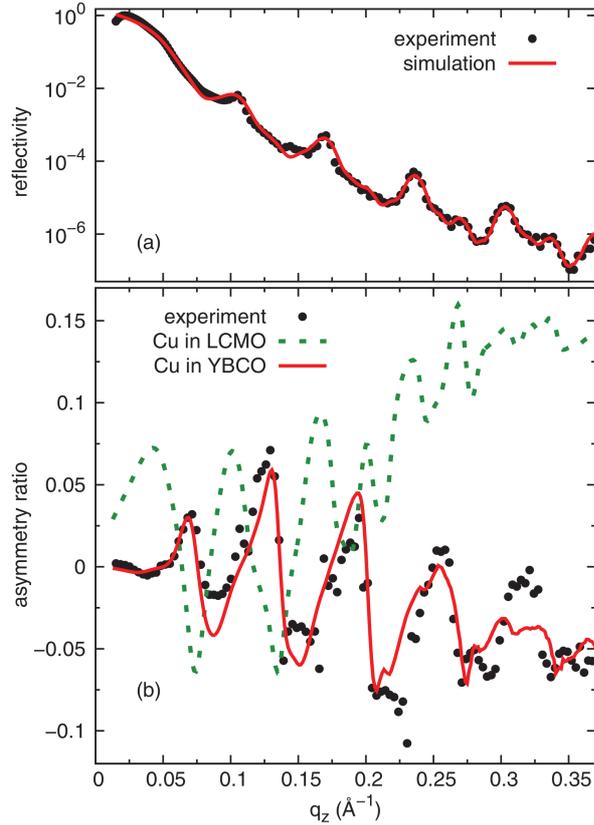
Figure 3.21: X-ray resonant magnetic reflectometry (XRMR) at the Cu-L_3 edge of YLCM. (a) Resonant x-ray reflectivity curve measured at room temperature with an incident beam energy of 930.5 eV. (b) Normalized difference curve between the reflectivity for positive and negative x-ray helicity measured at the same energy at 40 K with an applied field of 200 G. The lines represent the simulated asymmetry assuming that the magnetic Cu ions are located on the LCMO (doted green line) or on the YBCO (red line) side of the interface. The figure has been taken from reference [109].

in panel (b) of Figure 3.21 corresponds to the simulated asymmetry obtained by introducing such a magnetic correction on the YBCO side of the interface using a simple block-like model. Based on the XMCD data, the Cu moment has been assumed to be antiparallel to the applied field and the Mn moments. The estimated magnetic moment from the simulation is around $0.25(10)\,\mu_{\mathrm{B}}$ per Cu ion and agrees reasonably well with the $0.18(4)\,\mu_{\mathrm{B}}$ and $0.21(8)\,\mu_{\mathrm{B}}$ magnetic moments calculated using the TEY and FY XMCD data, respectively. While the simulation could be further improved, for example, by grading the profile of the Cu moments in the YBCO layers, it already reproduces well the main features of the data, such as the peak positions and their intensity variation. Most importantly, the simulation for the opposite case where the Cu moments are assumed to reside within the LCMO layers (dashed green line) is in clear disagreement with the data. The Cu moments are now placed on the opposite side of the interface which gives rise to a π phase shift of the reflected x-ray waves and thus to an exchange of the maxima and minima of the asymmetry curve. A reasonable agreement with the data could only be obtained by changing the mutual orientation of the Cu and Mn moments from antiparallel to parallel. This possibility is however excluded by the XMCD data which highlight that the Cu and Mn moments are antiparallel. The combined analysis of the XMCD and XRMR thus confirms that the Cu magnetic moments reside on the YBCO side of the interface.

Secondly, the coupling between the Cu and Mn magnetic moments has been studied. The coupling between these moments at the topmost YBCO/LCMO interface is evident from their similar temperature dependence (see Figure 3.20). Nevertheless, the lack of bulk-sensitive FY measurements for Mn and the small contribution of the magnetic Cu ions to FY signal
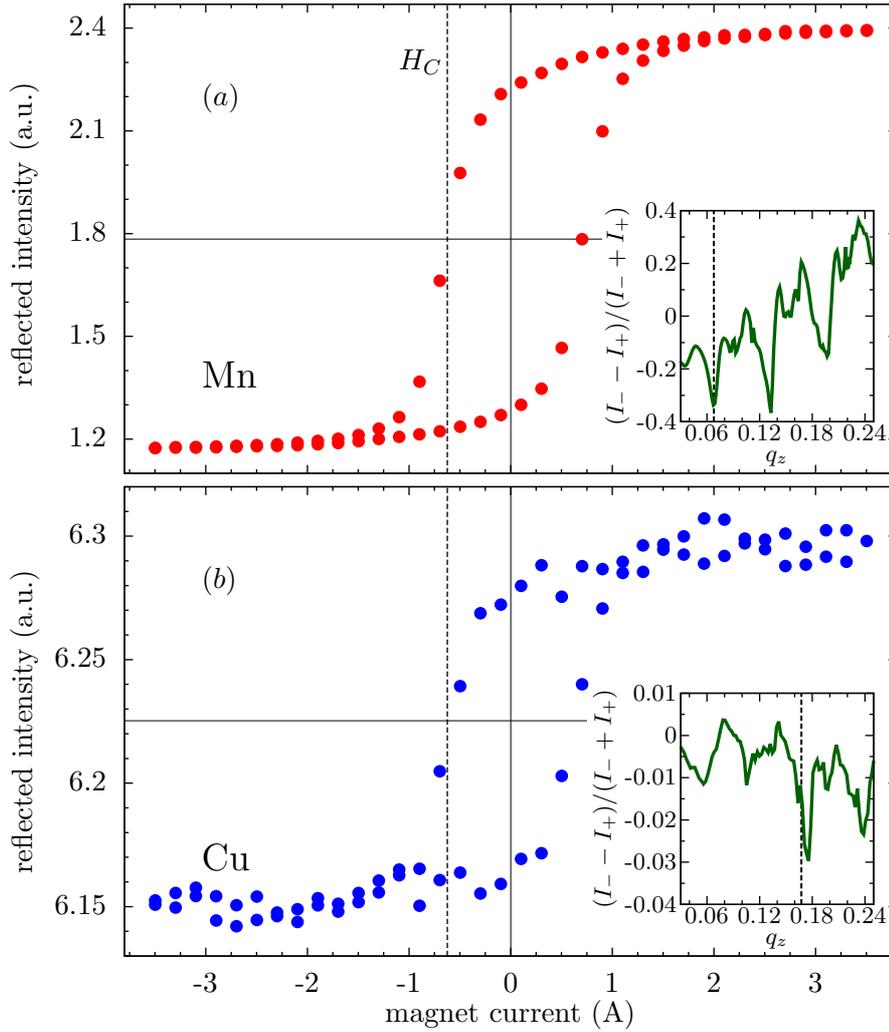
Figure 3.22: Switching behavior of Mn (panel (a)) and Cu (panel (b)) magnetic moments. In each panel the reflectivity at a fixed q_z value is shown as a function of the current in the electromagnet that magnetizes the sample. The measurements were performed at $20\,K$ and the energy was set to $639.9\,eV$ and $930.4\,eV$ for Mn and Cu, respectively. The position of the coercive field H_C is marked with a dashed line. The insets in both panels show the normalized asymmetry of the reflectivity. The thick dashed line marks the q_z at which the reflectivity loops were measured.

makes it difficult to confirm that such a coupling exists in all the interfaces of the YLCM superlattice. These difficulties can be overcome with the resonant x-ray reflectivity curves at the Mn and Cu-L_3 resonances. While in resonance the x-ray penetration depth is strongly reduced, it is still large enough to probe the magnetic properties of several YBCO/LCMO bilayers. To test the coupling between the Mn and Cu magnetic moments in the YLCM superlattice their switching behavior has been studied. For both, Cu and Mn, the reflectivity at a fixed value of q_z has been measured as a function of the current in the electromagnet that was used to magnetize the sample. In each case, q_z has been set to a position where a significant asymmetry is observed. The result of this study is presented in Figure 3.22 which displays the reflectivity measured at the Mn (panel (a)) and Cu (panel (b)) resonances. The measurements where performed at a temperature of $20\,K$ and the incident beam energy was tuned to $639.9\,eV$ and $930.4\,eV$ for Mn and Cu, respectively. The insets in the figure show the normalized asymmetry between the reflectivity measured with circularly polarized x-rays with positive and negative helicity. The dashed lines mark the q_z position chosen for the measurements, these values correspond to $q_z = 0.068\,\text{Å}$ and $q_z = 0.168\,\text{Å}$ for Mn and Cu, respectively. The data are shown in terms of the current through the electromagnet since the relationship with the magnetic field at the sample position is not exactly known. For both Cu

and Mn the reflectivity shows a characteristic magnetic hysteresis confirming the change in the optical parameters as the magnetization of Cu and Mn ions changes with the applied field. The observation of a larger reflected intensity for positive fields in both Mn and Cu reflectivity loops must not be taken as an evidence of a parallel magnetization, the dependence of the reflected intensity with the magnetization direction depends on the particular chosen values of q_z. Notably, the hysteresis loops have the same shape in both cases and the coercive and saturation fields are common for Mn and Cu. This result confirms that the Cu magnetic moments on the YBCO side of the interface are coupled to the magnetization of the LCMO layers and that they flip together in the magnetization reversal process. Moreover, owing to the sensitivity of the XRMR technique to several layers in the superlattice, this coupling can be generalized to all interfaces in the sample.

From the analysis of the PNR data it was determined that the main feature of the magnetic depth profile in the YLCM sample is the strong suppression of the ferromagnetic order of the LCMO layers next to the interface. The results shown in this section and in section 3.5 show that there is still a Cu moment induced on the YBCO side of the interface which is strongly coupled to the magnetization in the LCMO layers. The observation of such a coupling confirms that the so-called depleted layers on the LCMO side of the interface are by no means non-magnetic. The Mn moments must retain a magnetic ordering of canted or oscillatory nature for which the net magnetization along the direction of the applied field is largely reduced [109]. Finally, the question whether the induced ferromagnetic Cu moments in the YBCO layers are playing a significant role for the fitting of the PNR curves has been addressed. Model 1 in section 3.3 has thus been modified to allow in addition to the depleted layers on the LCMO side for a small, antiparallel moment on the YBCO side. It turned out that these Cu moments do not significantly modify or improve the fit results. This is not surprising since these Cu moments are much smaller than the Mn moments in the central part of the LCMO layers and are confined to the CuO_2 layer adjacent to the interface. The PNR curves thus are governed by the larger magnetic moment inside the LCMO layers and are hardly sensitive to the much smaller Cu moment in the YBCO layers.

3.6.1. Summary

The observation of a periodic asymmetry between the reflectivity curves measured at the Cu-L_3 edge for x-rays with different helicity confirms that the magnetic Cu ions are periodically distributed over the interfaces of the superlattice. The asymmetry curve has been simulated assuming that the magnetic Cu ions are located on either the YBCO or the LCMO side of the interface. A much better agreement with the measured data has been found by locating the magnetic Cu ions on the YBCO side of the interface. This result rules out the possibility that the observed magnetism in Cu is a consequence of interdiffusion of Cu into the LCMO layers in support of previous observations with TEM of atomically flat and very sharp interfaces observed in identically grown samples.

The reflectivity curves at the Mn and Cu-L_3 edges show an hysteretic behavior due to the dependence of the index of refraction on the magnetization state of the resonant ions. The hysteresis loops for Mn and Cu are almost identical and thus evidence that the Cu magnetic moments are coupled to the magnetization in the LCMO layers.

3.7. Concluding remarks

The phenomenology of the magnetic proximity effect in a symmetric YBCO/LCMO superlattice has been studied. The sample was epitaxially grown on a LSAT substrate with the pulsed laser deposition technique. The crystallographic c axis is oriented normal to the sample surface and the superconducting and ferromagnetic properties of the individual layers are retained with corresponding critical temperatures of $T_C \approx 88\,K$ and $T^{Curie} \approx 200\,K$, respectively.

The polarized neutron reflectometry (PNR) technique was used to determine the depth profile of the magnetization in the sample. The stability of the substrate and the good quality of the sample allowed the measurement of the PNR curves with a good signal-to-background ratio up to a value of q_z of $0.14\,\text{Å}^{-1}$ at low temperatures. Thanks to the additional information contained in the PNR curves measured over such a large q_z range it was possible to determine that the main characteristic of the magnetic depth profile in the YBCO/LCMO superlattice is the existence of a so-called depleted layer on the LCMO side of the interface in which the net magnetization is substantially reduced. This finding solves the question first raised in Ref. [30] regarding the origin of the observed symmetry breaking of the neutron potential at temperatures below T^{Curie}. Although from PNR the possibility of having a small magnetization on the YBCO side of the interface cannot be excluded, it becomes clear that it could not account for the large differences between the structural and magnetic components of the potential depth-profile. The depleted layers are found to be around 1 and 2 nm thick at the bottom (the one closer to the substrate) and top LCMO interfaces, respectively, and cannot be explained in terms of interface roughness or disorder.

The depleted layers do not show any significant change as the applied magnetic field is increased above saturation. The analysis of the PNR curves for different temperatures shows, on the other hand, that the magnetic properties of the depleted layers are sharply enhanced below 90 K and that the main changes happen in the bottom interface. Whether these changes in the magnetic properties of the LCMO layers are related with the onset of superconductivity in the YBCO layers is a question of great interest which needs to be further investigated. The confirmation of such superconductivity induced changes would be a remarkable step toward the understanding of the interaction between the superconducting and ferromagnetic orders in oxide-based systems.

The magnetic and electric properties of the Cu ions on the YBCO side of the interface have been studied by means of the x-ray absorption spectroscopy (XAS) technique. The comparison of the XAS spectra measured using the surface sensitive TEY and the bulk sensitive FY modes shows that the Cu ions at the interface exhibit a large orbital reconstruction and a net ferromagnetic order with the magnetization antiparallel to the applied field. A multiplet analysis of the absorption curves allowed the identification of the absorption peak that is associated to the Cu ions at the interface. This peak shows a redshift of about 0.6 eV with respect to the main absorption peak corresponding to the Cu ions in the planes far from the interface. The shift of the peak can be explained in terms of a charge transfer at the interface or a change in the crystal field, in either case, a large change in the electronic surrounding of the Cu ions at the interface is inferred. The analysis described in this chapter shows that only the Cu ions at the interface for which the redshift is observed exhibit the aforementioned orbital reconstruction and the ferromagnetic order. A direct link between these two effects is thus established for the first time.

The calculated orbital polarization for the Cu ions at the interface of about -26% is in clear contrast with the one calculated for the Cu ions far from the interface which amounts to about 80%. Such a large change suggests that the electronic environment of the Cu ions at the interface becomes more symmetric. Whether this is due to a reduction of the Jahn-Teller distortion or the buckling of the CuO_2 planes needs to be further explored. The application of the sum-rules to the XMCD data yields an average magnetic moment of $0.18(4)\,\mu_{\text{B}}$ per electronically modified Cu ion at the interface. The similar temperature dependence between the Cu and Mn magnetic moments suggests that they are coupled. This coupling is confirmed by the observation of an identical shape in the x-ray resonant-magnetic reflectometry (XRMR) loops measured at a fixed momentum transfer as a function of the applied field. Moreover, according to the simulations of the XRMR asymmetry as a function of q_z, the Cu ions are located on the YBCO side of the interface. A clear disagreement between the measured data and the simulation is obtained if the magnetic Cu ions are assumed to be located on the LCMO side. This rules out the possibility that the Cu ferromagnetic moment is a consequence of the interdiffusion of the Cu ions into the LCMO layers.

The observation of a Cu magnetization at the interface despite the large reduction of the

net magnetization on the LCMO side of the interface raises the question about the magnetic state of the depleted layers. The observed coupling between the Cu and Mn moments confirms that the depleted layers cannot be thought of as being non-magnetic. A magnetic order which is coupled to the magnetization in the core of the layers must persist right to the interface and be transmitted to the Cu ions. This magnetic order must have a canted antiferromagnetic, non-collinear or oscillatory nature for which the net magnetization along the direction of the applied field is largely reduced.

Finally, the strong suppression of the ferromagnetic moment on the LCMO side of the interface and the orbital reconstruction and magnetization of the Cu ions at the interface have been shown for the first time to occur simultaneously on the same sample. How these three effects are related and their dependence on the particular electric and magnetic properties of the cuprate and manganite layers needs to be further explored.

Chapter 4

Magnetic proximity effect in a YBCO/LMO superlattice

In this chapter the study of the phenomenology of the magnetic proximity effect is extended to a $YBa_2Cu_3O_7/LaMnO_{3+y}$ superlattice. In section 4.1 the sample growth and its structural characterization are discussed. The transport, magnetization and optical measurements that confirm that the LMO layers are ferromagnetic and insulating are presented in section 4.2. Section 4.3 summarizes the polarized neutron reflectometry study of the magnetic depth profile of the sample, the magnetization in the LMO layers is found to be nearly homogeneous. The electric and magnetic properties of Cu are studied with the x-ray absorption spectroscopy measurements shown in section 4.4, the orbital reconstruction and the induction of magnetism in Cu are comparable to the ones observed in the YLCM sample. The concluding remarks are finally given in section 4.5

4.1. Sample growth an structural characterization

The $[YBa_2Cu_3O_{7-\delta}(9\,\mathrm{nm})/LaMnO_{3+y}(10\,\mathrm{nm})]_{\times 10}$ (YBCO/LMO) superlattice, from now on referred to as sample YLM, was grown on a LSAT substrate by means of pulsed laser deposition (PLD). The details about the PLD technique were briefly discussed in section 3.1. This sample was grown under the same conditions as the YLCM sample. The laser fluence was set to around $2\,\mathrm{J/cm^2}$ per $25\,\mathrm{ns}$ pulse at the target surface. The substrate was heated to $825\,^\circ\mathrm{C}$ and the oxygen partial pressure was set to $0.32\,\mathrm{mbar}$. After the growth, the sample was annealed at $485\,^\circ\mathrm{C}$ for $12\,\mathrm{h}$ in an oxygen atmosphere.

The structural properties of the sample were studied with x-ray diffraction measurements using the Rigaku SmartLab system. The results are summarized in Figure 4.1. Panel (a) in the figure displays the x-ray diffraction pattern measured with the momentum transfer normal to the sample surface. The results obtained for the YLCM sample are also shown for comparison. The sample is epitaxial and no trace of impurity phases can be observed. Strong modulations with the periodicity of the YBCO/LMO bilayer testify to the good quality of the interfaces in the superlattice. The LSAT and YBCO peaks can be observed at almost identical positions for both the YLCM and the YLM samples. The lattice parameters of YBCO are therefore not significantly influenced by the replacement of LCMO by LMO. The calculated c-axis lattice parameters for YBCO and LSAT are $c_{YBCO} = 11.71(3)$ Å and $c_{LSAT} = 3.8715(4)$ Å, respectively. On the other hand, a clear difference in the intensity distribution in the region around the substrate peaks can be observed. This weight can only be associated with the LMO layers and the separation from the substrate peaks suggest that the c axis parameter of LMO is larger than the one of LSAT. This observation is in good agreement with the published x-ray diffraction data for undoped or slightly cation-deficient LMO for which pseudo-cubic lattice constants between 3.94 and 3.89 Å have been reported [128, 129]. A rough estimate of the LMO c-axis lattice parameter based on the position of the LMO(003) peak yields $c_{LMO} = 3.93(3)$ Å. The large error bar arises from the uncertainty in the position of the LMO(003) peak which
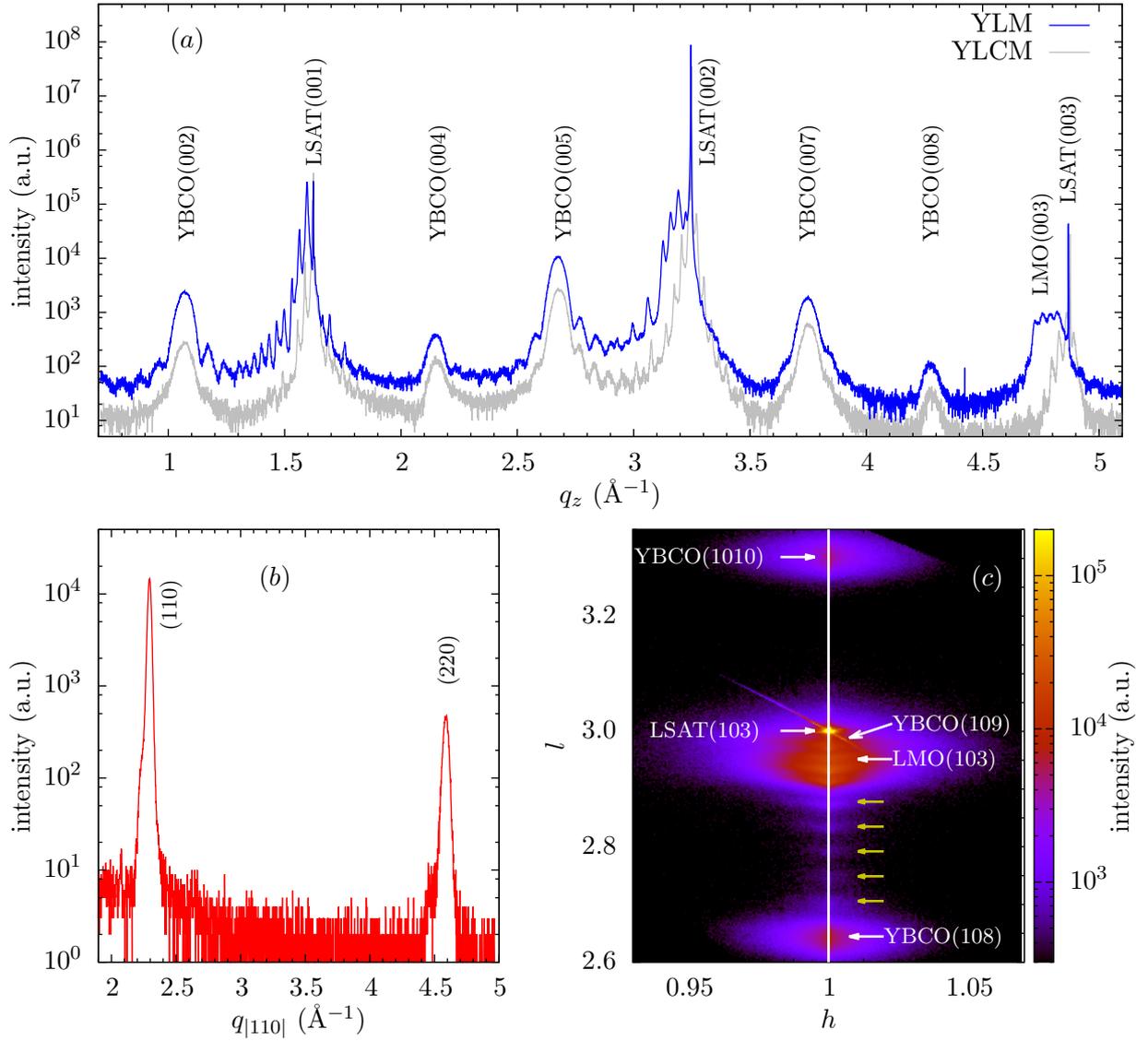
Figure 4.1: X-ray diffraction data for the YLM sample. Panel (a) shows the standard theta-2theta x-ray diffraction curve. For comparison the diffraction curve for YLCM is shown in gray. Panel (b) displays the results of the in-plane x-ray diffraction measurement. In panel (c) the reciprocal space map around the LSAT(103) peak is shown. The yellow arrows in the map mark the superlattice modulations. A pseudo-cubic representation of the LSAT and LMO lattices has been used to identify the diffraction peaks.

is difficult to the determine due to the superlattice modulations and the contributions of the neighboring YBCO and LSAT peaks.

Figure 4.1(b) shows the in-plane x-ray diffraction measurements from which an in-plane lattice parameter of $a = 3.876(5)$ Å is obtained. This value is close to c_{LSAT} and thus suggest that the in-plane lattice parameter of the film matches the one of the substrate. This finding is confirmed by the reciprocal space map around the LSAT(103) peak shown in panel (c). The q_x position of the observed YBCO and LMO peaks matches the one of the substrate peak. Furthermore, the peaks are symmetric around the $h = 1$ line and thus no evidence of lattice relaxation is observed. The good quality of the interfaces is evidenced by the superlattice modulations of the intensity in the l-direction.

In summary, the YLM superlattice keeps its strained condition in spite of the introduction of the LMO layers which are subjected to a sizable compressive strain. The structural properties of the YBCO layers are therefore comparable to the ones of the YLCM sample.
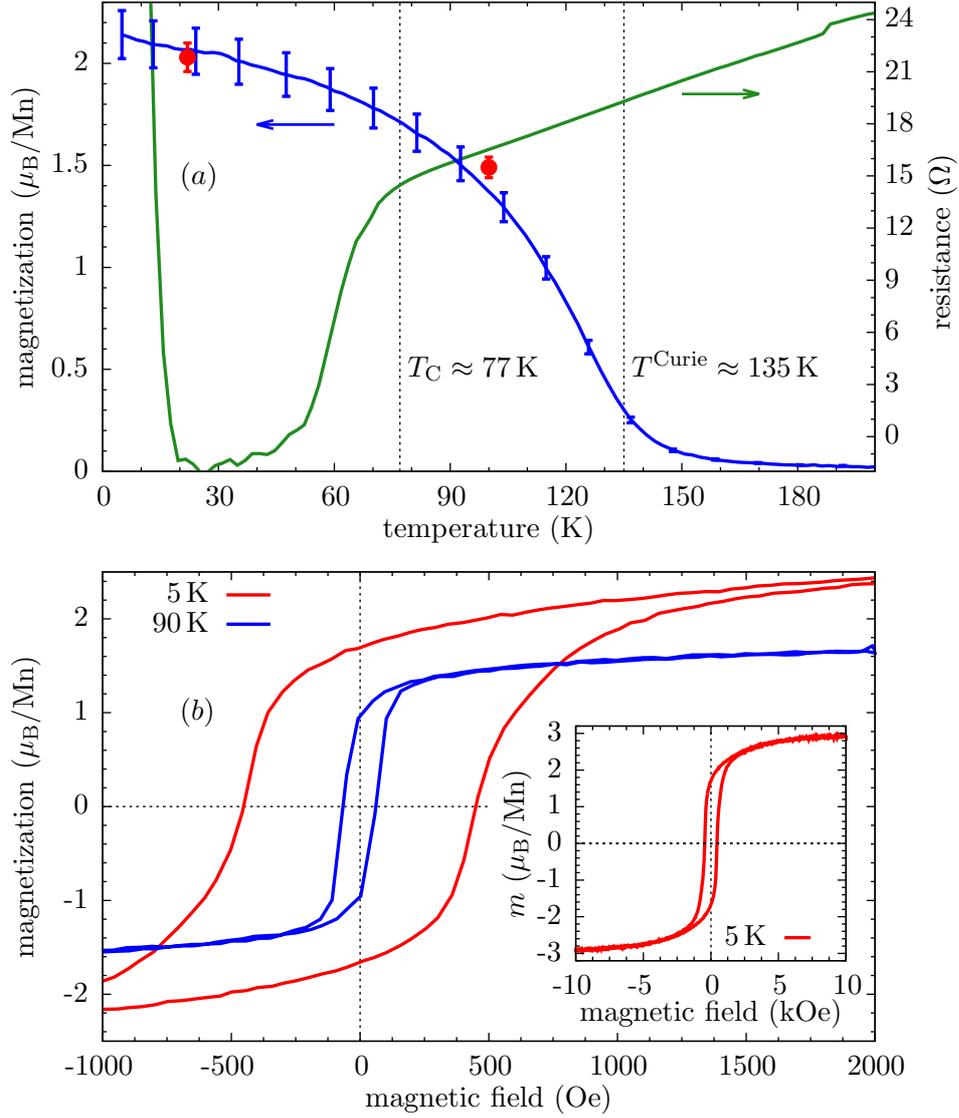
Figure 4.2: (*a*) Temperature dependence of the resistance and the dc magnetization of the superlattice YLM. The magnetization have been measured while cooling with and applied field of 1000 Oe. The doted lines mark superconducting and ferromagnetic onset transition temperatures. The red symbols correspond to the sample magnetization as calculated from the fits of the neutron reflectivity data discussed in section 4.4. (*b*) Magnetic hysteresis loops measured at different temperatures. The inset shows the hysteresis loop measured at 5 K in a wider scale. The magnetization measurements have a $\sim 5\%$ uncertainty that arises from the errors in the determination of the sample area and the LCMO layer thickness and density.

4.2. Electric and magnetic properties

The electric and magnetic properties of the YLM sample have been first characterized with the electric resistance and dc magnetization measurements shown in Figure 4.2. These measurements have been performed using the physical properties measurement system (PPMS) from Quantum Design (model QD6000) and its vibrating sample magnetometer option (model P525). The magnetization has been measured while cooling with an applied field of 1000 Oe on a small piece cut out from a corner of the sample.

Figure 4.2(*a*) shows the temperature evolution of the resistance and the magnetization. The magnetization in μ_B per Mn ion has been calculated using a thickness of $d_{LMO} = 10.4(1)$ nm for the LMO layers, an area of $A = 1.75(6)$ mm^{-2} for the small piece and a density of Mn ions of $16.7(2)$ nm^{-3} as obtained from the PNR data that are discussed in section 4.4. As seen in the figure, the LMO layers are ferromagnetic with a Curie temperature of

$T^{\mathrm{Curie}} \approx 135\,\mathrm{K}$. The average magnetization per Mn ion at low temperatures of about $2.1\,\mu_{\mathrm{B}}$ is comparable to the one found for the LCMO layers of the YLCM sample. The resistivity curve exhibits a superconducting transition with an onset temperature of $T_{\mathrm{C}} \approx 77\,K$. The superconducting critical temperature is thus reduced with respect to the one observed in the YLCM sample suggesting that the YBCO layers in the YLM sample may be slightly oxygen deficient. The oxygen deficiency can be estimated as $\delta \approx 0.2$ based on a comparison with tabulated values of T_{C} for different oxygen concentrations [51].

The magnetization hysteresis loops measured on YLM are shown in panel (b) of Figure 4.2. Similar to the YLCM sample, an enhancement of the coercivity is observed at low temperatures. It is most likely due to an inhomogeneous magnetic phase in the LMO layers [103]. The $5\,\mathrm{K}$ hysteresis curve shows an average saturation moment of about $3\,\mu_{\mathrm{B}}/\mathrm{Mn}$ and a saturation field near $10\,\mathrm{kOe}$. These values are larger than their counterparts measured in YLCM for which a saturation moment of $2\,\mu_{\mathrm{B}}/\mathrm{Mn}$ and a saturation field around $1\,\mathrm{kOe}$ are observed at low temperatures. A comparison with the published magnetization data for cation-deficient LMO samples suggests that the oxygen excess, y, of the LMO layers should be somewhere between 0.11 and 0.14 [40]. As shown in Figure 2.2, for these values a ferromagnetic and insulating phase is stabilized.

Indeed, the insulating character of the LMO layers is suggested by the fact that the resistance of the YLM sample does not show any significant change at T^{Curie}. An insulator-to-metal transition does not seem take place in the LMO layers upon the ferromagnetic ordering. This scenario is further supported by the observation of a steep increase of the resistance below $20\,\mathrm{K}$ and by the negative resistance measured between 20 and $50\,\mathrm{K}$. The latter effect is an artifact which most likely arises because the transport through the highly insulating LMO layers is governed by some defects like grain boundaries. This can result in complex current pathways through the sample and a negative voltage between the measurement contacts.

Nevertheless, since the resistance measured with the four-probe method is mostly sensitive to the topmost LMO layer, the insulating behavior of all the LMO layers in the superlattice cannot be confirmed from these measurements. Moreover, as shown in Figure 2.2, the electric and magnetic properties of the LMO layers are extremely sensitive to the oxygen content. It is thus plausible that due to its direct exposure to the atmosphere the topmost layer may have a different doping level and thus different properties than the inner layers of the YLM superlattice. To study the electric properties of all the LMO layers in the sample, the optical conductivity has been determined from infrared ellipsometry measurements. With this technique the changes in the polarization of linearly polarized infrared light upon reflection on the sample are used to calculate the dielectric function and thus the conductivity of the sample [130]. The probe depth of the infrared light is in excess of $200\,\mathrm{nm}$, this technique thus provides the required information about the electric properties of the inner layers.

The results of this study are shown in Figure 4.3 where the corresponding measurements for the YLCM sample are also presented for comparison. The figure has been taken from the online supplemental material of Ref. [109]. Panels (a) and (c) in the figure show the real part of the optical conductivity of the YLCM and YLM samples, respectively, measured at different temperatures. The corresponding temperature evolution of the spectral weight for different energy regions is shown in panels (b) and (d). For both the YLCM and the YLM SL the spectra reveal a pronounced spectral weight shift from high energies at $T > T^{\mathrm{Curie}}$ to the low energy region at $T < T^{\mathrm{Curie}}$ that is a well known hallmark of the colossal magneto-resistance transition in the manganites [131, 132]. However, while for the YLCM superlattice a significant amount of this spectral weight is accumulated in a Drude-like peak centered at zero frequency, for the YLM superlattice all of the spectral weight is contained in a mode that is centered around $0.6\,\mathrm{eV}$ with no significant weight at zero frequency. Notably, a very similar behavior was previously reported for a $\mathrm{La_{1.9}Sr_{0.1}MnO_3}$ single crystal when it entered the ferromagnetic insulating state [131]. This behavior has been interpreted in terms the formation of orbital and magnetic polarons that are strongly coupled to the lattice (and pinned to defects thereof) [41, 42]. The characteristic spectral weight transfer that is observed below T^{Curie} in the optical spectra of the YLM superlattice thus confirms that the LMO
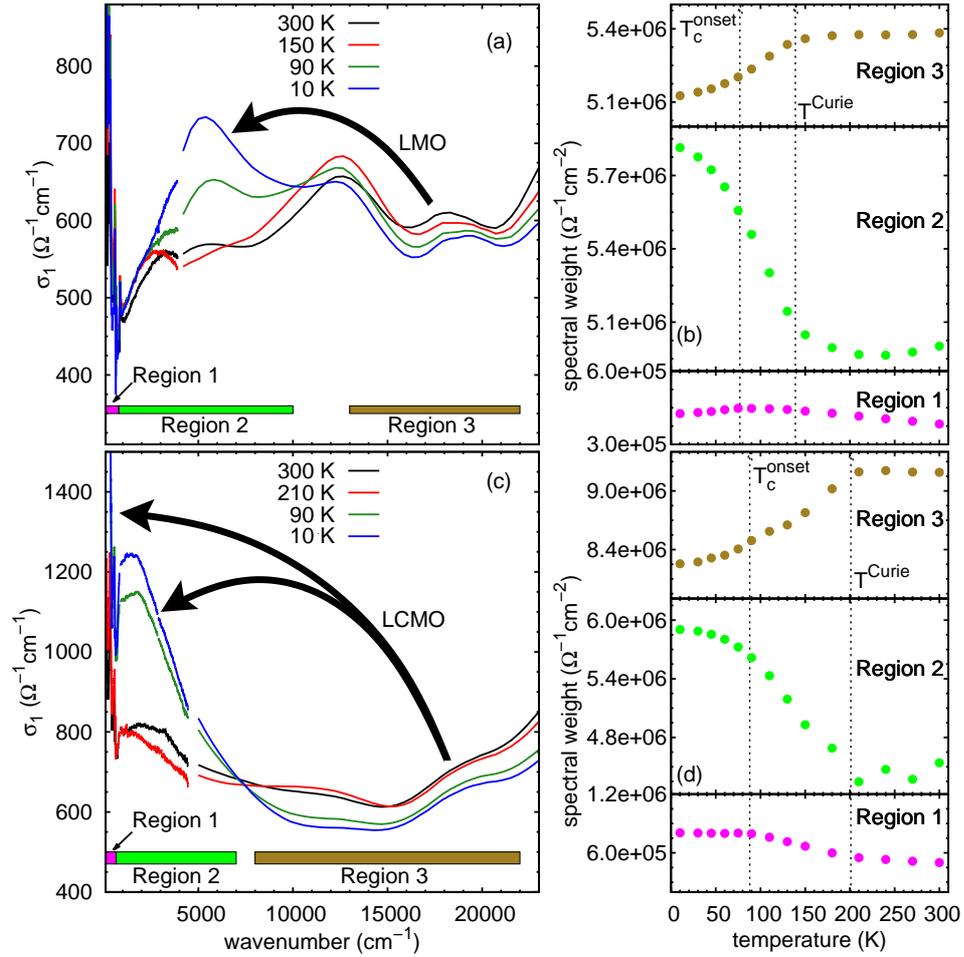
Figure 4.3: Panels (a) and (c): energy dependence of the real part of the conductivity for the YLCM and YLM superlattices, respectively, measured at different temperatures. Panels (b) and (c): corresponding evolution with temperature of the spectral weight for the three regions defined in (a) and (c). The figure has been taken from the supplemental online material of Ref. [109].

layers are hole doped with polaronic charge carriers that are strongly pinned and thus do not contribute to a coherent transport.

The ferromagnetic and insulating character of the LMO layers in sample YLM constitutes the main difference with respect to the sample YLCM for which the ferromagnetic LCMO layers are conducting below T^{Curie}. In the following sections the influence of the insulating behavior of the ferromagnetic layers on the phenomenology of the magnetic proximity effect is explored.

4.3. Polarized neutron reflectometry and the magnetic depth profile

The magnetic depth profile of the YLM superlattice has been studied with polarized neutron reflectometry (PNR). The suppression of the ferromagnetic order on the LMO side of the interface is found to be very weak for this system, the depleted layers are limited to the first monolayer at the interface.

The PNR measurements of this sample have been performed at the AMOR time-of-flight reflectometer located at the SINQ spallation source in the Paul Scherrer Institut in Villigen, Switzerland. The low temperature data have been collected after cooling the sample with an applied field of 1000 Oe. The results are summarized in Figure 4.4 where the reflectivity curves measured at 300, 100 and 22 K are shown. At room temperature the magnetic effects
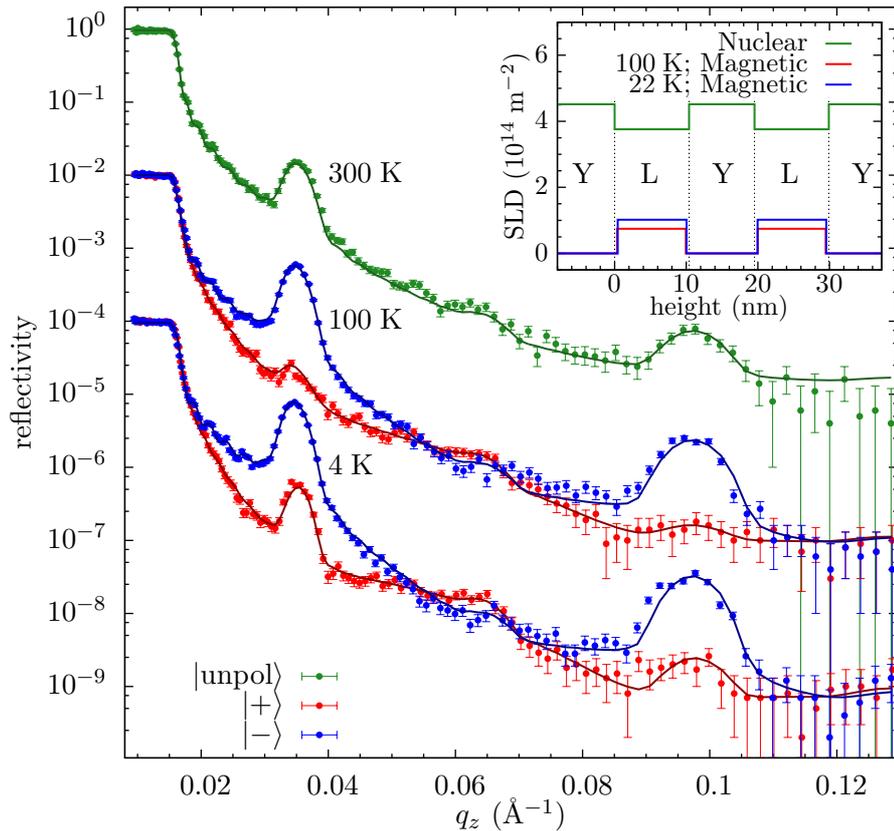
Figure 4.4: Polarized neutron reflectometry measurements performed on the YLM sample at different temperatures. At room temperature an unpolarized neutron beam has been used. The low temperature curves have been measured after cooling in a filed of 1000 Oe and for neutrons with spin parallel, $|+\rangle$, and antiparallel, $|-\rangle$, to the applied field. The curves are shifted vertically for clarity. The fitted reflectivities using Model 1 are represented by the solid lines and the corresponding structural and magnetic depth-profiles are shown in the inset.

are absent and an unpolarized neutron beam has been used. As discussed in section 2.2.4, in the time-of-flight mode the dispersion in q_z increases linearly with the momentum transfer and leads to the observed broadening of the higher order superlattice Bragg peaks (SLBPs) in the curves shown in the figure. This is thus an instrumental effect and should not be associated with an inhomogeneity of the sample.

As expected for an almost symmetric superlattice, the second order Bragg peak is strongly suppressed at room temperature. This suppression is, however, not complete which suggests that there is a small mismatch in the thickness of the YBCO and LCMO layers. The Kiessig fringes arising from the interference between the reflection coming from the substrate-film and film-surface interfaces can be observed in the region before the 1st SLBP. At low temperatures the shape of the reflectivity curve depends on the neutron spin orientation owing to the different sign of the magnetic contribution to the potential. In remarkable contrast to the YLCM sample, the 2nd order SLBP remains essentially absent at low temperature. This observation suggests that the neutron potential for this sample remains nearly symmetric even when the magnetic contribution becomes relevant.

To perform a quantitative analysis, the reflectivity curves have been fitted using the GenX software [74]. The room temperature data were fitted first to obtain the structural parameters of the superlattice. The fitted reflectivity is shown as a continuous line in Figure 4.4 and exhibits a good agreement with the measured data. The calculated structural parameters are presented in Table 4.1. As suggested by the sizable intensity of the 2nd order SLBP at room temperature, the LMO layers are approximately 13 Å thicker than the YBCO ones. In good agreement with the x-ray diffraction results, the calculated scattering length density of the

	ρ_n $(10^{-6}$ $\mathring{A}^{-2})$	d $(\mathring{A})$	σ $(\mathring{A})$
YBCO	4.56(5)	91(1)	6.7(6)
LMO	3.78(3)	104(1)	8.7(6)
LSAT	5.117	–	–

Table 4.1: Nuclear scattering length density (ρ_n), thickness (d) and roughness (σ) of the YBCO and LMO layers in the YLM superlattice as obtained from the fit of the room temperature neutron reflectometry. The given roughness corresponds to the top interface of the layer, in the growth direction. Also shown for reference is the substrate scattering length density which was not used as a fitting parameter but was calculated from the structural parameters reported in Ref. [106].

YBCO layers is, within the error bars, the same than the one calculated for the YLCM sample. A nominal value of the scattering length density of the LMO layers could not be calculated since the exact stoichiometry remains unknown. The fitted value is nevertheless slightly larger than the one calculated using the reported lattice parameters for undoped $LaMnO_3$, $\rho_n = 3.74 \times 10^{-6}$ $\mathring{A}^{-2}$ [128], and for cation-deficient $LaMnO_{3.16}$, $\rho_n = 3.645 \times 10^{-6}$ $\mathring{A}^{-2}$ [129], which is smaller given its reduced density. The enhancement of the scattering length density in the LMO layers can be attributed to the large compressive strain induced by the LSAT substrate. The density of Mn ions, which is needed to normalize the magnetization measurements, can be estimated by assuming an oxygen excess parameter $y = 0.125(15)$. It is in this range of oxygen doping that a ferromagnetic and insulating phase is observed in LMO. For this stoichiometry, the fitted value of the scattering length density of the LMO layers corresponds to a Mn ion density of $16.7(2)$ nm^{-3}, this value has been used in section 4.2.

The fitted values of the interface roughness of the YBCO and LMO layers in YLM are similar to the ones obtained for the YLCM superlattice which suggests that they have comparable interface properties. For both samples the roughness of the ferromagnetic layers is found to be slightly larger than for the superconducting ones. The obtained surface roughness of $16(1)$ $\mathring{A}$ is larger than for YLCM. The poorer quality of the surface may be due to a stronger degradation effect of the topmost LMO layer as a consequence of the direct contact with the atmosphere.

The low temperature PNR data have been fitted using the Model 1 introduced in section 3.3. This model incorporates the so-called depleted layers on the ferromagnetic side of the interface and was shown to properly describe the magnetic properties of the YLCM superlattice. The fitted reflectivity curves are presented as continuous lines in the Figure 4.4 and reproduce well all the features of the measured data. The remarkable agreement between the simulation and the observation testifies to the suitability of Model 1 to describe the magnetic depth profile in the YLM superlattice as well.

The fitted values of the thickness of the top and bottom depleted layers (with respect to the growth direction) are listed in Table 4.2, the corresponding structural and magnetic depth profiles are displayed in the inset of Figure 4.4. As initially suggested by the reduced intensity of the even order SLBP at low temperatures, the thickness of the depleted layers in the LMO layers is considerable smaller than for the LCMO layers in the YLCM sample. With a maximum value of 4.4 $\mathring{A}$, the suppression of the ferromagnetic moment in the LMO layers is essentially bound to the first monolayer at the interface. The thickness of the depleted layers is even smaller than the interface roughness, the observed suppression can thus also be associated to interface disorder effects. The magnetization inside the LMO layers is therefore almost homogeneous.

The PNR data also confirms that the topmost LMO layer is largely affected by the contact with the atmosphere. Indeed, for the fits shown in Figure 4.4 the topmost LMO layer has been treated separately and its calculated magnetization vanishes. A non-ferromagnetic topmost LMO layer must be introduced to account for the observed difference between the reflectivity curves for neutrons with spin parallel and antiparallel in the region before the 1st SLBP. This

T, H	$d_{\mathrm{dep}}^{\mathrm{bottom}}$ (Å)	$d_{\mathrm{dep}}^{\mathrm{top}}$ (Å)
22 K, 1000 Oe	4.3(7)	3.6(7)
100 K, 1000 Oe	3.3(7)	4.4(7)

Table 4.2: Thickness of the depleted layers in YLM at the bottom and top LMO interfaces as obtained with Model 1.

large splitting was not observed in the PNR data of sample YLCM for which the topmost LCMO layer remains ferromagnetic. Whether the topmost LMO layer is non-magnetic or it rather shows a weakly ferromagnetic or canted antiferromagnetic ordering is difficult to tell from these measurements.

The fitted values of the magnetization in the core of the LMO layers are 1.61(5) and 2.20 μ_{B}/Mn at 100 and 22 K, respectively. The corresponding magnetization of the sample, calculated by taking into account the depleted layers and the non-magnetic topmost LMO layer, is shown as red symbols in Figure 4.2. Their good agreement with the dc magnetization data confirms the applicability of Model 1 to accurately describe the magnetic depth profile of the sample.

Within the error bars, the thickness of the depleted layers does not change from 100 k to 22 K. Correspondingly, the asymmetry of the 3rd order SLBP does not show any significant evolution between these two temperatures. This observation confirms that the detected changes in the magnetic-depth profile of the YLCM sample below the superconducting critical temperature take place in the ferromagnetic LCMO layers. These changes cannot be associated with a diamagnetic contribution of the superconducting YBCO layers which would be common for both samples.

The observed difference in the suppression of the ferromagnetic moment on the LCMO or LMO side of the interface between the YLCM and YLM samples cannot be attributed to structural defects or an enhanced interface disorder. As shown by the x-ray diffraction data, the structural properties and strain condition of the YLCM and YLM samples are similar. The same trend is observed for the interface roughness as calculated from the PNR data. Since the main difference between these two samples concerns the conducting and insulating character of the LCMO and LMO layers, respectively, it appears that the strength of the magnetic proximity effect on the ferromagnetic side of the interface is governed by the electric properties of the ferromagnetic layers. The suppression of the ferromagnetic moment on the ferromagnetic side of the interface thus has an intrinsic origin.

4.4. Orbital reconstruction and magnetism of the Cu ions at the interface

The study of the electrical and magnetic properties of the Cu ions on the YBCO side of the interface by means of x-ray absorption spectroscopy is discussed in this section. The x-ray linear dichroism (XLD) measurements reveal that the orbital reconstruction takes place but is somewhat weaker than for the YLCM superlattice. The x-ray circular dichroism (XMCD) data show that although the Cu ions in the topmost YBCO/LMO interface are non-ferromagnetic, the inner interfaces show a net Cu ferromagnetic moment that is comparable to the one found in the YLCM sample.

The x-ray absorption measurements for linear and circular polarization on the YLM sample have been measured at the XTreme beamline of the Paul Scherrer Institut in Villigen Switzerland. The measurements were carried out using the total electron yield (TEY) and fluorescence yield (FY) modes with a sample temperature of 2 K and an angle of incidence of 30°.

The x-ray absorption for linearly polarized light provides the information about the orbital occupation of the probed Cu ions. To perform this study the absorption curves at the Cu-$L_{3,2}$ edge for σ and π polarized light have been measured twice each. The absorption for

	$\underline{P}_{e_g}$ (%)		w (%)	
	TEY	FY	TEY	FY
Peak 1	7(1)	20(6)	60(1)	9(1)
Peak 2	66(5)	59(2)	29(1)	57(2)
Peak 3	41(22)	10(7)	5(1)	15(1)
Peak 4	-40(23)	-34(9)	7(1)	19(1)

Table 4.3: Calculated values for the hole orbital polarization ($\underline{P}_{e_g}$) and spectral weight in the polarization-averaged absorption (w) for each of the contributions to the TEY and FY absorption spectra at the Cu-L_3 edge of sample YLM.

polarization along the ab-plane and along the c-axis have been calculated based on these measurements using the transformations given in (3.1). The data have been subsequently corrected for a linear background in the pre-edge region as described in chapter A of the appendix.

The resulting absorption curves and the x-ray linear dichroism, defined as $\mu_{ab} - \mu_c$, are shown in Figure 4.5. The displayed data have been normalized to the peak at the L_3 edge of the polarization-averaged absorption, $\overline{\mu} = (2\mu_{ab} + \mu_c)/3$, for comparison purposes. The results for the surface sensitive TEY mode and the bulk sensitive FY mode are displayed in panels (a) and (c) in the figure, respectively. For the FY mode, the expected large difference in the absorption for different polarization directions is observed. At the L_3 edge, the XLD signal amounts to 80% of the polarization-averaged intensity. As already discussed, the holes in the Cu ions located in the CuO_2 planes have a predominant in-plane character and the absorption is thus larger when the polarization is parallel to the planes [53, 54]. A shoulder in the high-energy side of the white-line is evidence of the Zhang-Rice singlets [118, 119]. In the TEY mode the white lines for out-of-plane polarization are more intense than for the FY mode and the intensity of the XLD signal is thus reduced by about one-half at both the L_3 and L_2 edges. This observation evidences that, like in the YLCM superlattice, an orbital reconstruction for the Cu ions at the interface takes place. In the TEY mode the shoulder corresponding to the Zhang-Rice singlets is largely reduced.

A quantitative analysis of the orbital occupation of the Cu ions has been performed using the multiplet fitting at the Cu-L_3 edge. The absorption curves have thus been reproduced using a set of Lorentzian functions and a sigmoid function to model the background. The results of this analysis are presented in panels (b) and (d) of Figure 4.5 for the TEY and FY measurement modes, respectively. In analogy to the results of the sample YLCM, the L_3 white line of YLM can be described in terms of four different contributions. The peak located around 931 eV has been assigned to the $d^9 \rightarrow \underline{c}d^{10}$ transition, this transition is more probable when the polarization is parallel to the planes owing to the strong in-plane character of the holes in the CuO_2 planes. The transitions located at 931.6 eV and 932.5 eV can be associated to the so-called Zhang-Rice singlets, which are located preferably in the CuO chains. The lowest energy peak, located around 930.4 eV has been assigned to the electronically modified Cu ions at the interface. The redshift of the peak can be assigned to a charge transfer at the interface or to a change in the crystal field [37, 120], in either case it evidences a change in the electronic environment of the Cu ions at the interface.

For each of the four contributions to the absorption, the spectral weight and the hole orbital polarization have been calculated using the expressions (3.4) and (3.2), respectively. The results of these calculations are listed in Table 4.3 where the peaks have been labeled from the lowest to the highest energy. In agreement with the sample YLCM, for YLM the main contribution in the FY mode corresponds to Peak 2 located at 931 eV. The weight of the Zhang-Rice contributions, identified as Peaks 3 and 4, is largely reduced in the TEY mode evidencing that they have a predominant chain character and that the CuO chains are missing at the interface. The weight of Peak 1, located at 930.4 eV, shows the largest change between the FY and TEY modes, in the former it is the smallest contribution while in the latter it
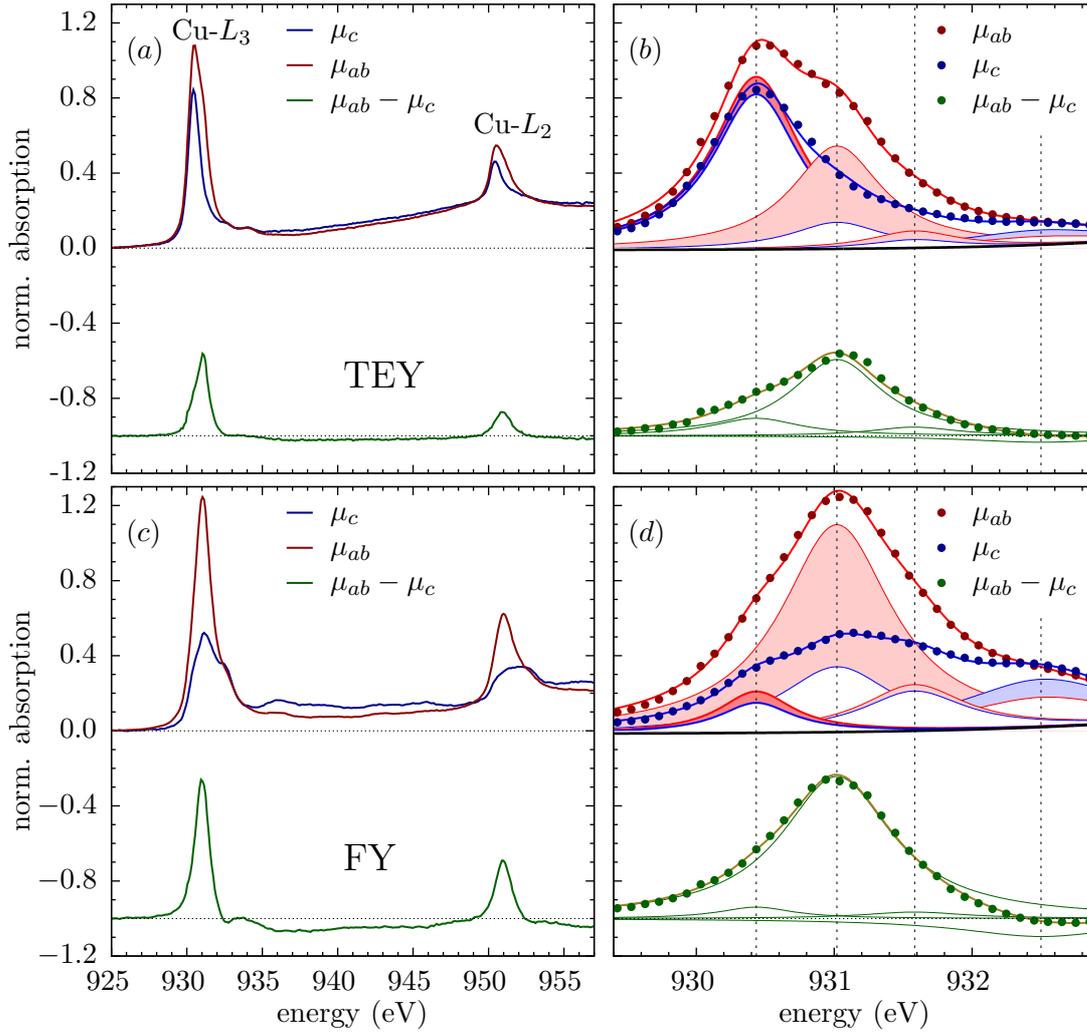
Figure 4.5: X-ray linear dichroism (XLD) results at the Cu-$L_{3,2}$ edge for sample YLM at 2 K. Panels (a) and (c) show the absorption curves for linear polarization along the planes, μ_{ab}, along the c-axis, μ_{ab}, and their difference. Panels (b) and (d) show the results of the multiplet fitting. The data are represented by dots and the fitted absorption by thick lines. The individual contributions to the absorption and the XLD are shown as thin lines, the shadowed areas highlight the XLD contribution of each peak. The dotted lines mark the position of the peaks.

is the largest. This observation confirms that this peak corresponds to transitions in the Cu ions next to the interface.

The orbital reconstruction of the Cu ions at the interface is confirmed by the large difference in the orbital polarization of Peaks 1 and 2. While for Peak 2 the orbital polarization is about 60%, the orbital polarization of Peak 1 is of only 7% in the TEY mode (the weight of the peak in the FY mode is smaller and the calculation of the orbital polarization in this mode is thus less reliable). For the Cu ions at the interface the occupation of the $3d_{x^2-y^2}$ orbital is thus almost as large as for the $3d_{3z^2-r^2}$ one. Nevertheless, the effect is weaker than for YLCM. For that sample the orbital polarization of the Cu ions at the interface is negative and a larger occupation is inferred for the $3d_{x^2-y^2}$ orbital. In terms of the covalent bonding model, the occupation of the in-plane and out-of plane orbitals in the electronically modified Cu ions at the interface depends on the energy difference between the $3d_{x^2-y^2}$ and the antibonding molecular orbitals [37]. The energy of the molecular orbital depends on the energy of the $3d_{3z^2-r^2}$ orbitals of both the Cu and Mn ions at the interface. For LMO the latter might be different than for LCMO and the size of the effect is thus modified.

On the other hand, the fraction of modified Cu ions seems to be larger for YLM than for YLCM. As discussed in section 3.4, the spectral weight of each peak in the FY polarization-

averaged absorption can be associated to the fraction of Cu ions where the transition takes place. For YLM the weight of the lowest energy peak in the FY mode is 9(1)%. This value is in close correspondence to the fraction of Cu ions that are at the interface. This fraction can be calculated using the obtained values of the YBCO c-axis lattice parameter and the YBCO layer thickness as 8.5%. Although the value of the spectral weight can be subjected to corrections due to the uncertainty in the background determination and the neglect of the finite spectral weight in the region above the white line, this analysis suggests that in the YLM sample the vast majority of the Cu ions at the interface are subjected to the orbital reconstruction. This is in contrast to the YLCM sample for which the weight of the lowest energy peak was calculated as 4.7%, corresponding to a 60% of the Cu ions at the interface. In terms of the covalent bonding model, the fraction of modified Cu ions at the interface depends on the probability to find the Cu-O-Mn bond and on the occupation of the $3d_{3z^2-y^2}$ orbital of the Mn ions at the interface. Either, or both, of these factors is thus larger for YLM than for YLCM. The probability to find the Cu-O-Mn bond could be enhanced if the CuO_2 termination of the YBCO layers is more homogeneous in the YLM superlattice. On the other hand, the compressive strain of the LMO layers grown on the LSAT substrate may lift the degeneracy of the e_g levels in favor of the occupation of the $3d_{3z^2-r^2}$ orbital [117]. To learn how these effects alter the fraction of modified Cu ions, the layer termination and the orbital occupation of the Mn ions should be studied with transmission electron microscopy and a combination of bulk and surface sensitive XLD measurements on the Mn-$L_{3,2}$ edge. The latter study is not possible in this case owing to the distortion of the FY signal at the Mn edge and to the fact that the TEY measurements are sensitive only to the topmost interface which is largely degraded.

The weight of the Zhang-Rice contributions to the absorption in the FY mode is smaller in the YLM than in the YLCM sample. On the other hand, for the YLM sample the weight of the 931 eV peak is larger. This weight transfer can be understood in terms of the oxygen deficiency and the corresponding reduced hole density in the YBCO layers in the YLM sample. Since the doped holes have mainly oxygen character their reduction leads to a reduction in the Zhang-Rice singlet density.

The magnetic properties of the Cu and Mn ions in the sample YLM have been studied by means of x-ray circular dichroism (XMCD) measurements. X-ray absorption curves for circularly polarized light with positive and negative helicity have thus been measured at the Cu and Mn $L_{3,2}$ edges with an applied field of ± 0.5 T after saturating the sample at ± 3 T. As already mentioned all the measurements have been performed at 2 K and with an incident angle of $30°$. To enhance the statistics, each absorption curve has been measured two and three times for each field direction at the Mn and Cu edges, respectively.

The measured absorption curves at the Cu-$L_{3,2}$ edge and the corresponding XMCD, defined as $\mu_+ - \mu_-$, are shown in panels (a) and (c) of Figure 4.6 for the TEY and FY modes, respectively. Apart from the pre-edge background correction, a normalization to the maximum at the L_3 edge of the polarization-averaged absorption has been applied. A small XMCD signal is observed for both the TEY and FY modes for which the XMCD intensity at the L_3 edge reaches about 2% of the averaged intensity. Its magnetic origin is confirmed by the sign change at the L_2 edge. As before, the Cu spin moment is antiparallel to the applied field as evidenced by the positive sign of the XMCD at the L_3 edge. While for the TEY mode the XMCD intensity is about five times smaller than the observed for the YLCM sample, the size of the XMCD signal in the FY mode is sizable and appears to have a similar size in both samples. Therefore, although the magnetic moment of the Cu ions next to the topmost YBCO/LMO interface appears to be largely reduced, a clear magnetization is suggested for the Cu ions at the inner interfaces.

The Cu spin magnetic moment can be calculated using the sum-rules in equations (3.5). The absorption curves have been corrected for the non-resonant contributions using the absorption baseline, μ_{bl}, shown in the panels (a) and (c) of Figure 4.6. As for YLCM, this baseline corresponds to the absorption curve for linear polarization along the ab planes and has been interpolated in the region of the white lines. This procedure has been chosen to ac-
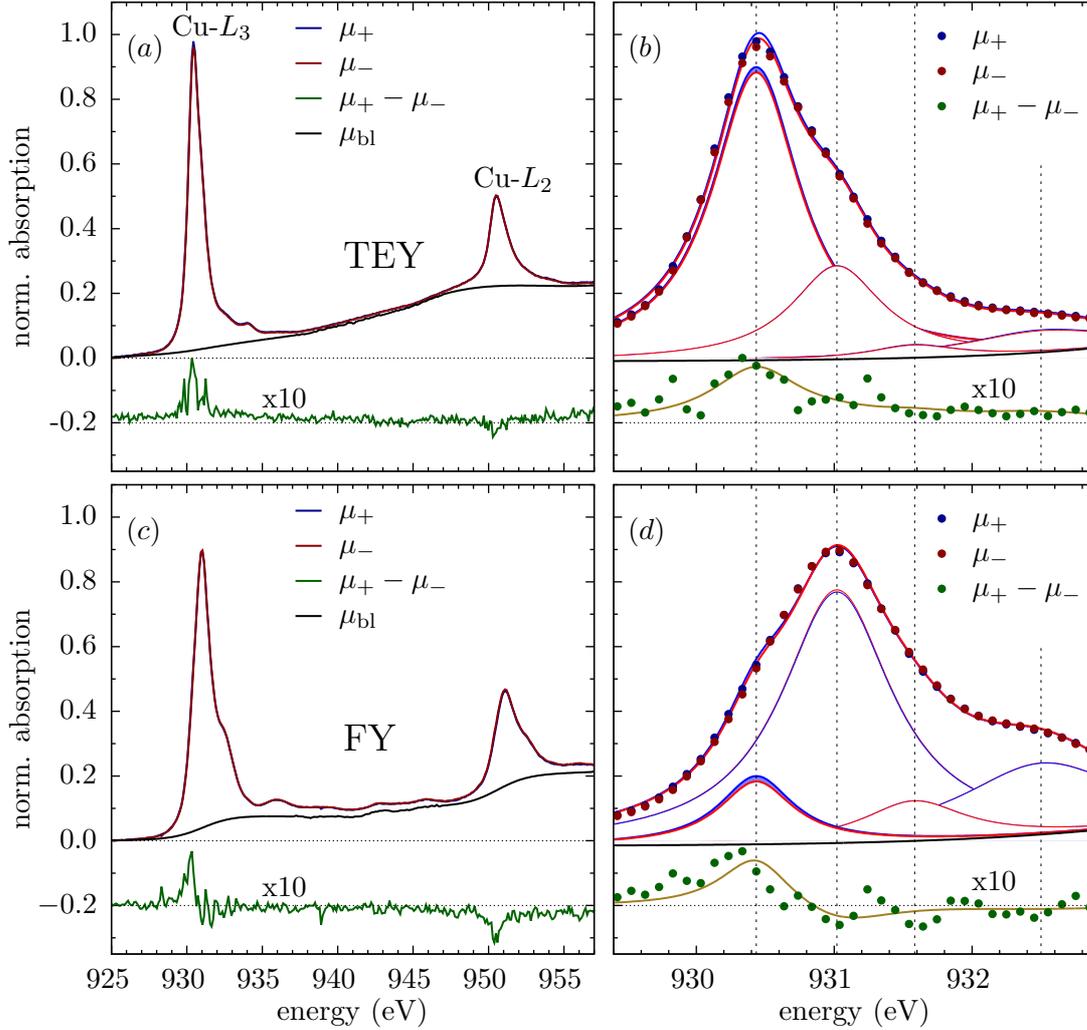
Figure 4.6: X-ray magnetic circular dichroism (XMCD) curves at the Cu-$L_{2,3}$ edge for sample YLM at 2 K. Panels (a) and (c) show the absorption curves for circular polarization with positive helicity, μ_+, negative helicity , μ_-, and their difference. The non-resonant absorption baseline, μ_{bl}, used in the sum rule calculations is also shown. Panels (b) and (d) show the results of the multiplet fitting. The data are represented by dots and the fitted absorption by thick lines. The individual contributions to the absorption and the XLD are shown as thin lines, the shadowed areas highlight the XMCD contribution of each peak. The dotted lines mark the position of the peaks.

count for the resonant contributions evidenced by a finite XLD in the regions above the white lines. The value of $\langle T_z \rangle$ has been estimated using equation 2.70 with an angle of incidence of 30° and a hole orbital polarization $\underline{P}_{e_g} = 7(1)\%$ for the Cu ions at the interface.

The resulting average spin magnetic moment in the TEY and FY modes is -0.011(5) μ_B/Cu and -0.013(5) μ_B/Cu, respectively. In agreement with the intensity of the XMCD signal the calculated moments in the TEY and FY modes are six times smaller and slightly larger, respectively, than the ones calculated for the YLCM sample. To learn about the origin of magnetism in the YLM sample, the multiplet fitting analysis has been performed to the absorption data for circularly polarized light. The fitting results are shown in panels (b) and (d) of Figure 4.6 and the good agreement with the data is evident. For both the TEY and FY modes, it becomes clear that the relevant contribution to the XMCD signal originates from the lowest energy peak, the one associated to the Cu ions at the interface. The direct link between the electronic reconstruction and the magnetism of the Cu ions at the interface is therefore confirmed in the YLM sample. In the FY mode, there is also a small magnetic component in the peak at 931 eV. These moments, which are parallel to the applied field, have also been observed in the sample YLCM and in other YBCO films and have been attributed
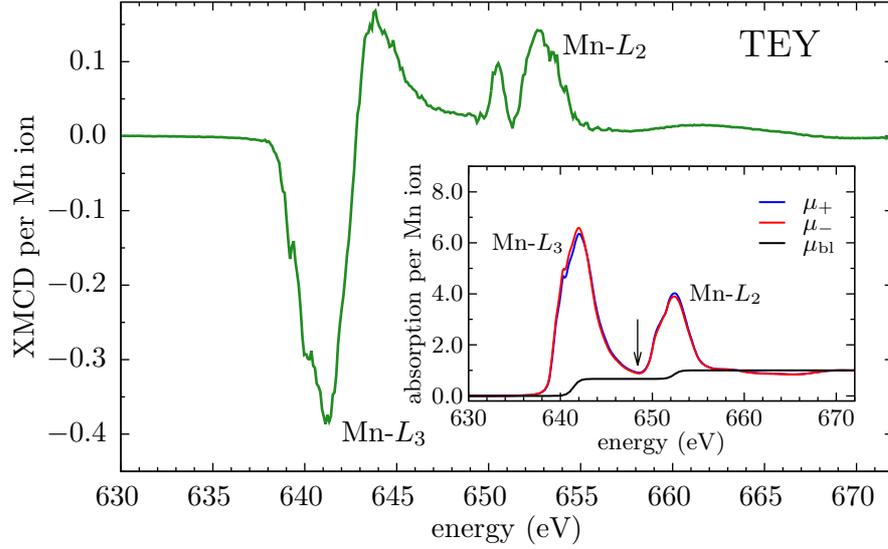
Figure 4.7: X-ray circular dichroism, defined as $\mu_+ - \mu_-$, at the Mn-$L_{3,2}$ edge of sample YLM at 2 K. The inset shows the absorption data which have been normalized to one after the edge.

to a paramagnetic contribution [123].

The ferromagnetic signal in Cu comes therefore exclusively from the ions next to the interface. The spin magnetic moment per electronically modified Cu ion at the interface can thus be calculated by normalizing the calculated moment to the weight of Peak 1 in the polarization-averaged absorption, which is shown in Table 4.3. This calculation yields $0.020(8)\,\mu_\mathrm{B}/\mathrm{Cu}$ and $0.16(6)\,\mu_\mathrm{B}/\mathrm{Cu}$ for the TEY and FY modes, respectively. The magnetization of the Cu ions in the topmost YBCO/LMO interface is therefore almost one order of magnitude smaller than the magnetization of the Cu ions averaged over all the interfaces. This large difference is related to the fact that the top LMO layer is non-ferromagnetic and is in good agreement with the conclusion that the Cu moment at the interface is induced by the Mn magnetic on the other side of the interface. The non-ferromagnetic character of the top LMO layer has been inferred from the PNR data and is also confirmed by the XMCD data at the Mn-$L_{3,2}$ edge shown in Figure 4.7. As seen in the figure, the XMCD signal is about six times smaller than the observed for the YLCM sample and, correspondingly, the magnetization of Mn in the top LMO layer is calculated as only $0.36(7)\,\mu_\mathrm{B}/\mathrm{Mn}$. To perform this calculation, an average valence of the Mn ions of $+3.25(3)$ has been used based on the oxygen excess parameter $y = 0.125(15)$ that is suggested from the transport and magnetization data.

The average magnetization for the Cu ions at the interface calculated from the FY data of $0.16(6)\,\mu_\mathrm{B}/\mathrm{Cu}$, yet subjected to a large uncertainty, is in good agreement with the magnetization for the Cu ions at the interface in the YLCM sample. As discussed in section 3.5, for that sample a magnetization of $0.18\,\mu_\mathrm{B}/\mathrm{Cu}$ was inferred from the TEY measurements. This observation evidences that the magnetic properties of the Cu ions at the interface are indeed similar for both systems and that they are not significantly affected by the electric properties of the ferromagnetic layers in the superlattice. According to the covalent bonding model the hole density in the $3d_{3z^2-r^2}$ orbital should modulate the magnetic moment of the Cu ions at the interface [37]. This dependence is nevertheless, not possible to establish from the measurements presented here owing to the large error bars of the calculations.

4.5.   Concluding remarks

The transport, magnetization and optics measurements performed on the superlattice YLM revealed that the LMO layers are ferromagnetic with a Curie temperature $T^{\mathrm{Curie}} \approx 135\,\mathrm{K}$ and that they remain insulating in the ferromagnetic phase. The localization of carriers

might be due to the formation of orbital and magnetic polarons. The YBCO layers are superconducting with an onset critical temperature $T_C \approx 77\,K$ and thus exhibit a slightly oxygen deficient phase.

The x-ray diffraction analysis showed that the structural properties of the YBCO layers do not differ significantly from the sample YLCM. The LMO layers, on the other hand, have a larger unit-cell than LCMO and are thus subjected to a larger compressive strain. This enhanced strain, however, does not lead to any appreciable lattice relaxation. The in-plane lattice parameters of the YBCO and LMO layers are therefore similar to the ones of the LSAT substrate.

The magnetic depth profile of the YLM superlattice has been studied with the polarized neutron reflectometry technique. While the interface roughness is similar to the one of the YLCM sample, the depleted layers are smaller and bound to the first LMO layer next to the interface. The strong reduction of the ferromagnetic moment observed in the YLCM sample, for which the ferromagnetic layers are conducting, is thus not present in this sample. Since the structural properties and the interface quality of both samples are similar, the difference in the strength of the suppression of the ferromagnetic correlations is related to the different electric properties of the magnetic layers. This dependence confirms the intrinsic origin of the magnetic proximity effect.

The x-ray linear dichroism studies on the sample revealed that for the Cu ions at the interface a redshift of the absorption peak and an orbital reconstruction take place. Yet smaller than for the YLCM sample, the changes in the orbital occupation for the Cu ions at the interface are large and an almost equal occupation is inferred for the in-plane and out-of-plane orbitals. The difference in the orbital occupation at the interface between the YLCM and YLM samples is probably related to the different orbital configuration of the Mn ions on the ferromagnetic side of the interface. The fraction of Cu ions at the interface that are electronically modified is, on the other hand, larger than for the YLCM sample. The origin of this difference needs to be further explored, it can be related to the termination of the YBCO layers or to the occupation of the $3d_{3z^2-r^2}$ orbitals of the Mn ions.

The x-ray circular dichroism measurements show the existence of a net magnetic moment for the modified Cu ions at the interface. The link between the orbital reconstruction and the magnetism of the Cu ions at the interface is thus confirmed. The Cu magnetic moment is antiparallel to the applied field. The quantitative analysis yields an average magnetic moment per modified Cu ion at the interface of $0.16(6)\,\mu_B$ which is comparable to the observed in YLCM. The magnetic proximity effect on the YBCO side of the interface is thus not significantly influenced by the electric transport properties of the magnetic layers.

Chapter 5

Conclusions and Outlook

The phenomenology of the magnetic proximity effect has been studied on almost symmetric $YBa_2Cu_3O_7/$ $La_{2/3}Ca_{1/3}MnO_3$ (YBCO/LCMO) and YBCO/$LaMnO_{3+y}$ (LMO) superlattices grown on LSAT substrates. For both samples the cuprate layers are superconducting with superconducting critical onset temperatures of $T_C \approx 88\,K$ and $77\,K$ for the YBCO/LCMO and YBCO/LMO respectively. The manganite layers are ferromagnetic with Curie temperatures, T^{Curie}, of about $200\,K$ for LCMO and $135\,K$ for LMO. The former exhibits a metal-to-insulator transition at T^{Curie} whereas the latter remains insulating in the ferromagnetic state. The structural properties of both samples are similar, the cuprate and manganite layers are strained and thus have in-plane lattice parameters that are very similar to the ones of the substrate. In both cases no evidence of a significant lattice relaxation has been found.

The neutron reflectometry curves measured at room temperature testify to the high structural quality of both superlattices. The strong suppression of the even order superlattice Bragg peaks (SLBPs) provides direct evidence for the similar thickness of the cuprate and manganite layers. The odd-order SLBP are pronounced and sharp. Correspondingly, the fitting of the reflectivity curves yields rather low values of the interface roughness of about $7\,\text{Å}$ for the cuprate and $9\,\text{Å}$ for the manganite layers in both samples.

The polarized neutron reflectometry (PNR) curves of the YBCO/LCMO superlattice measured in the ferromagnetic state below T^{Curie} yield intense even order SLBPs. This observation shows that there must be a large mismatch between the magnetic and the structural depth profiles in this sample. The magnetic depth profile has been determined by fitting the data to different models. The characteristic features of the data have been best described with a model that contains a so-called depleted layer on the LCMO side of the interface for which the net ferromagnetic moment of LCMO is strongly suppressed. The average thickness of these depleted layers in the LCMO bottom and top interfaces (in the growth direction) amounts to about 10 and $17\,\text{Å}$ respectively and is significantly larger than the interface roughness. This suggests that the strong reduction of the magnetization in the depleted layers has an intrinsic origin, rather than an extrinsic one related to structural or chemical disorder.

The magnetic depth profile shows an interesting temperature dependence. Notably, the temperature dependent asymmetry of the 3rd order SLBP is significantly enhanced below $90\,K$, i.e., in the vicinity of the superconducting critical temperature T_C. By simulating the reflectivity curves it has been shown that this changes are related to the enhancement of the magnetic properties of the depleted layers. This results will hopefully motivate additional studies, for example on superlattices with different values of T_C, to determine whether the changes in the magnetic depth profile of the LCMO layers are induced by the onset of superconductivity in the YBCO layers.

For the YBCO/LMO superlattice, on the other hand, the PNR curves below T^{Curie} do not show a significant increase in the intensity of the even order SLBP. The neutron potential thus remains nearly symmetric in the ferromagnetic state. Correspondingly, the depleted layers are found to be much smaller. With a maximal thickness of about $4\,\text{Å}$ they are bound to the first LMO monolayer at the interface. This clear difference between the YBCO/LCMO

and YBCO/LMO superlattices evidences that the size of the depleted layers depends on the electronic properties of the ferromagnetic layers. The intrinsic origin of the depleted layers is thus confirmed. For this sample no significant changes in the shape of the magnetic depth profile are observed at low temperature.

The x-ray absorption data at the Cu-$L_{3,2}$ edge confirm that the magnetic proximity effect additionally gives rise to a so-called orbital reconstruction and an induced ferromagnetic moment on the YBCO side of the interface. The orbital reconstruction is such that the occupancy of the in-plane and out-of-plane orbitals becomes comparable, in contrast to the large orbital polarization of bulk YBCO. For both the YBCO/LCMO and YBCO/LMO superlattices, the induced ferromagnetic Cu moment is antiparallel to the magnetization in the manganite layers. The temperature dependence and switching behavior of the Cu and Mn moments show that the former are induced by the latter. The x-ray resonant magnetic reflectometry results confirm that the magnetic Cu ions are located on the YBCO side of the interface and thus rule out the possibility of a chemical interdiffusion.

The quantitative analysis of the Cu-L_3 absorption spectra shows that both the magnetism and the orbital reconstruction arise exclusively from a fraction of Cu ions that are located at the interface and are subjected to a different electronic environment. The modified electronic environment for these ions is evidenced by a redshift of about $0.6\,\mathrm{eV}$ of their contribution to the absorption spectra. The direct link between the magnetism and the orbital reconstruction of Cu has thus been established for the first time. The spin magnetic moment per electronically modified Cu ion at the interface has been determined as $0.18(4)\,\mu_\mathrm{B}$ and $0.16(6)\,\mu_\mathrm{B}$ for the YBCO/LCMO and YBCO/LMO superlattices, respectively. Both superlattices also exhibit a comparable magnitude of the orbital reconstruction effect. The similar strength of these effects suggest that they do not significantly depend on the electronic transport properties of the ferromagnetic layers.

A sizable difference is nevertheless found in the fraction of the Cu ions at the interface that are affected by the magnetic proximity effect. While a fraction of 60% is estimated for YBCO/LCMO, a nearly 100% fraction is obtained for YBCO/LMO. Whether this difference has a structural or an intrinsic origin needs to be further explored.

The induction of a Cu moment and its coupling to the magnetic moment in the ferromagnetic layers confirms that the depleted layer cannot be regarded as non-magnetic. In spite of the strong suppression of the net magnetization in the depleted layers, the magnetic correlations evidently persist right to the interface. The depleted layers must therefore retain a canted antiferromagnetic or a non-collinear magnetic order with a reduced in-plane magnetization component.

The results presented in this thesis raise an important question regarding the origin of the depleted layers and their dependence on the electronic properties of the ferromagnetic layers. A deeper understanding of the magnetic proximity effect in YBCO/LCMO superlattices would allow the control of the magnetic properties at the interface in these systems clearing the way to new devices and applications. For example, a non-collinear magnetic layer at the interface between a superconductor and a ferromagnet is a prerequisite for the induction of spin-polarized supercurrents into the ferromagnet [3, 12]. The ability to control the thickness of such non-collinear magnetic layer would make the YBCO/LCMO system an ideal example to study the possibility to induce spin-triplet superconductivity in oxide-based superconductor/ferromagnet heterostructures.

Appendix A

Normalization and background subtraction of the x-ray absorption curves

The x-ray absorption coefficient of Cu and Mn ions has been determined with total electron yield (TEY) and fluorescence yield (FY) measurements. Neglecting saturation and self-absorption effects, the intensity of the fluorescence radiation and the current of the Auger electrons leaving the sample are both proportional to the absorption coefficient and allow for a quantitative data analysis [96, 98]. In TEY mode the absorption coefficient is thus determined by grounding the sample and measuring the charge flow to the sample as a function of the incident beam energy. Correspondingly, in FY mode the absorption is obtained by measuring the current in a photodiode as a function of the energy of the incoming x-rays.

To single out the resonant part of the absorption due to the Cu-$L_{2,3}$ or Mn-$L_{2,3}$ edges, it is necessary to subtract a background due to the non-resonant contributions of the other elements in the sample. In the following the procedure of this background subtraction is described for the example of the XMCD curves at the $L_{2,3}$-edge of Cu and Mn in sample YLCM performed at 2 K with an applied field of 0.5 T. The same procedure has been used for the analysis of all the XMCD and XLD curves that are shown in this work.

Figure A.1 illustrates the procedure for the intensity normalization and the background subtraction of the x-ray absorption curves for positive and negative helicity at the Cu-$L_{3,2}$ and Mn-$L_{3,2}$ edges of YLCM. Panels (a) and (d) show the raw data for a series of such XMCD measurements which have been performed at the Cu-$L_{3,2}$ edge with an applied field of 0.5 T at 2 K. For each polarization the measurement has been repeated three times. The TEY curves in panel (a) exhibit a noticeable intensity drift that is most likely caused by a weak charging effect of the sample. Panel (b) shows that this effect can be corrected by normalizing the intensity with respect to the average value in the pre-edge region. Panels (d) and (e) show the corresponding correction procedure for the FY data where the intensity drift is significantly smaller. After this normalization the curves match very well in the regions before and after the edges and can now be directly compared.

The next step involves the subtraction of the background that arises from the non-resonant absorption due to the other elements in the sample. In a first approximation, the contribution of these remote absorption edges has been approximated with a linear function. Panels (b) and (d) show the result of the linear fit to the data in the pre-edge region. The TEY and FY curves after the subtraction of this linear background are displayed in panels (c) and (f). For the FY curve in panel (f) this yields a satisfactory result. For the TEY curve in panel (c) it is evident that this linear background subtraction is not as accurate. This is due to the very low probe depth of the TEY mode and the circumstance that the YBCO layer is buried below the topmost LCMO one. The Cu signal is therefore not much stronger than the background which is dominated by some partially non-linear after-edge features of the strong La-$M_{5,4}$ absorption edge near 850 eV. For the sum-rule analysis of the spin and orbital moments an
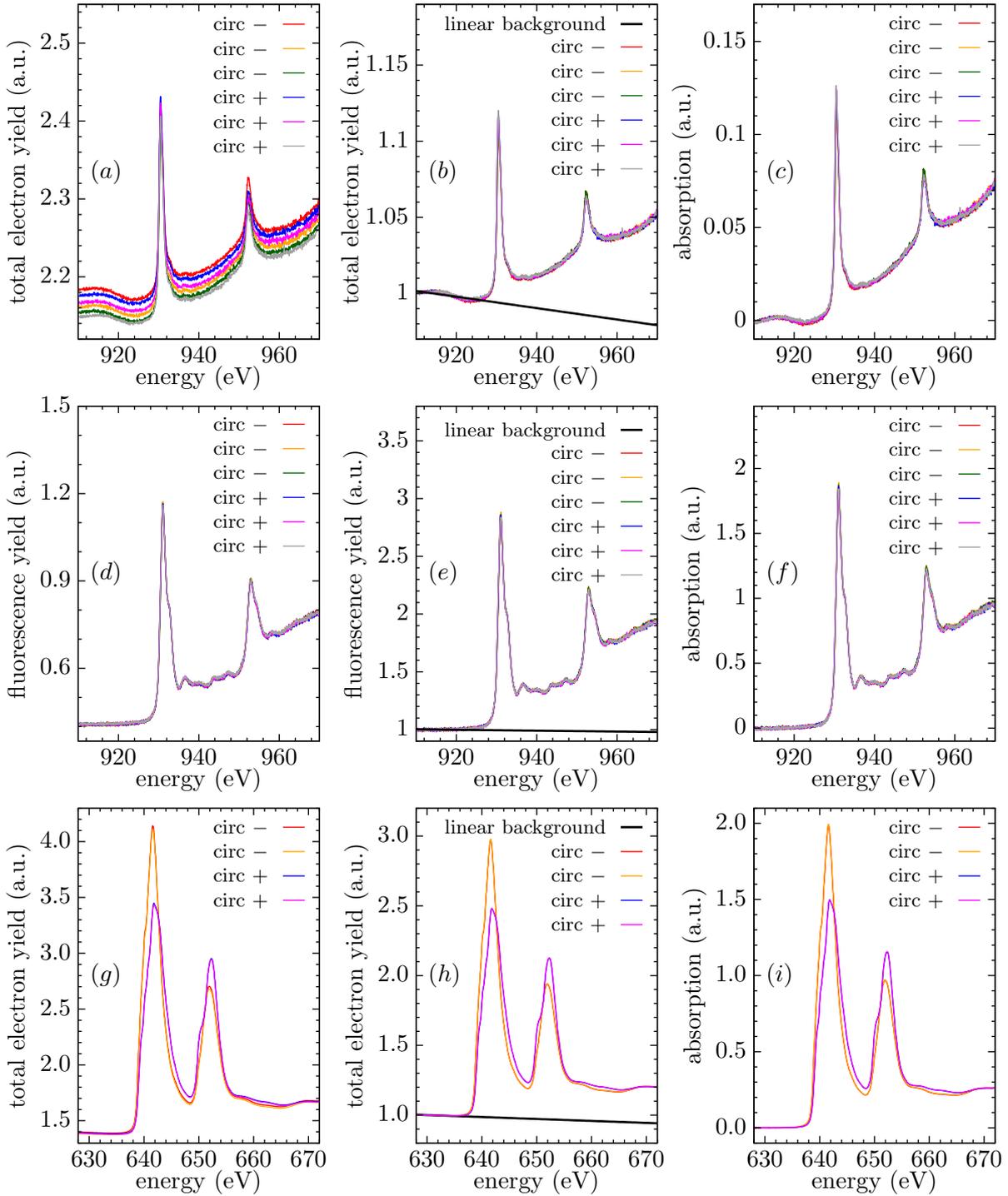
Figure A.1: Illustration of the procedure for the background subtraction to obtain the resonant absorption at the Cu and Mn-$L_{3,2}$ edges. The Cu $L_{3,2}$-edge results are shown in panels (a), (b) and (c) for the TEY mode and in panels (d), (e) and (f) for the FY mode. Panels (g), (h) and (i) show the results for Mn in the TEY mode. The raw data for a series of measurements performed using circular polarized light with positive and negative helicity at $2\,\mathrm{K}$ with an applied field $0.5\,\mathrm{T}$ are shown in panels (a), (d) and (g). Panels (b), (e) and (h) display the same data after the normalization with respect to the intensity in the pre-edge region. The black line shows the extrapolation of the linear fit of the pre-edge region that is used to account for the background absorption. Panels (c), (f) and (i) show the absorption at the Cu-$L_{3,2}$ and Mn-$L_{3,2}$ edges obtained after the subtraction of this linear background.

additional background subtraction has been performed as outlined in section 3.5.

Finally, for the Cu-$L_{3,2}$ edge FY and TEY curves shown in section 3.5, the absorption has been normalized with respect to the maximum of the polarization-averaged absorption at the L$_3$ edge. The μ_+ and μ_- curves represent the average of the absorption curves for helicity antiparallel and parallel to the applied magnetic field, respectively, as measured for positive and negative field directions. This reduces the noise level and helps to remove instrumental artifacts. It is worth mentioning that the XTreme beamline allows one to change the polarization state of the x-rays (via a modification of the undulator shift) without affecting the beam path to the sample and thus without modifying the offset or the dispersion of the energy scale [95].

For the Mn $L_{3,2}$-edge only the TEY data were suitable for a quantitative analysis. The FY data were heavily distorted due to strong self-absorption effects. Figure A.1(g) shows the raw data for a series of TEY measurements at the Mn-$L_{3,2}$ edge of YBCO/LCMO at 0.5 T and 2 K. In this case the absorption curves were measured twice for each polarization. Panel (b) shows that the small differences in the raw data can be readily corrected for by normalizing with respect to the averaged intensity of the pre-edge. In TEY mode the resonant Mn signal is much stronger than the background. The linear fit to the pre-edge region thus provides a good approximation of the background. This is seen in panel (c) where the Mn-$L_{3,2}$ absorption curves after the background subtraction are shown. In sections 3.4 and 3.5 the Mn absorption data have been normalized to one well after the edge to yield the absorption per Mn ion.

Acknowledgment

Curriculum Vitae

Personal Details

Name:	Uribe Laverde
First Name:	Miguel Angel
Date of birth:	June 25, 1984
Place of birth:	Bogotá, Colombia
Nationality:	Colombian

Studies

2010-2014:	PhD in Physics Physics Department University of Fribourg Fribourg, Switzerland
2006-2009:	MSc in Physics Departamento de Física Universidad Nacional de Colombia Bogotá, Colombia
2001-2006:	BSc in Physics Departamento de Física Universidad Nacional de Colombia Bogotá, Colombia

Languages

Spanish:	Native
English:	Advanced
French:	Intermadiate

Publications as First Author

X-ray absorption study of the electronic and magnetic proximity effects in $La_{2x}Sr_xCuO_4/$ $La_{2/3}Ca_{1/3}MnO_3$ multilayers
M.A. Uribe-Laverde, S. Das, K. Sen, I. Marozau, E. Peret, A. Alberca, J. Heidler, C. Piamonteze, M. Merz, P. Nagel, S. Schuppler, D. Munzar and C. Bernhard
To be submitted to Physical Review Letters.

Depth profile of the ferromagnetic order in a $YBa_2Cu_3O_7/La_{2/3}Ca_{1/3}MnO_3$ superlattice on a LSAT substrate: A polarized neutron reflectometry study
M. A. Uribe-Laverde, D. K. Satapathy, I. Marozau, V. K. Malik, S. Das, K. Sen, J. Stahn, A. Rühm, J.-H. Kim, T. Keller, A. Devishvili, B. P. Toperverg and C. Bernhard
Phys. Rev. B **87**, 115105 (2013)

Synthesis, structural characterization and fluctuation conductivity of $HoBa_2Cu_3O_{7-\delta}$-$SrTiO_3$ composites
M.A. Uribe Laverde, D.A. Landínez Téllez and J. Roa-Rojas
Physica C **470**, 5259 (2010).

Publications as Co-Author

Evidence for spin-triplet superconducting correlations in metal-oxide heterostructures with noncollinear magnetization
Yu. N. Khaydukov, G. A. Ovsyannikov, A. E. Sheyerman, K. Y. Constantinian, L. Mustafa, T. Keller, M. A. Uribe-Laverde, Yu. V. Kislinskii, A. V. Shadrin, A. Kalaboukhov, B. Keimer, and D. Winkler
Phys. Rev. B **90**, 035130 (2014).

Influence of La and Mn vacancies on the electronic and magnetic properties of $LaMnO_3$ thin films grown by pulsed laser deposition
I. Marozau, P.T. Das, M. Döbeli, J.G. Storey, M.A. Uribe-Laverde, S. Das, Ch. Wang, M. Rössle and C. Bernhard
Phys. Rev. B **89**, 174422 (2014).

Structural, magnetic, and superconducting properties of pulsed-laser-deposition-grown $La_{1.85}Sr_{0.15}CuO_4/La_{2/3}Ca_{1/3}MnO_3$ superlattices on (001)-oriented $LaSrAlO_4$ substrate
S. Das, K. Sen, I. Marozau, M. A. Uribe-Laverde, N. Biskup, M. Varela, Y. Khaydukov, O. Soltwedel, T. Keller, M. Döbeli, C. W. Schneider and C. Bernhard
Phys. Rev. B **89**, 094511 (2014).

High bias anomaly in $YBa_2Cu_3O_{7-x}/LaMnO_{3+\delta}/YBa_2Cu_3O_{7-x}$ superconductor/ferromagnetic insulator/superconductor junctions: Evidence for a long-range superconducting proximity effect through the conduction band of a ferromagnetic insulator
T. Golod, A. Rydh, V. M. Krasnov, I. Marozau, M. A. Uribe-Laverde, D. K. Satapathy, Th. Wagner and C.Bernhard
Phys. Rev. B **87**, 134520 (2013).

Magnetic proximity effect in $YBa_2Cu_3O_7/La_{2/3}Ca_{1/3}MnO_3$ and $YBa_2Cu_3O_7/LaMnO_{3+\delta}$ superlattices
D. K. Satapathy, M. A. Uribe-Laverde, I. Marozau, V. K. Malik, S. Das, Th. Wagner, C. Marcelot, J. Stahn, S. Brück, A. Rühm, S. Macke, T. Tietze, E. Goering, A. Frañó, J. -H. Kim, M. Wu, E. Benckiser, B. Keimer, A. Devishvili, B. P. Toperverg, M. Merz, P. Nagel, S. Schuppler and C. Bernhard
Phys. Rev. Lett. **108**, 197201 (2012).

Pulsed laser deposition growth of heteroepitaxial $YBa_2Cu_3O_7/La_{0.67}Ca_{0.33}MnO_3$ superlattices on $NdGaO_3$ and $Sr_{0.7}La_{0.3}Al_{0.65}Ta_{0.35}O_3$ substrates
V. K. Malik, I. Marozau, S. Das, B. Doggett, D. K. Satapathy, M. A. Uribe-Laverde, N. Biskup, M. Varela, C. W. Schneider, C. Marcelot, J. Stahn and C. Bernhard
Phys. Rev. B **85**, 054514 (2012).

Conductivity fluctuation and superconducting parameters of the $YBa_2Cu_{3-x}(PO_4)_xO_{7-\delta}$ material

M.P. Rojas Sarmiento, M.A. Uribe Laverde, E. Vera López. D.A. Landínez Téllez and J. RoaRojas

Bibliography

[1] L. Bulaevskii, A. Buzdin, M. Kuli and S. Panjukov. Adv. Phys. **34**, 175 (1985).

[2] A. I. Buzdin. Rev. Mod. Phys. **77**, 935 (2005).

[3] F. S. Bergeret, A. F. Volkov and K. B. Efetov. Rev. Mod. Phys. **77**, 1321 (2005).

[4] A. I. Buzdin and A. S. Mel'nikov. Phys. Rev. B **67**, 020503 (2003).

[5] J. Kehrle, V. Zdravkov, G. Obermeier, J. Garcia-Garcia, A. Ullrich, C. Müller, R. Morari, A. Sidorenko, S. Horn, L. Tagirov and R. Tidecks. Ann. Phys. (Berlin) **524**, 37 (2012).

[6] A. F. Volkov, F. S. Bergeret and K. B. Efetov. Phys. Rev. Lett. **90**, 117006 (2003).

[7] T. Kontos, M. Aprili, J. Lesueur, F. Genêt, B. Stephanidis and R. Boursier. Phys. Rev. Lett. **89**, 137007 (2002).

[8] Y. Blum, A. Tsukernik, M. Karpovski and A. Palevski. Phys. Rev. Lett. **89**, 187004 (2002).

[9] T. S. Khaire, M. A. Khasawneh, W. P. Pratt and N. O. Birge. Phys. Rev. Lett. **104**, 137002 (2010).

[10] J. W. A. Robinson, J. D. S. Witt and M. G. Blamire. Science **329**, 59 (2010).

[11] Z. Yang, M. Lange, A. Volodin, R. Szymczak and V. V. Moshchalkov. Nat. Mater. **3**, 793 (2004).

[12] M. Eschrig. Phys. Today **64**, 43 (2011).

[13] N. G. Pugach and A. I. Buzdin. Appl. Phys. Lett. **101**, 242602 (2012).

[14] J. G. Bednorz and K. A. Müller. Z. Phys. B: Condens. Matter **64**, 189 (1986).

[15] A. Schilling, M. Cantoni, J. D. Guo and H. R. Ott. Nature **363**, 56 (1993).

[16] R. von Helmolt, J. Wecker, B. Holzapfel, L. Schultz and K. Samwer. Phys. Rev. Lett. **71**, 2331 (1993).

[17] Y. Tokura and Y. Tomioka. J. Magn.Magn. Mat. **200**, 1 (1999).

[18] E. Dagotto, T. Hotta and A. Moreo. Phys. Rep. **344**, 1 (2001).

[19] P. Przyslupski, S. Kolesnik, E. Dynowska, T. Skoskiewicz and M. Sawicki. IEEE T. Appl. Supercon. **7**, 2192 (1997).

[20] A. Goldman, P. Kraus, K. Nikolaev, V. Vas'ko, A. Bhattacharya and W. Cooley. J. Supercond. **14**, 283 (2001).

[21] H.-U. Habermeier, G. Cristiani, R. Kremer, O. Lebedev and G. van Tendeloo. Physica C **364-365**, 298 (2001).

[22] Z. Sefrioui, D. Arias, V. Peña, J. E. Villegas, M. Varela, P. Prieto, C. León, J. L. Martinez and J. Santamaria. Phys. Rev. B **67**, 214511 (2003).

[23] T. Holden, H.-U. Habermeier, G. Cristiani, A. Golnik, A. Boris, A. Pimenov, J. Humlíček, O. I. Lebedev, G. Van Tendeloo, B. Keimer and C. Bernhard. Phys. Rev. B **69**, 064505 (2004).

[24] R. Werner, C. Raisch, A. Ruosi, B. A. Davidson, P. Nagel, M. Merz, S. Schuppler, M. Glaser, J. Fujii, T. Chassé, R. Kleiner and D. Koelle. Phys. Rev. B **82**, 224509 (2010).

[25] V. K. Malik, I. Marozau, S. Das, B. Doggett, D. K. Satapathy, M. A. Uribe-Laverde, N. Biskup, M. Varela, C. W. Schneider, C. Marcelot, J. Stahn and C. Bernhard. Phys. Rev. B **85**, 054514 (2012).

[26] V. Peña, Z. Sefrioui, D. Arias, C. Leon, J. Santamaria, J. L. Martinez, S. G. E. te Velthuis and A. Hoffmann. Phys. Rev. Lett. **94**, 057002 (2005).

[27] N. M. Nemes, M. García Hernández, S. G. E. te Velthuis, A. Hoffmann, C. Visani, J. Garcia-Barriocanal, V. Peña, D. Arias, Z. Sefrioui, C. Leon and J. Santamaría. Phys. Rev. B **78**, 094515 (2008).

[28] K. Dybko, K. Werner-Malento, M. Sawicki and P. Przyslupski. EPL (Europhysics Letters) **85**, 57010 (2009).

[29] J. Hoppler, J. Stahn, C. Niedermayer, V. K. Malik, H. Bouyanfif, A. J. Drew, M. Rossle, A. Buzdin, G. Cristiani, H.-U. Habermeier, B. Keimer and C. Bernhard. Nat. Mater. **8**, 315 (2009).

[30] J. Stahn, J. Chakhalian, C. Niedermayer, J. Hoppler, T. Gutberlet, J. Voigt, F. Treubel, H.-U. Habermeier, G. Cristiani, B. Keimer and C. Bernhard. Phys. Rev. B **71**, 140509 (2005).

[31] A. Hoffmann, S. G. E. te Velthuis, Z. Sefrioui, J. Santamaría, M. R. Fitzsimmons, S. Park and M. Varela. Phys. Rev. B **72**, 140407 (2005).

[32] S. Brück, S. Treiber, S. Macke, P. Audehm, G. Christiani, S. Soltan, H.-U. Habermeier, E. Goering and J. Albrecht. New J. Phys. **13**, 033023 (2011).

[33] W. Luo, S. J. Pennycook and S. T. Pantelides. Phys. Rev. Lett. **101**, 247204 (2008).

[34] J. Chakhalian, J. W. Freeland, G. Srajer, J. Strempfer, G. Khaliullin, J. C. Cezar, T. Charlton, R. Dalgliesh, C. Bernhard, G. Cristiani, H.-U. Habermeier and B. Keimer. Nat. Phys. **2**, 244 (2006).

[35] J. Liu, B. J. Kirby, B. Gray, M. Kareev, H.-U. Habermeier, G. Cristiani, J. W. Freeland and J. Chakhalian. Phys. Rev. B **84**, 092506 (2011).

[36] J. Salafranca and S. Okamoto. Phys. Rev. Lett. **105**, 256804 (2010).

[37] J. Chakhalian, J. W. Freeland, H.-U. Habermeier, G. Cristiani, G. Khaliullin, M. van Veenendaal and B. Keimer. Science **318**, 1114 (2007).

[38] K. Chahara, T. Ohno, M. Kasai and Y. Kozono. Appl. Phys. Lett. **63**, 1990 (1993).

[39] M. B. Salamon and M. Jaime. Rev. Mod. Phys. **73**, 583 (2001).

[40] J. Töpfer and J. Goodenough. J. Solid State Chem. **130**, 117 (1997).

[41] J. Geck, P. Wochner, S. Kiele, R. Klingeler, A. Revcolevschi, M. v Zimmermann, B. Büchner and P. Reutler. New J. Phys. **6**, 152 (2004).

[42] R. Kilian and G. Khaliullin. Phys. Rev. B **60**, 13458 (1999).

[43] R. J. Cava, R. B. van Dover, B. Batlogg and E. A. Rietman. Phys. Rev. Lett. **58**, 408 (1987).

[44] H. Takagi, S.-i. Uchida, K. Kitazawa and S. Tanaka. Jpn. J. Appl. Phys. **26**, L123 (1987).

[45] C. W. Chu, P. H. Hor, R. L. Meng, L. Gao and Z. J. Huang. Science **235**, 567 (1987).

[46] C. W. Chu, P. H. Hor, R. L. Meng, L. Gao, Z. J. Huang and Y. Q. Wang. Phys. Rev. Lett. **58**, 405 (1987).

[47] M. K. Wu, J. R. Ashburn, C. J. Torng, P. H. Hor, R. L. Meng, L. Gao, Z. J. Huang, Y. Q. Wang and C. W. Chu. Phys. Rev. Lett. **58**, 908 (1987).

[48] R. J. Cava, B. Batlogg, R. B. van Dover, D. W. Murphy, S. Sunshine, T. Siegrist, J. P. Remeika, E. A. Rietman, S. Zahurak and G. P. Espinosa. Phys. Rev. Lett. **58**, 1676 (1987).

[49] J. J. Capponi, C. Chaillout, A. W. Hewat, P. Lejay, M. Marezio, N. Nguyen, B. Raveau, J. L. Soubeyroux, J. L. Tholence and R. Tournier. EPL (Europhysics Letters) **3**, 1301 (1987).

[50] R. Liang, D. A. Bonn and W. N. Hardy. Phys. Rev. B **73**, 180505 (2006).

[51] J. D. Jorgensen, B. W. Veal, A. P. Paulikas, L. J. Nowicki, G. W. Crabtree, H. Claus and W. K. Kwok. Phys. Rev. B **41**, 1863 (1990).

[52] A. Lombardi, M. Mali, J. Roos and D. Brinkmann. Phys. Rev. B **53**, 14268 (1996).

[53] N. Nücker, E. Pellegrin, P. Schweiss, J. Fink, S. L. Molodtsov, C. T. Simmons, G. Kaindl, W. Frentrup, A. Erb and G. Müller-Vogt. Phys. Rev. B **51**, 8529 (1995).

[54] J. Fink, N. Nücker, E. Pellegrin, H. Romberg, M. Alexander and M. Knupfer. J. Electron. Spectrosc. Relat. Phenom. **66**, 395 (1994).

[55] P. W. Anderson. Science **235**, 1196 (1987).

[56] C. Bernhard, J. L. Tallon, T. Blasius, A. Golnik and C. Niedermayer. Phys. Rev. Lett. **86**, 1614 (2001).

[57] A. Shekhter, B. J. Ramshaw, R. Liang, W. N. Hardy, D. A. Bonn, F. F. Balakirev, R. D. McDonald, J. B. Betts, S. C. Riggs and A. Migliori. Nature **498**, 7577 (2013).

[58] H. Alloul, F. Rullier-Albenque, B. Vignolle, D. Colson and A. Forget. EPL (Europhysics Letters) **91**, 37005 (2010).

[59] N. E. Hussey. J. Phys.: Condens. Matter **20**, 123201 (2008).

[60] S. Sachdev. Science **288**, 475 (2000).

[61] S. Yunoki, A. Moreo, E. Dagotto, S. Okamoto, S. S. Kancharla and A. Fujimori. Phys. Rev. B **76**, 064532 (2007).

[62] S. R. Giblin, J. W. Taylor, J. A. Duffy, M. W. Butchers, C. Utfeld, S. B. Dugdale, T. Nakamura, C. Visani and J. Santamaria. Phys. Rev. Lett. **109**, 137005 (2012).

[63] J. Hoppler, J. Stahn, H. Bouyanfif, V. K. Malik, B. D. Patterson, P. R. Willmott, G. Cristiani, H.-U. Habermeier and C. Bernhard. Phys. Rev. B **78**, 134111 (2008).

[64]   X.-L. Zhou and S.-H. Chen. Phys. Rep. **257**, 223 (1995).

[65]   C. Fermon, F. Ott and A. Menelle. Neutron reflectometry. In J. Daillant and A. Gibaud, editors, *X-ray and Neutron Reflectivity*, volume 770 of *Lecture Notes in Physics*, pages 183–234. Springer Berlin Heidelberg (2009).

[66]   V. F. Sears. Neutron News **3**, 26 (1992).

[67]   H. Zabel, K. Theis-Bröhl and B. P. Toperverg. *Polarized Neutron Reflectivity and Scattering from Magnetic Nanostructures and Spintronic Materials.* John Wiley & Sons, Ltd (2007).

[68]   L. G. Parratt. Phys. Rev. **95**, 359 (1954).

[69]   J. Hoppler. *Magnetic induction in high-T_C superconductor/ferromagnet heterostructures.* PhD thesis, University of Fribourg (2009).

[70]   A. Rühm, B. P. Toperverg and H. Dosch. Phys. Rev. B **60**, 16073 (1999).

[71]   A. Gibaud and G. Vignaud. Specular reflectivity from smooth and rough surfaces. In J. Daillant and A. Gibaud, editors, *X-ray and Neutron Reflectivity*, volume 770 of *Lecture Notes in Physics*, pages 85–131. Springer Berlin Heidelberg (2009).

[72]   H. Zabel and K. Theis-Bröhl. J. Phys.: Condens. Matter **15**, S505 (2003).

[73]   SUPERFIT: Polarized Neutron Reflectivity Tool (Max-Planck Institute for Intelligent Systems, Stuttgart).

[74]   M. Björck and G. Andersson. J. Appl. Crystallogr. **40**, 1174 (2007).

[75]   M. Blume. J. Appl. Phys. **57**, 3615 (1985).

[76]   F. de Groot and A. Kotani. *Core Level Spectroscopy of Solids.* CRC press (2008).

[77]   J. Stöhr. J. Electron. Spectrosc. Relat. Phenom. **75**, 253 (1995).

[78]   J. Als-Nielsen and D. McMorrow. *Elements of modern x-ray physics.* Wiley, New York, NY, 2nd edition (2011).

[79]   L. Baumgarten. X-ray absorption spectroscopy. In M. Angst, T. Brückel, D. Richter and R. Zorn, editors, *Scattering Methods for Condensed Matter Research: Towards Novel Applications at Future Sources.* Forschungszentrum Jülich GmbH, JCNS, PGI, ICS, IAS Jülich (2012).

[80]   A. Nilsson and N. Mårtensson. Physica B **208-209**, 19 (1995).

[81]   M. D. Núñez Regueiro, M. Altarelli and C. T. Chen. Phys. Rev. B **51**, 629 (1995).

[82]   J. Stöhr and H. König. Phys. Rev. Lett. **75**, 3748 (1995).

[83]   J. Stöhr. J. Magn. Magn. Mater. **200**, 470 (1999).

[84]   B. T. Thole, G. van der Laan and G. A. Sawatzky. Phys. Rev. Lett. **55**, 2086 (1985).

[85]   G. van der Laan, B. T. Thole, G. A. Sawatzky, J. B. Goedkoop, J. C. Fuggle, J.-M. Esteva, R. Karnatak, J. P. Remeika and H. A. Dabkowska. Phys. Rev. B **34**, 6529 (1986).

[86]   C. Piamonteze, P. Miedema and F. M. F. de Groot. Phys. Rev. B **80**, 184410 (2009).

[87]   C. T. Chen, Y. U. Idzerda, H.-J. Lin, N. V. Smith, G. Meigs, E. Chaban, G. H. Ho, E. Pellegrin and F. Sette. Phys. Rev. Lett. **75**, 152 (1995).

[88] G. Schütz, W. Wagner, W. Wilhelm, P. Kienle, R. Zeller, R. Frahm and G. Materlik. Phys. Rev. Lett. **58**, 737 (1987).

[89] E. Goering, S. Gold and A. Bayer. Appl. Phys. A **78**, 855 (2004).

[90] J. P. Crocombette, B. T. Thole and F. Jollet. J. Phys.: Condens. Matter **8**, 4095 (1996).

[91] B. T. Thole, P. Carra, F. Sette and G. van der Laan. Phys. Rev. Lett. **68**, 1943 (1992).

[92] P. Carra, B. T. Thole, M. Altarelli and X. Wang. Phys. Rev. Lett. **70**, 694 (1993).

[93] Y. Teramura, A. Tanaka and T. Jo. J. Phys. Soc. Jpn. **65**, 1053 (1996).

[94] T. Oguchi and T. Shishidou. Phys. Rev. B **70**, 024412 (2004).

[95] C. Piamonteze, U. Flechsig, S. Rusponi, J. Dreiser, J. Heidler, M. Schmidt, R. Wetter, M. Calvi, T. Schmidt, H. Pruchova, J. Krempasky, C. Quitmann, H. Brune and F. Nolting. J. Synchrotron Radiat. **19**, 661 (2012).

[96] R. Nakajima, J. Stöhr and Y. U. Idzerda. Phys. Rev. B **59**, 6421 (1999).

[97] W. L. O'Brien and B. P. Tonner. Phys. Rev. B **50**, 12672 (1994).

[98] L. Tröger, D. Arvanitis, K. Baberschke, H. Michaelis, U. Grimm and E. Zschech. Phys. Rev. B **46**, 3283 (1992).

[99] G. J. H. M. Rijnders, G. Koster, D. H. A. Blank and H. Rogalla. Appl. Phys. Lett. **70**, 1888 (1997).

[100] J. Blasco, J. García, J. M. de Teresa, M. R. Ibarra, P. A. Algarabel and C. Marquina. J. Phys.: Condens. Matter **8**, 7427 (1996).

[101] E. O. Wollan and W. C. Koehler. Phys. Rev. **100**, 545 (1955).

[102] J. M. D. Coey, M. Viret and S. von Molnár. Adv. Phys. **48**, 167 (1999).

[103] H. Ju and H. Sohn. J. Magn. Magn. Mater. **167**, 200 (1997).

[104] N. Moutis, C. Christides, I. Panagiotopoulos and D. Niarchos. Phys. Rev. B **64**, 094429 (2001).

[105] J. F. Ding, Y. F. Tian, W. J. Hu, W. N. Lin and T. Wu. Appl. Phys. Lett. **102**, (2013).

[106] D. A. Pawlak, M. Ito, L. Dobrzycki, K. Wozniak, M. Oku, K. Shimamura and T. Fukuda. J. Mater. Res. **20**, 3329 (2005).

[107] J. Hoppler, H. Fritzsche, V. K. Malik, J. Stahn, G. Cristiani, H.-U. Habermeier, M. Rössle, J. Honolka, A. Enders and C. Bernhard. Phys. Rev. B **82**, 174439 (2010).

[108] M. A. Uribe-Laverde, D. K. Satapathy, I. Marozau, V. K. Malik, S. Das, K. Sen, J. Stahn, A. Rühm, J.-H. Kim, T. Keller, A. Devishvili, B. P. Toperverg and C. Bernhard. Phys. Rev. B **87**, 115105 (2013).

[109] D. K. Satapathy, M. A. Uribe-Laverde, I. Marozau, V. K. Malik, S. Das, T. Wagner, C. Marcelot, J. Stahn, S. Brück, A. Rühm, S. Macke, T. Tietze, E. Goering, A. Frañó, J. H. Kim, M. Wu, E. Benckiser, B. Keimer, A. Devishvili, B. P. Toperverg, M. Merz, P. Nagel, S. Schuppler and C. Bernhard. Phys. Rev. Lett. **108**, 197201 (2012).

[110] M. Varela, A. R. Lupini, S. J. Pennycook, Z. Sefrioui and J. Santamaria. Solid-State Electron. **47**, 2245 (2003).

[111] T. K. Worthington, W. J. Gallagher and T. R. Dinger. Phys. Rev. Lett. **59**, 1160 (1987).

[112] W. J. Gallagher. J. Appl. Phys. **63**, 4216 (1988).

[113] M. Abbate, F. M. F. de Groot, J. C. Fuggle, A. Fujimori, O. Strebel, F. Lopez, M. Domke, G. Kaindl, G. A. Sawatzky, M. Takano, Y. Takeda, H. Eisaki and S. Uchida. Phys. Rev. B **46**, 4511 (1992).

[114] K. B. Garg, N. L. Saini, B. R. Sekhar, R. K. Singhal, B. Doyle, S. Nannarone, F. Bondino, E. Magnano, E. Carleschi and T. Chatterji. J. Phys.: Condens. Matter **20**, 055215 (2008).

[115] A. J. Achkar, T. Z. Regier, H. Wadati, Y.-J. Kim, H. Zhang and D. G. Hawthorn. Phys. Rev. B **83**, 081106 (2011).

[116] F. M. F. de Groot. Nat. Chem. **4**, 766 (2012).

[117] D. Pesquera, G. Herranz, A. Barla, E. Pellegrin, F. Bondino, E. Magnano, F. Sánchez and J. Fontcuberta. Nat. Commun. **3**, 1189 (2012).

[118] D. Meyers, S. Mukherjee, J.-G. Cheng, S. Middey, J.-S. Zhou, J. B. Goodenough, B. A. Gray, J. W. Freeland, T. Saha-Dasgupta and J. Chakhalian. Sci. Rep. **3**, 1834 (2013).

[119] F. C. Zhang and T. M. Rice. Phys. Rev. B **37**, 3759 (1988).

[120] G. van der Laan, R. Pattrick, C. Henderson and D. Vaughan. J. Phys. Chem. Solids **53**, 1185 (1992).

[121] A. Ruosi, C. Raisch, A. Verna, R. Werner, A. Davidson, B. J. Fujii, R. Kleiner and D. Koelle (2013), arXiv:1310.5998 [cond-mat.mtrl-sci].

[122] M. A. Hossain, M. H. Burkhardt, S. Sarkar, H. Ohldag, Y.-D. Chuang, A. Scholl, A. T. Young, A. Doran, D. S. Dessau, H. Zheng, J. F. Mitchell, H. A. Dürr and J. Stöhr. Appl. Phys. Lett. **101**, 132402 (2012).

[123] G. M. De Luca, G. Ghiringhelli, M. Moretti Sala, S. Di Matteo, M. W. Haverkort, H. Berger, V. Bisogni, J. C. Cezar, N. B. Brookes and M. Salluzzo. Phys. Rev. B **82**, 214504 (2010).

[124] S. Brück, S. Macke, E. Goering, X. Ji, Q. Zhan and K. M. Krishnan. Phys. Rev. B **81**, 134414 (2010).

[125] S. Brück, S. Bauknecht, B. Ludescher, E. Goering and G. Schütz. Rev. Sci. Instrum. **79**, 083109 (2008).

[126] S. Macke, S. Brück and E. Goering. ReMagX: X-Ray Magnetic Reflectivity Tool (Max-Planck Institute for Intelligent Systems, Stuttgart) (2010).

[127] S. Brück. *Magnetic resonant reflectometry of exchange bias systems*. PhD thesis, Max-Planck-Institut für Metallforschung, Stuttgart (2009).

[128] J. Rodríguez-Carvajal, M. Hennion, F. Moussa, A. H. Moudden, L. Pinsard and A. Revcolevschi. Phys. Rev. B **57**, R3189 (1998).

[129] J. V. Roosmalen, E. Cordfunke, R. Helmholdt and H. Zandbergen. J. Solid State Chem. **110**, 100 (1994).

[130] A. Röseler. *Infrared Spectroscopy Ellipsometry*. Akad.-Verlag (1990).

[131] Y. Okimoto, T. Katsufuji, T. Ishikawa, T. Arima and Y. Tokura. Phys. Rev. B **55**, 4206 (1997).

[132] M. Quijada, J. Černe, J. R. Simpson, H. D. Drew, K. H. Ahn, A. J. Millis, R. Shreekala, R. Ramesh, M. Rajeswari and T. Venkatesan. Phys. Rev. B **58**, 16093 (1998).